Politecnico di Milano

School of Industrial and Information Engineering

Master of Science in Materials Engineering and Nanotechnology

MOBILITY MAXIMIZATION IN ORGANIC FIELD-EFFECT TRANSISTORS VIA MACHINE LEARNING AND DESIGN OF EXPERIMENTS

Supervisor: Prof. Carlo S. Casari
Co-Supervisors: Stefano Pecorario, Mario Caironi

Master thesis of:
Stefano Reale
919140

Academic Year 2019-2020

Essentially, all
models are wrong,
but some are useful.

George E. P. Box

Abstract

The last decade has seen a burst in the development of organic electronics. Indeed, the increasing electrical performances of organic semiconductors (OSCs) allowed this technology to "leave the laboratory" and be implemented in the first real applications. Organic electronics presents many advantages compared to its traditional inorganic counterpart. For instance, it allows the fabrication of transparent and flexible devices exploiting solution processes. However, the conduction properties of organic semiconductors are still poor, and, for this reason, organic electronics is not meant to replace the well known silicon technology but to be implemented in new kinds of applications.

In this thesis work, the use of machine learning-assisted optimization have been studied in the field of organic field-effect transistors (OFETs). The optimization tasks in organic electronics are often time consuming and require a large number of experiments. Compared to the usual optimization approach adopted in academic laboratories, these novel techniques are able to better identify the interplay of different factors, and, generally, require fewer experiments, hence reducing costs in terms of time and money.
Two optimization methods (support vector regression (SVR) and bayesian optimization (BO)), based on machine learning algorithms and design of experiments , were used to maximize the mobility of OFETs. Firstly, the methods were validated and compared on a well known system: OFETs with P(NDI2OD-T2) (a polymeric OSC also known as "N2200") as active material. Afterwards, the methods were used to draw predictions on OFETs fabricated with a new kind of small-molecule OSC containing a *sp*-carbon chain: tetraphenyl butatriene (named hereafter "[3]Ph").

The optimization of N2200-based OFETs led to the fabrication of devices with mobilities comparable with the ones obtained from the state-of-the-art for the

same system. Additionally, it was possible to have a better visualization of the "area of interest" on which to focus the future experiments to maximize the mobility of OFETs fabricated with [3]Ph as active material.

Estratto

L'ultimo decennio ha visto un considerevole sviluppo dell'elettronica organica. Le crescenti prestazioni elettriche dei semiconduttori organici hanno infatti permesso a questa tecnologia di "lasciare il laboratorio" ed essere implementata in applicazioni reali. L'elettronica organica presenta molti vantaggi rispetto alla sua controparte inorganica, ad esempio, rende possibile la produzione di dispositivi trasparenti e flessibili attraverso processi da soluzione. Tuttavia, le proprietà di conduzione dei semiconduttori organici sono tuttora limitate. Per questo motivo, l'elettronica organica non è volta a sostituire la performante tecnologia del silicio, bensì ad essere utilizzata in nuove, diverse applicazioni.

In questa tesi sono stati utilizzati due metodi di ottimizzazione per massimizzare la mobilità nei transistor organici a effetto di campo (OFET). Generalmente, i processi di ottimizzazione nel campo dell'elettronica organica sono molto dispendiosi in termini di tempo e denaro. Queste nuove tecniche invece, rispetto alle comuni tecniche di ottimizzazione adottate nei laboratori accademici, riescono ad identificare meglio le interazioni tra fattori e in generale richiedono un minor numero di esperimenti.
I due metodi studiati sono la "support vector regression" (SVR) e la "ottimizzazione bayesiana" (BO), i quali si basano sul "machine learning" e sul "design degli esperimenti" (DoE). Inizialmente, i metodi sono stati validati e confrontati su un sistema noto, OFET con P(NDI2OD-T2) come materiale attivo (un polimero semiconduttore conosciuto anche come "N2200"). Successivamente, i due metodi sono stati usati per trarre previsioni su OFET prodotti con un nuovo tipo di semiconduttore organico a piccola molecola contenente una catena di carbonio *sp*: tetraphenyl butatriene (chiamato d'ora in poi "[3]Ph").

L'ottimizzazione dei transitor a base di N2200 ha portato alla produzione di dispositivi con mobilità superiore a quella ottenuta dallo stato dell'arte di dispositivi

equivalenti. Inoltre, è stato possibile ottenere una migliore visualizzazione dell'area di interesse dove concentrare gli esperimenti futuri per massimizzare la mobilità dei transistor a base di [3]Ph.

Acknowledgments

At the end of this journey I would like to thank all the people that supported me and made this thesis work possible.
Starting from my family, that has always been by my side in every decision I took. All the friends that I made during my studies. From my incredibly inspiring high-school class mates who gave a philosophical, artistic and non-engineering view of the world. My university colleagues (specially "I Ragazzi") who, with curiosity and competition, always pushed me to do my best. The friends who have accompanied me in my life-changing experience in Shanghai. And finally, all the long-time friends of mine, from Sesto san Giovanni (and Monza), who have grown up with me and have always been by my side.
A big thank goes also to Carlo Casari, Mario Caironi and Stefano Pecorario, who helped me in the practical realization of this thesis work. In conclusion, I would like to thank Politecnico di Milano that, thanks to its professors, gave me an incredibly high level of education and made the realization of many of my dreams possible.

Contents

Acronyms

AFM atomic force microscopy. 109

BGBC bottom-gate bottom-contacts. 21, 22, 98, 109

BGTC bottom-gate top-contacts. 21

BLA bond-length alternation. 25, 27, 28, 51

BO bayesian optimization. 2, 47, 49, 66, 84, 86, 87, 106–109

CAW carbon atomic wire. 2, 3, 24, 25, 27–29, 51, 98, 109

CB chlorobenzene. 53, 71

CN 1-chloronaphthalene. 53, 60, 71, 72

DoE design of experiments. 2, 32, 33, 35, 37, 66–69, 79, 84, 99, 104, 107–109

$\mathbf{E_F}$ Fermi level. 16, 17

FET field-effect transistor. 5, 10, 18–20

GP Gaussian process. 47, 84

HOMO highest occupied molecular orbital. 10, 17, 49, 51

IIT Istituto Italiano di Tecnologia. 2, 3

KCC kinetically controlled crystallization. 56, 57, 67, 93, 95, 96

LUMO lowest unoccupied molecular orbital. 10, 17, 49, 51

Mes mesitylene. 53, 71

MOSFET metal-oxide-semiconductor field-effect transistor. 5, 6, 8

MSE mean squared error. 37

NMP *n*-Methyl-2-pyrrolidone. 53

OFET organic field-effect transistor. 2, 3, 7–9, 16, 18, 20, 21, 27, 28, 49, 51, 52, 55, 66, 67, 69, 96, 98, 108, 109

OLED organic light-emitting diode. 1

OSC organic semiconductor. 1–3, 7–12, 14–17, 21, 22, 24, 49, 51, 55, 98, 108

OTFT organic thin film transistor. 16

OVAT one variable at a time. 1, 31, 32, 34, 35, 109

PFBT pentafluorotiophenol. 51, 104

PLM polarized light microscopy. 60, 62, 95, 96, 100, 109

PME Printed and Molecular Electronics. 3, 49, 98

PMMA poly(methyl methacrylate). 58, 59, 62

PS polystyrene. 51, 98, 104

RBF radial basis function. 43

SAM self-assemble monolayer. 22, 51, 104

SPA semiconductor parameter analyzer. 62, 63, 65, 69, 79, 96

SVM support vector machine. 41

SVR support vector regression. 2, 41, 44, 47, 49, 66, 74, 76, 79, 83, 84, 87, 88, 93, 96, 103, 106–109

TGBC top-gate bottom-contacts. 21, 22, 49, 52, 55, 109

TGTC top-gate top-contacts. 21

Tol toluene. 53, 71

W_f work function. 10, 17, 51

Introduction

The field of organic electronics has seen a growing interest during the last few decades. Especially after the first demonstration of an efficient low voltage thin film organic light-emitting diode (OLED) by Ching Tang and Steven van Slyke at Kodak in 1987 [1]. Today, organic semiconductors (OSCs) find many engineering applications, and are now reaching the consumer market [2]. The most notable applications are in the field of optoelectronics (OLEDs) [1, 2], energy conversion (organic photovoltaic and organic thermoelectrics) [3, 4], microelectronics (Organic field-effect transistors) [5, 6] and healthcare [7].
OSCs presents many advantages compared with traditional inorganic semiconductors like silicon [6]. Indeed, organic chemistry posseses a great tunability of properties, thanks to the tailorability of organic molecules. Another big advantage of OSCs is their ability to be deposited from solution, allowing the production of thin-films, large area [8], transparent [5] and flexible [9] electronics. The major drawback associated with OSCs is related to their poor electrical performances. In particular, they posses a charge mobility which is order of magnitudes lower than their inorganic counterpart. For this reason, the objective of organic electronics is not to exceed the level of performance of conventional electronics, but to enable the development of new devices characterized by new functionalities (e.g. flexibility, transparency etc.) and a reduced production costs [10]. The success of OSCs is, however, linked to the improvement of their charge mobility. Up to now, the optimization of this property has been particularly difficult because of its dependency on many parameters, such as the molecular structure and packing of the semiconductor, the morphology of the film and the presence of impurities. However, the main factor hindering this improvement is the lack of solid physical models and the consequent necessity of "case study" approaches for different OSCs.
The usual optimization process adopted in academic laboratories consists in varying one variable at a time (OVAT) and observe how the mobility changes. However

this approach is highly inefficient and requires a large number of experiments, associated with a high cost in terms of money and time. New optimization methods, based on machine learning and design of experiments (DoE), have recently proven useful in the improvement of organic photovoltaics [3]. However, this modern approach has never been tested in the field of organic field-effect transistors (OFETs). The field of machine learning is extremely wide, with applications ranging from data analysis to artificial intelligence. Some concepts, typical of data science, can be adapted in order to make predictions and enabling a better visualization and understanding of the optimization problem. Indeed, with regression techniques, it is possible to obtain maps that can help the experimentalist in finding the "region of interest" on which to focus the experiments.

The goal of this thesis is to implement two different machine learning-based optimization techniques for the maximization of the mobility in OFETs: support vector regression (SVR) and bayesian optimization (BO). Initially, the two methods have been validated and compared using a well known polymeric OSC, P(NDI2OD-T2), also known as "N2200". Afterwards, using an existing dataset, some predictions were drawn on a new unconventional small-molecule OSC based on carbon atomic wires (CAWs): tetraphenyl butatriene, also knwon as "[3]Ph".
Conventional OSCs owe their semiconducting behaviour to the π-electrons delocalization due to their sp^2-hybridized carbon atoms. CAWs instead, are characterized by *sp*-hybridized carbon atoms. Studies on isolated CAWs have shown outstanding conduction properties, even superior to those of the graphene and carbon nanotubes [11]. However, the poor stability of *sp*-carbon hamper the synthesis of long wires and their use in real applications. For this reason the carbon chain has to be isolated with chemical moieties that alter the conduction properties and lead to a much lower mobility associated with intermolecular transport. A better understanding of the deposition techniques is the key to the mobility maximization of these kinds of system and a necessary requirement for its implementation in commercial devices.

The initial DoE was obtained using the "GPyOpt" open-source library [12] in Python [13]. The same library was used to write the BO script, while the script used in the "SVR optimization" was adapted from the open-source script written by B. Cao et al. [3], available online.
The fabrication of OFETs with N2200 was carried out in the laboratories of Istituto Italiano di Tecnologia (IIT) under the supervision of Mario Caironi and

Stefano Pecorario of Printed and Molecular Electronics (PME) group in IIT. The [3]Ph dataset, obtained by previous work of PME group, was analysed and processed in order to improve the training of the machine learning algorithm.

The thesis starts with an introduction on OSCs and OFETs followed by a theoretical introduction on CAWs and on the machine learning techniques adopted. Afterwards, the materials and methods used in this work are described in details, and finally the obtained results are presented in the last chapter.

Chapter 1

Organic field-effect transistors

1.1 Field-effect transistor

Field-effect transistors (FETs) are the fundamental building blocks of modern computers. The FET is a 3-electrode device in which an electric field is used to control the conductivity of a thin channel at the semiconductor-insulator interface. It can be described as an electronically driven switch in which it is possible to allow or prevent the flow of current between two electrodes without any mechanical moving parts. The current flowing between two terminals ("**source**" and "**drain**") can be switched "ON" and "OFF" with the application of a voltage to the third one, called "**gate**". By exploiting this property, it is, for instance, possible to use the transistor as a logical bit able to encode the information (1 or 0) in the form of a current (ON or OFF). By combining different FETs it is possible to build logical gates and, ultimately, computers. The most widely used FET is the silicon metal-oxide-semiconductor field-effect transistor (MOSFET), composed by doped silicon as semiconductor and silicon dioxide as insulator. A schematic representation of a MOSFET is shown in Fig 1.1 underlining the most important geometrical parameters: L (channel length), W (channel width) and t_{ox} (dielectric thickness). In silicon MOSFET, silicon is doped to increase its conductivity: p-type doping is achieved with the introduction of an element of the V group and the resulting semiconductor will show hole conductivity while n-type doped silicon is realized with elements of the VII group and will lead to electron conductivity. The most common MOSFET is composed of an n-p-n or a p-n-p junction.

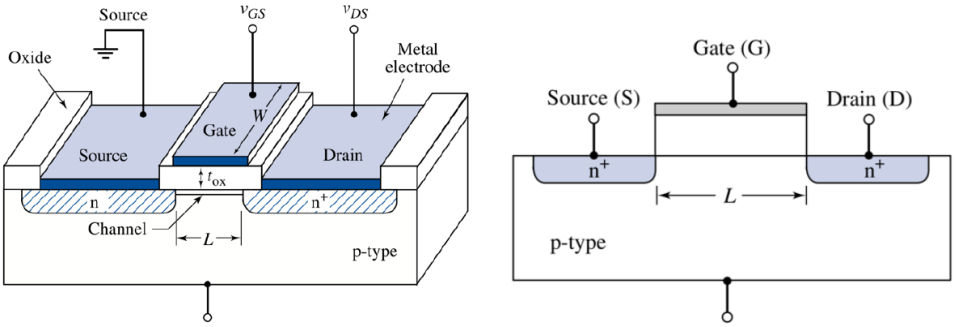

Figure 1.1: *General architecture of an n-p-n MOSFET [14].*

1.1.1 Working principle

Considering an n-p-n device, the active part is the p-type material. By applying a positive vertical voltage at the gate, it is possible to accumulate charges at the semiconductor-insulator interface. The gate terminal-insulator-semiconductor system behave as a capacitor and an electric field will be established when the capacitor is charged. The electric field, generated by the induced positive charges at the gate terminal, will repel holes in the semiconductor, which are majority carriers in the case of p-doped silicon, moving them away from the semiconductor-dielectric interface. At the same time, it will attract electrons, which are the minority carriers. Hence, increasing the gate voltage, a negative space-charge region will be created. At a certain point, if the positive bias is large enough, the density of minority carriers at the interface will be comparable to the one of majority carriers, creating the so-called "electron inversion layer" or channel. This channel is able to connect the two n-doped regions connected to the source and drain terminals, such that, if a voltage is applied between these two terminals, a current will flow with an intensity determined by the gate voltage and the conductivity of the conducting channel. For a p-n-p device, the working principle is equivalent, however, the applied bias at the gate is negative and creates a hole inversion layer. This operating mode is called enhancing mode. In accumulation mode instead of creating an inversion layer of minority carriers, an accumulation layer of majority carrier is formed, applying an opposite bias, and prevents the conduction between source and drain. In Fig 1.2 the two operation modes of a MOSFET are schematized.

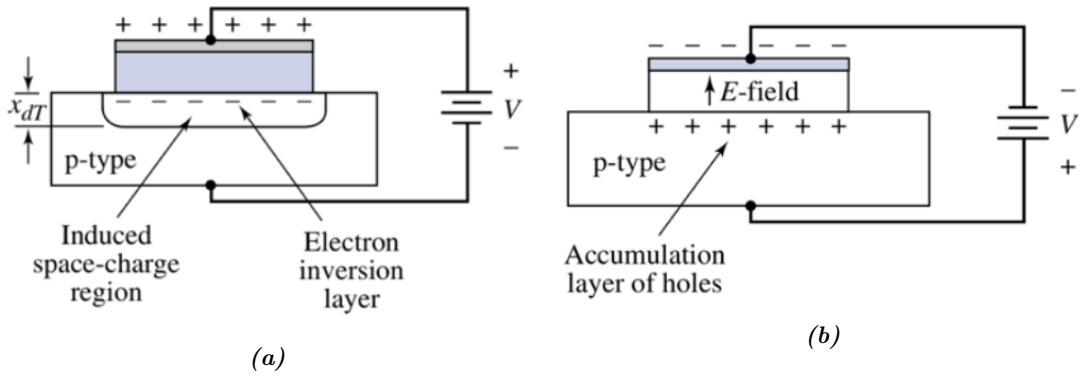

Figure 1.2: *Schematics of the two operation mode of a p-type MOSFET: (a) enhancing mode and (b) accumulation mode [14].*

1.2 Organic field-effect transistor

Over the past three decades, a new kind of device based on organic semiconductors (OSCs) has been conceptualized and developed: the so-called organic field-effect transistor (OFET) [15]. OSCs are molecular solids or polymers composed by molecules characterized by π-conjugation (usually in the form of alternating single and double carbon-carbon bonds), thus containing overlapped p-orbitals with delocalized electrons. π-conjugation underlies the semiconducting behaviour of OSCs and makes the charge transport possible.

The OFET architecture is similar to its inorganic counterpart being a three-terminal device with a semiconductor as active material. However, the working principle is completely different due to the intrinsic differences between organic and inorganic semiconductors. Indeed, inorganic semiconductors are characterized by a highly crystalline structure and an important orbital delocalization. This results in the characteristic band structure, and the charge transport is well approximated by the Bloch description. For OSCs, one would expect the only difference to be that the Bloch states in the tight binding model would be constructed from molecular orbitals instead of atomic orbitals of isolated atoms [16]. The situation, however, is very different. Whereas inorganic semiconductors crystals are bounded by covalent bonds, in OSCs the molecules interact only via Van der Waals forces. In Van der Waals molecular solids, the intermolecular distances are much larger than in covalently bonded inorganic semiconductors. For this reason, the resulting orbital delocalization is much smaller, and the associated band structure is char-

acterized by a small bandwidth and resembles the molecular orbitals levels [16]. As a consequence, the main disadvantages of organic electronics are related to the poor conduction properties of OSCs with respect to their organic counterparts.

The OFET has several advantages compared with its inorganic counterpart [6]. (i) Being based on OSCs it is possible to synthesize an incredibly large number of different molecules (from small molecules to polymers), thus, having great control on the semiconductor properties. (ii) With organic molecules, it is possible to form thin films or pliant polymeric devices, allowing the realization of flexible [9] and transparent electronics [5]. (iii) Finally, it is possible exploit a great variety of deposition techniques. The fabrication of MOSFETs requires high temperatures and a high level of vacuum because any form of contamination is highly detrimental; in order to deposit organic molecules, instead, it is possible to use both physical techniques, such as evaporation, and solution-based processes, thus, allowing the deposition at room temperature and atmospheric pressure. This last point is particularly important. Indeed, the biggest advantage of organic electronics is the possibility of fabricating devices on a large scale, with reduced fabrication costs, and a less restrictive level of precision. One of the most promising application of OFETs is the so-called "printed electronics". This technique points at fabricating large-area electronic devices on flexible and/or transparent substrates with applications in the field of microelectronics [5] and healthcare [7].

It is possible to group OSCs in three main categories: small molecules, polymers and carbon allotropes [17]. Small molecules are characterized by more desirable conduction properties related to their higher degree of crystallinity, on the other hand their processability from solution is reduced. Indeed, their tendency to crystallize in a fast way hinder the deposition of homogeneous films. Polymers, instead, usually have a higher solubility and their deposition is easier to control. Additionally, they present more desirable mechanical properties due to their stretchability [18] and flexibility [9], although their semi-crystalline structure is detrimental for their conduction properties. Finally, carbon allotropes, such as fullerenes, carbon nanotubes or graphene, present outstanding electronic properties resembling the ones of inorganic materials. The problems related to these materials lie in their poor tailorability, i.e. chirality control in nanotubes or bandgap in graphene [19], which makes their implementation in devices problematic.

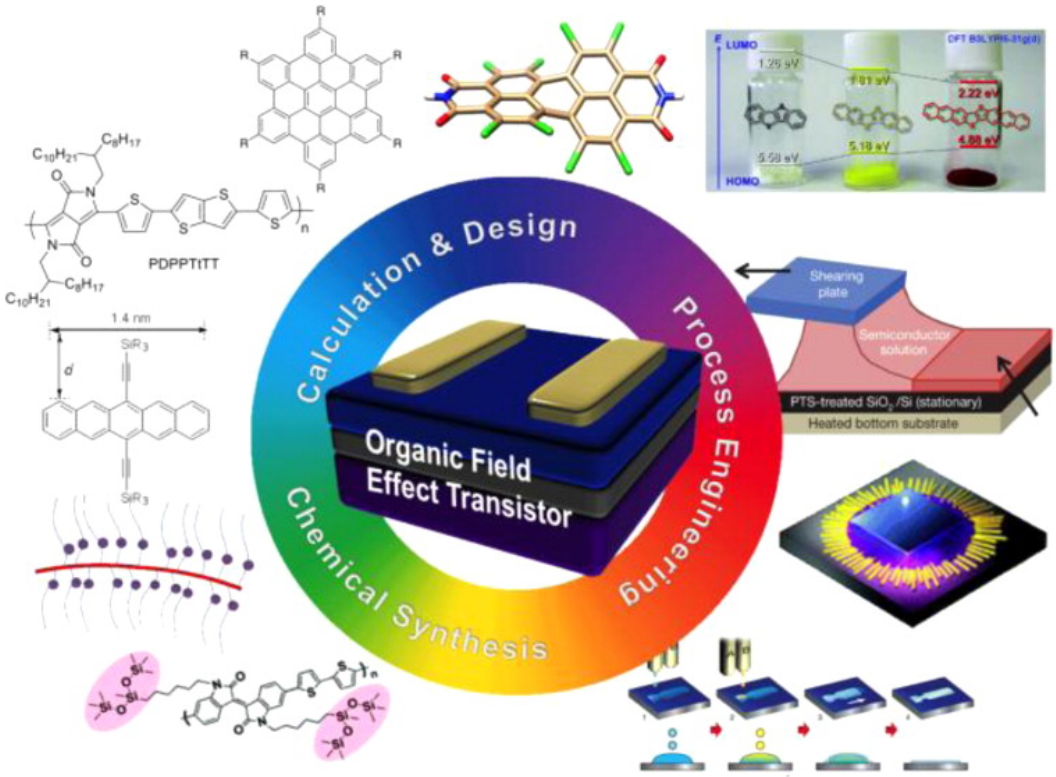

Figure 1.3: *OFETs, schematic overview [6].*

1.2.1 Working principle

As for its inorganic counterpart, also in OFETs it is possible to modulate the conductivity of a thin layer of material, which acts as conducting channel, by applying a bias to the gate terminal. However, to create the channel, unlike inorganic semiconductors, the OFET operates in accumulation regime. When a bias voltage is applied to the gate terminal, charges are injected into the channel between source and drain and, equivalently to a capacitor, accumulates in the semiconductor/insulator interface. Upon charge injection, the material conductivity will increase, creating a conductive channel and allowing a current flow if a voltage is present between source and drain. Applying a negative bias at the gate, a channel of positive charges will be created, and the material will behave as a p-type semiconductor. On the contrary, if a positive voltage is applied, a channel of negative charges is created, and the material behaves as n-type.
In principle, all OSCs can show p-type and n-type behaviour, for this reason, they are defined "ambipolar". However, it is still possible to distinguish between p-type

and n-type materials by considering their higher tendency to undergo a positive or negative charge-injection doping process, respectively [20]. A p-type material will be characterized by a high highest occupied molecular orbital (HOMO), while, an n-type material will show a low lowest unoccupied molecular orbital (LUMO) with respect to the work function (W_f) of the metal contacts (see Chapter 1.4).
In OSCs, the charge injection process can be seen as a reversible doping process. Charge-injection doping generates charged molecules thanks to charge transfer processes, thus, increasing the charge-carrier density and the conductivity of the semiconductor.

1.3 Charge transport in organic semiconductors

Charge transport in OSCs is the result of intra-molecular and inter-molecular transport. The intra-molecular contribution can be relevant in polymers, while is negligible in the case of small molecules.
One of the most important parameters of semiconducting materials is the so-called **charge mobility**. Charge mobility determines the suitability of semiconductors for applications in a large variety of electronic devices, including FETs [21]. It governs how fast charges can move in a material under an applied electric field. The carrier mobility influences the device behaviour through its frequency response or time response in two ways. First, the carrier velocity is proportional to the mobility for low electric fields. Hence, higher mobility materials are likely to have a higher frequency response because charges take less time to travel through the device. Moreover, the device current depends on the mobility, hence, higher mobility materials present, in general, higher currents.
In the absence of any external potential, transport is purely diffusive and is generally described by a simple diffusion equation [20]:

$$\langle x^2 \rangle = nDt \tag{1.1}$$

where $\langle x^2 \rangle$ denotes the mean-square displacement of the charges, D is the diffusion coefficient, t is the time, and n represents an integer number equal to 2, 4, or 6 for one-, two-, and three-dimensional (1D, 2D, and 3D) systems, respectively. The charge mobility μ is related to the diffusion coefficient via the Einstein-Smoluchowski equation:

$$\mu = \frac{eD}{K_b T} \tag{1.2}$$

where K_b is the Boltzmann constant and e is the electron charge. The application of an external electric field induces a drift of the charge carriers; the mobility can then be alternatively defined as the ratio between the velocity, v, of the charges and the amplitude of the applied electric field, F:

$$\mu = \frac{v}{F} \tag{1.3}$$

Diffusion should be seen as a local displacement of the charge around an average position, while drift induces a displacement of the average position.
When a charge is introduced into the system, for example through a charge injection process, it is possible to distinguish two transport regimes: (i) polaronic band transport typical of ideal (without defects) molecular crystals (i.e. small-molecules OSCs) in the low temperature limit ($T \to 0$), and, (ii) small polaron hopping transport typical of systems at higher temperatures or with an higher degree of defects such as polymeric OSCs [20, 22].

1.3.1 Polaronic band transport

When individual conjugated molecules are brought together in a crystalline structure, their molecular orbitals are only weakly perturbed by the neighbouring molecules [22]. Indeed, in small-molecule OSCs, the energy required to ionize a molecule exceed by at least one order of magnitude the interaction energy between two adjacent molecules in the crystal. The resulting band structure is formed by narrow bands closely matching the molecular orbitals of the isolated molecules [16].
When a charge is introduced, the total Hamiltonian of the system can be expressed as a sum of three contributions (*electronic*, *nuclear* and *electron-phonon coupling*):

$$H = H_{el} + H_{nucl} + H_{el-nucl} \tag{1.4}$$

Considering a one-dimensional array of molecules, with one state $|j\rangle$ per molecule corresponding to a frontier molecular orbital, each interacting with its nearest neighbours we can write the *electronic* Hamiltonian as

$$H_{el} = \sum_j (\epsilon|j\rangle\langle j| + \tau|j\rangle\langle j+1|) \tag{1.5}$$

where ϵ is the energy of the state and τ is the electronic coupling (also called transfer or hopping integral) between the localized molecular orbitals. In the low temperature and defects-free limit, the charge carrier in the band behaves like a particle with an effective mass

$$m^* = \frac{\hbar^2}{(2|\tau|L^2)} \tag{1.6}$$

where τ is the transfer integral and L is the distance between two sites. Therefore, in this picture, the charge carrier can be described as a delocalised wavepacket. The transfer integral is strongly dependent on the molecular orbital overlap [20], thus, it decays exponentially with the intermolecular distance (as shown in Fig 1.4*(a)*) and it is a function of the relative phase of the overlapping orbitals (as shown in Fig 1.4*(b)*). This dependency implies that the transport properties in OSCs will be strongly related to the packing arrangement of the molecules.

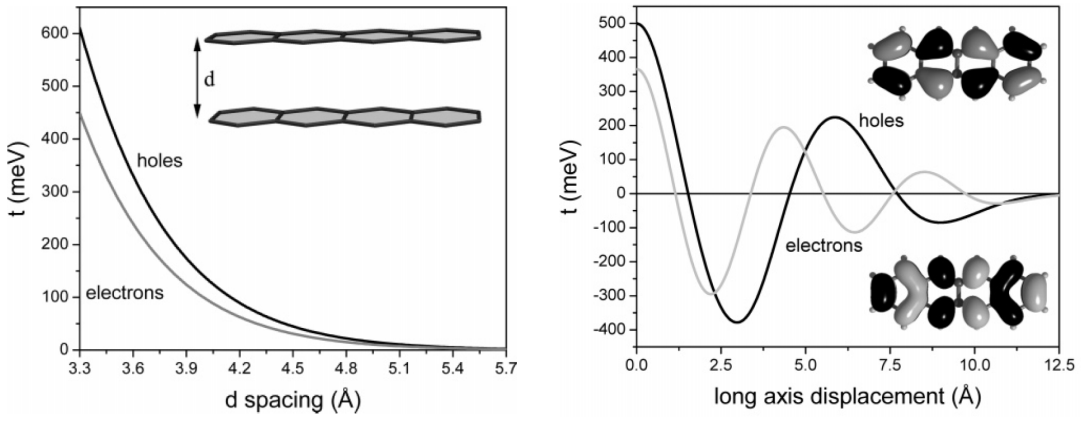

Figure 1.4: *Calculation of the transfer integrals for electrons and holes in a tetracene cofacial dimer as a function of: (a) intermolecular distance, and, (b) degree of translation of one molecule along its long axis, with a representation of the HOMO (top) and LUMO (bottom) wavefunctions [20].*

Considering, for simplicity, a single nuclear mode ω per molecule, the *nuclear* Hamiltonian can be expressed as [22]:

$$H_{nucl} = \sum_j \frac{\hbar\omega}{2}(q_j^2 + p_j^2) \tag{1.7}$$

with q_j and p_j being the adimensional displacement and momentum on molecule j, respectively.
With the introduction of a charge the equilibrium geometry of a molecule is modified [22]. This is the so called *local electron-phonon coupling*, and its related Hamiltonian can be expressed as:

$$H_{el-nucl} = g\hbar\omega \sum_j q_j |j\rangle\langle j| \tag{1.8}$$

where g is a parameter that quantifies the electron-phonon coupling and can be seen as the shift of the equilibrium position as shown in Fig 1.5*(c)*. The charge carrier and the associated deformations is called **polaron**. In the case of polaronic band transport, the charge wavefunction is delocalized over a large number of molecules, thus, only a small deformation is associated with each one of them. The resulting polaron will be delocalized and its states will be described by band states that are solutions of a Hamiltonian similar to Eq 1.5:

$$H_{polaron} = \sum_j (\epsilon' |j\rangle\langle j| + \tau' |j\rangle\langle j+1|) \tag{1.9}$$

where the only difference is in the use of the on-site energy ϵ' and the effective transfer integral τ'. The latter has a temperature dependence of the form:

$$\tau' = \tau e^{-\frac{1}{2}g^2(N_\omega + \frac{1}{2})} \tag{1.10}$$

with $N_\omega = [exp(\hbar\omega/K_bT) - 1]^{-1}$. This temperature dependence has the effect of further decreasing the transfer integral with increasing temperature, thus, increasing the effective mass as shown in Eq 1.6. It is finally possible to obtain the mobility, in this transport regime, as:

$$\mu = \frac{e \cdot t_S}{m^*} \tag{1.11}$$

with t_S being the average time between collisions with defects and e the electron charge. The mobility, thus, decreases with increasing temperature. This is considered a signature of polaronic band transport.

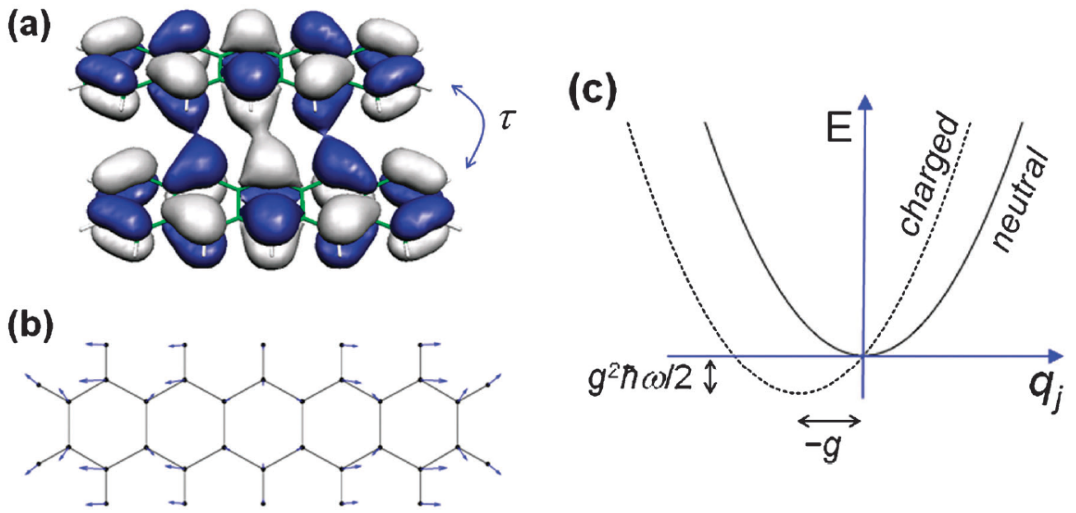

Figure 1.5: *Illustration of the terms appearing in the band transport model in the case of pentacene molecules: (a) electronic coupling τ, (representation of the HOMO orbitals on two neighbouring pentacene molecules), (b) nuclear deformation caused by the introduction of a charge in the molecule (The arrows illustrate the direction and relative magnitude of the deformation upon removal of an electron from pentacene), (c) change in energy and equilibrium configuration upon the introduction of a charge in an idealized system where there is only one degree of freedom per molecule [22].*

1.3.2 Small polaron hopping transport

As the temperature is increased, the polaronic band becomes of vanishing width ($\tau' \to 0$) and the effective mass becomes infinite [22]. It is more convenient, then, to describe the carrier wavefunction as localized on a single molecule. This same model is also well suited for "disordered" systems such as polymeric OSCs. In these cases, the polaron moves from site to site and its dynamics can therefore be described in a model containing only two sites (1 and 2) with $\epsilon = 0$:

$$H_{two-side} = H_{nucl} + g\hbar\omega q_1|1\rangle\langle 1| + g\hbar\omega q_2|2\rangle\langle 2| + \tau(|1\rangle\langle 2| + |2\rangle\langle 1|) \qquad (1.12)$$

This hopping process from one site to the next can be seen as a chemical reaction with a characteristic rate constant k_{hop}. In the initial state the carrier is in site 1, the equilibrium position of the oscillator 1 is $q_1^{eq} = -g$ and the equilibrium position of the oscillator 2 is $q_2^{eq} = 0$. In the final state, the carrier is in site 2, the equilibrium position of oscillator 1 is $q_1^{eq} = 0$ and the equilibrium position of oscillator 2 is $q_2^{eq} = -g$. The hopping takes place whenever there is enough energy to overcome the energy barrier.

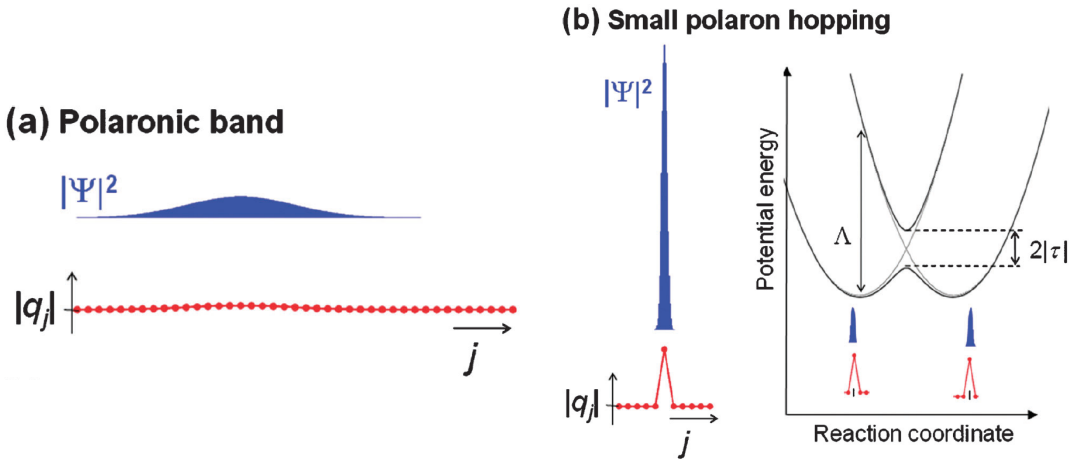

Figure 1.6: *Schematics of the two charge transport models:(a) polaronic band model characterized by the delocalization of the charge carrier wavefunction over many molecules and a small lattice deformation. (b) polaron hopping characterized by the carrier wavefunction localized on one molecular site, which is also distorted by the excess charge. An example of potential energy curve is reported for the process of hopping to the neighboring site. The energy is determined by τ and the reorganization energy Λ ($\Lambda = 2g^2\hbar\omega$), as discussed in the text. [22]*

1.3.3 Role of morphology

As already anticipated, the transport properties in OSCs are highly influenced by the morphology of the semiconducting material, in particular by the molecular packing, crystalline disorder and presence of impurities [20]. Several studies have shown that the crystallographic orientation within the channel will alter the measured field-effect mobility and that grain boundaries can play an important role in charge transport within the channel [23]. Ideally, single crystals would show the best transport properties and maximize the mobility [24]. However, even if small-molecules OSCs tend to form single crystals, their fast crystallization process prevents a uniform deposition and hinder the formation of thin films [25, 26],

necessary for the fabrication of organic thin film transistors (OTFTs). It is possible to improve the transport properties of the OSC by acting on the fabrication techniques. For example, with the control of the deposition method, it is possible to have an influence on the stacking direction of the molecules relative to the substrate, thus, increasing the mobility [8]. The main directional deposition techniques adopted in the fabrication of OFETs are off-center spin-coating [27], bar-coating [28] and blade coating [29]. With these techniques, it is possible to align the crystallographic domains in a favourable direction for conduction, thus increasing the mobility and the performance of the device. Another way to improve the morphology is to blend small-molecule OSC with a polymer (semiconducting or insulating). In this way, it is possible to control the crystallization and obtain more uniform films, thus increasing reproducibility and performances [26, 30]. An example of blended small-molecule OSC is reported in Fig 1.7. Regarding polymeric OSCs, it is also possible to exploit the pre-aggregation in solution by the optimal selection of the solvent and by using directional deposition techniques [31].

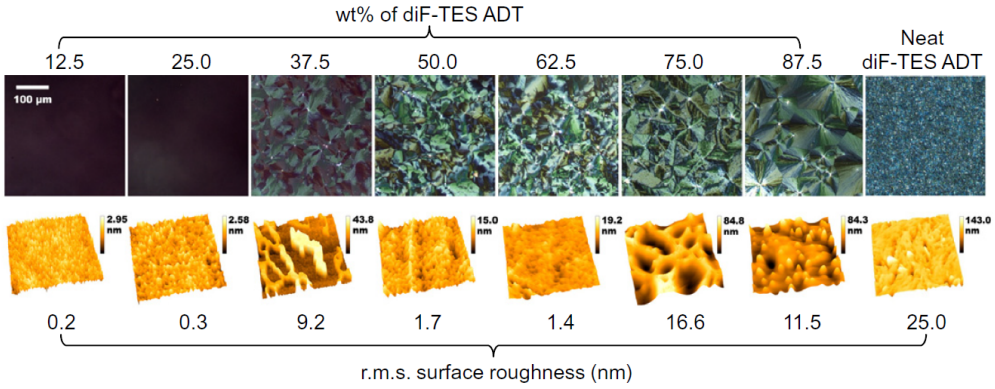

Figure 1.7: *Effect of concentration of diF-TES ADT in a small-molecule/polymer blend with PTAA deposited by spin-coating. Surface roughness and peak-to-peak heights were measured with AFM [32].*

1.4 Charge injection

The main factor that governs the performance of an OFET, along with the charge transport, is the charge injection process.
When two materials with a different Fermi level (E_F) are brought into contact (e.g. the OSC and the metal contacts), they reach thermal equilibrium and establish

a common E_F by exchanging charge carriers [33]. This gives rise to a contact potential across the interface, equal to the difference of the Fermi levels of the isolated materials. Charges transferred to the semiconductor can be stored in the form of a space charge, as a surface sheet charge (if surface states are present), or a combination of the two.
In order to describe the potential across the interface it is necessary to introduce the concept of work function (W_f). The W_f is the minimum energy required to remove an electron from a solid to a point in the vacuum immediately outside the solid surface. The metal W_f, is a surface property and, as such, it is modified by the presence of molecules near the metal surface [33].

1.4.1 Contact resistance

From conventional semiconductor electronics, it is known that creating a low resistance ohmic contact requires alignment of the metal E_F with the energy levels (bands) of the semiconductor. Usually in metal-OSC interfaces an interface dipole is present due, for example, to charge transfer or reduction of the metal W_f caused by the absorption of the organic layer [34]. The charge injection efficiency depends on the potential barrier formed at the interface (*hole or electron injection barrier*). A good estimation of the *hole injection barrier* from the metal to the OSC is given by the *LUMO offset* that in turn can be expressed as:

$$E_F - LUMO = W_f - IP \pm \Delta \tag{1.13}$$

where IP is the ionization potential of the OSC and Δ is the potential change due to the dipole. For the *electron injection barrier* an equivalent expression can be obtained by considering the HOMO and the electron affinity ($E.A.$):

$$HOMO - E_F = W_f - E.A. \mp \Delta \tag{1.14}$$

A schematic representation of the energy levels present at the metal-OSC junction is reported in Fig 1.8 for the case of gold and pentacene. The degree of interaction between the molecules and the metal governs the formation of the dipole and the change in the W_f. It is possible to distinguish three adsorption regimes (reported in order of interaction strength): physisorption, weak chemisorption and strong chemisorption.

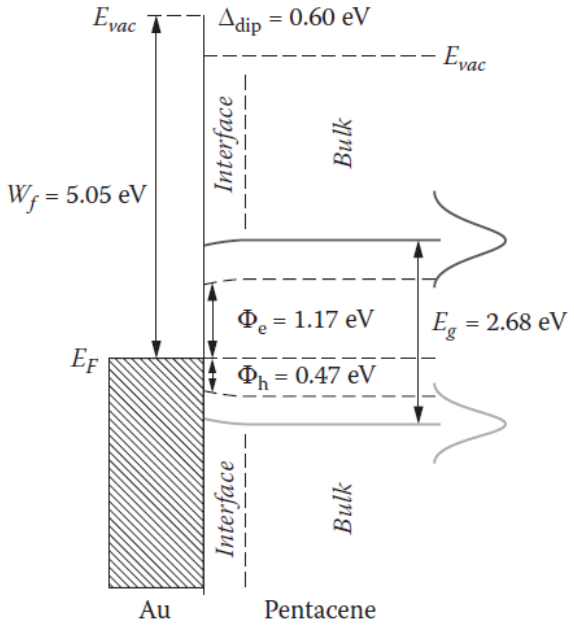

Figure 1.8: *Band diagram for the Au-pentacene interface. The hole injection barrier (Φ_h) is determined by taking the difference in energy between the Fermi level and the edge of the valence band [34].*

1.5 Devices

As already introduced in Chapter 1.2, OFETs are able to modulate the current between two electrodes with a bias applied to the gate.
An ideal FET is characterized by [34]:

- a mobility (μ) independent from the bias and constant over the channel
- a negligible contact resistance
- a negligible influence of defects on transport properties
- a transverse electric field much higher than the longitudinal one.

If these assumption are valid, it is possible to describe mathematically the current between source and drain with the use of the so called Schottky equations:

$$I_{ds} = \begin{cases} \frac{WC\mu}{L}\left[(V_g - V_{th})^2 V_{ds} - \frac{V_{ds}^2}{2}\right] & \text{if } V_{ds} < V_{ds}(sat) \\ \frac{WC\mu}{2L}(V_g - V_{th})^2 & \text{if } V_{ds} > V_{ds}(sat) \end{cases} \tag{1.15}$$

where I_{ds} is the output current at the drain, V_g is the gate bias, V_{th} is the threshold voltage (minimum voltage required for the creation of the conduction channel), V_{ds} is the voltage difference between source and drain, C is the capacitance of the device ($C = \epsilon/t$ with ϵ being the dielectric constant of the dielectric), W and t are the geometrical parameters already introduced in Chapter 1.1 and, finally, $V_{ds}(sat)$ is the drain voltage at saturation.
It is possible to distinguish between two operation regimes: linear regime and saturation regime [14]. In linear regime there is a direct proportionality between I_{ds} and V_{ds}, thus, the FET works as an ohmic resistance with a resistance R_{CH} related to the channel resistance (Fig 1.9*(b)*). If V_g is increased R_{CH} decrease. Increasing V_{ds} the voltage drop across the dielectric close to the drain terminal decreases, leading to a decrease of the charge density. This causes a deviation from linearity and the $I_{ds} - V_{ds}$ curve starts to bend. When V_D is further increased until $V_{ds} = V_g - V_{th}$, the channel is "pinched off" (Fig 1.9*(c)*) [35]. That means a depletion region forms next to the drain because the difference between the local potential $V(x)$ and V_g is now below V_{th}. From this moment, the FET works in saturation regime. Further increasing V_{ds} will not substantially increase the current because the potential at the pinch-off point remains $V_G - V_{th}$ and thus the potential drop between that point and the source electrode stays approximately the same, and the current saturates (Fig 1.9*(d)*).

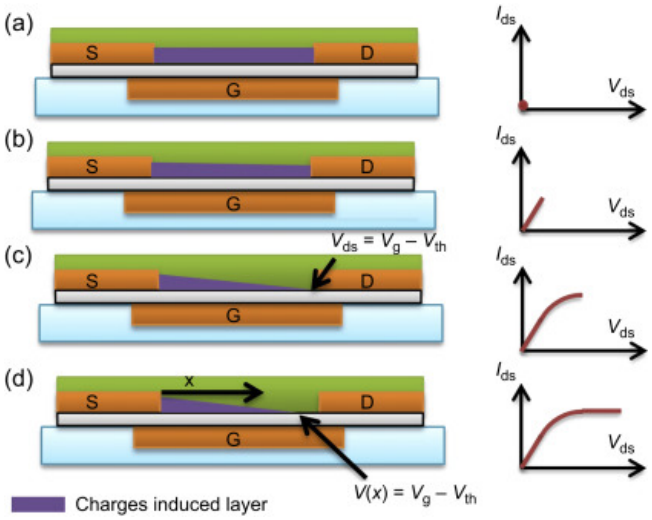

Figure 1.9: *Illustrations of operation regimes of a field-effect transistor: (a) generation of the charges, (b) linear regime, (c) start of saturation regime at pinch-off, and (d) saturation regime [35].*

Because there are two operation regimes, the current–voltage characteristics have to be described separately. For different gate voltages, with the increase of source-drain voltage V_{ds}, the current I_{ds} comprises the linear and saturation regimes (Fig 1.10*(a)*). In the transfer characteristics, at first the I_{ds} increases linearly with the voltage V_g when the gate voltage overcomes the V_{th} (Fig 1.10*(b)*). When the transistor is in the saturation regime, the square root of the saturation current is directly proportional to the gate voltage (Fig 1.10*(c)*).

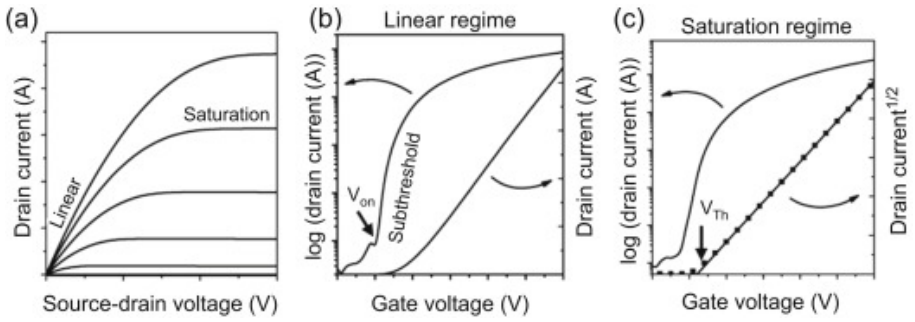

Figure 1.10: *Current-voltage characteristics of an n-channel OFET: (a) output characteristics, (b) transfer characteristics in the linear regime, and (c) transfer characteristics in the saturation regime [35].*

OFETs are often far from the model of ideal FET, in fact, the mobility is in general a function of the bias, the contact resistance is non-negligible and the presence of traps and defects, often unavoidable, influence the transport properties in a detrimental way. One marker of non-ideality and possible degradation is the formation of an hysteresis cycle, which may lead also to a shift of the threshold voltage in the transfer characteristic, during the forward and backward sweeps of the gate voltage V_g (Fig 1.11).

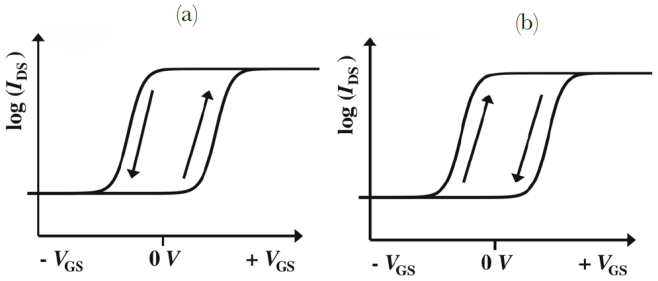

Figure 1.11: *Types of hysteresis cycles in OFETs: (a) higher back sweep current hysteresis. (b) Lower back sweep current hysteresis. [14].*

1.5.1 Architecture

There are four main architectures for OFETs, each one with its own advantages and disadvantages (Fig 1.12).

- **Top-gate top-contacts (TGTC)**(Fig 1.12*(a)*): the OSC is deposited on top of a substrate that acts as a support. Then, over the active material, source, drain and the dielectric are deposited. Finally, the gate is deposited on top of the dielectric.
- **Top-gate bottom-contacts (TGBC)**(Fig 1.12*(b)*): source and drain are deposited on the substrate prior to the OSC deposition, then the dielectric and the gate are deposited.
- **Bottom-gate top-contacts (BGTC)**(Fig 1.12*(c)*): the gate is deposited on the substrate and covered with the dielectric, then there is the deposition of the OSC followed by the deposition of source and drain on top of it.
- **Bottom-gate bottom-contacts (BGBC)**(Fig 1.12*(d)*): after the deposition on the substrate of the gate, and its coverage with the dielectric, source and drain are deposited, finally, the OSC is deposited.

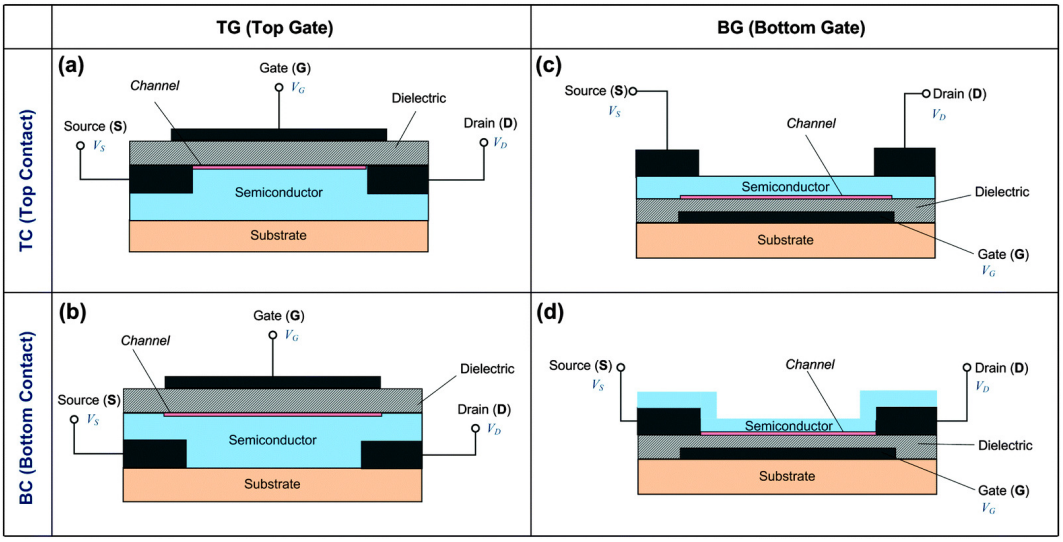

Figure 1.12: *Schematic cross-section of four configurations of organic transistors. Panels (a) and (b) are top-gate (TG) configured, with top-contact (TC) and bottom-contact (BC) configured source and drain electrodes, respectively. Panels (c) and (d) are bottom-gate (BG) configured, with TC and BC source/drain electrodes, respectively [36].*

In bottom-gate (BG) configurations the active material is directly exposed to the external environment. This can limit the performances, since usually organic semiconductors are quite sensitive to temperature, moisture, light and can be easily oxidized and degraded. For this reason the BG configuration is avoided with unstable OSCs. For a similar reason, bottom-contacts (BC) configuration avoid the deposition of metal contacts on top of the OSC usually related to high temperatures that can degrade the semiconducting molecules. The deposition of the dielectric is usually not a problem since polymeric materials can be used, and they can be processed by solution techniques. The configuration that offers more advantages, regarding the stability of the OSC is usually the TGBC one due to the limited exposure toward the environment. However, for the study of a new OSC usually the BGBC architecture is chosen. With this configuration, indeed, it is possible to prepare substrates with gate and contacts already deposited, thus, focusing the attention on the deposition parameters of the OSC and keeping the latter away from contamination or degradation due to further deposition steps.

1.5.2 Contact engineering

The injection barrier at the contact-OSC interface introduced in Section 1.4.1 is responsible for the origin of the so-called contact resistance (R_C), which is important for both the final performances of the device and the reliability of the extracted values of the field-effect mobility. In order to minimize the contact resistance, it is possible to apply a self-assemble monolayer (SAM) over the metal contacts [33]. The SAM is composed of organic molecules, usually characterized by a thiol group, able to be absorbed on the metal surface in a strong chemisorption regime, forming a covalent bond with the metal. These molecules modify the work function of the metal due to the formation of an interfacial dipole, thus changing the injection barrier [37]. It is important to note that the SAM modifies the interaction between the contacts and the OSC, thus can lead to a different crystallization morphology and change the transport properties in a detrimental way [30]. In Fig 1.14 an example of the beneficial effect of the SAM is reported. It is possible to notice that the SAM highly reduces the contact resistance (Fig 1.14*(d)*), increasing the output current and the ideality of the output characteristic (Fig 1.14*(b)* and *(c)*) [38].

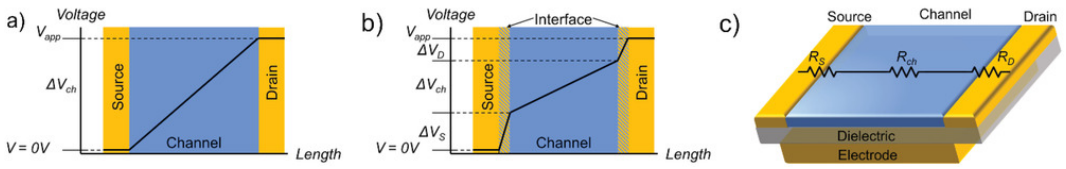

Figure 1.13: *a) Voltage profile of an ideal FET (R_C=0). No voltage is dropped at the contacts, $\Delta V_{CH} = V_{app}$. b) Voltage profile showing a real FET ($R_C \neq 0$) with voltage drops at the source and drain, leading to $\Delta V_{CH} < V_{app}$, shown as a reduced slope. c) The total FET resistance is a sum of three resistances connected in series: the source, channel, and drain resistances (R_S, R_{CH}, and R_D, respectively) [39].*

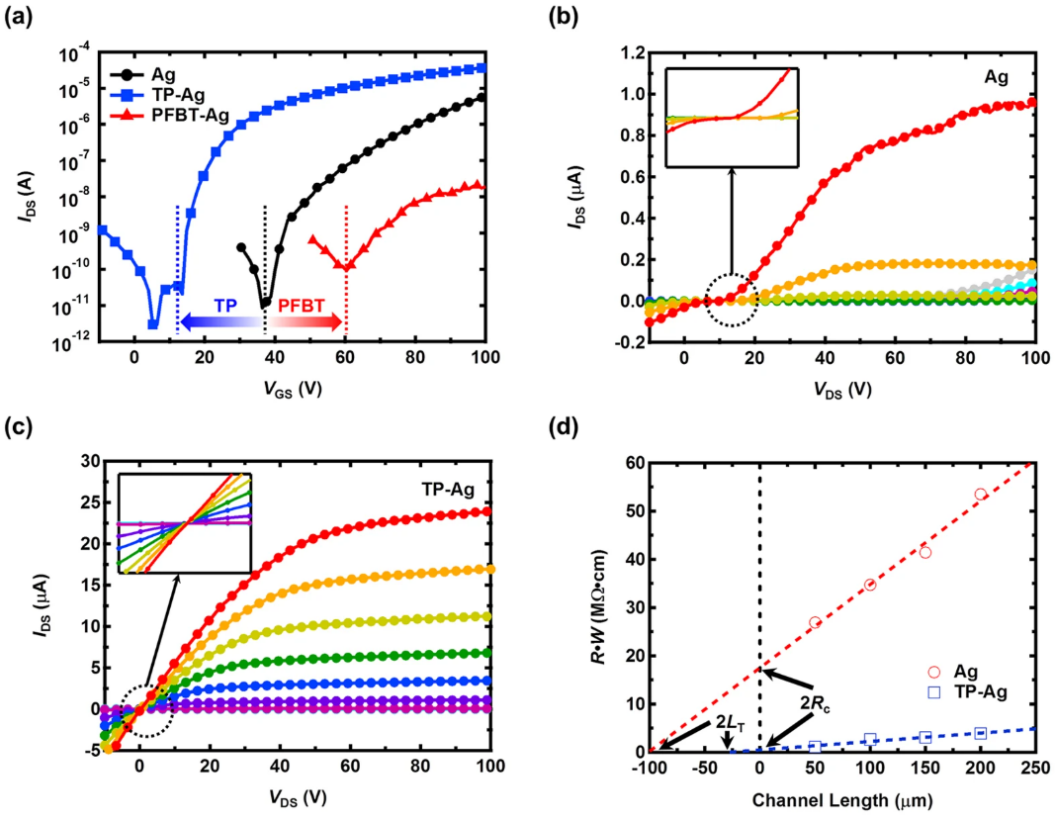

Figure 1.14: *Beneficial effect of a thiphenol (TP) SAM on a silver contact OFET: (a) Transfer characteristics of the all-solution-processed OFETs with and without SAM treatment. Output characteristic of the device (b) without SAM treatment and (c) with TP treatment. Output characteristics were obtained in the region of gate-to-source voltage from 0 V to 80 V with a 10 V step. (d) Width-normalized device resistance with respect to the channel lengths. [38].*

Chapter 2

Carbon atomic wires

Thanks to its chemical versatility, carbon has played a crucial role in science and technology advancement in the last 30 years [11]; in fact, its ability to adopt different hybridization states allows the production of a wide variety of allotropic forms: *sp*-, sp^2-, and sp^3-hybridized atomic orbitals give rise to linear, planar and three-dimensional organization. Fullerenes, nanotubes, and graphene demonstrate that carbon can form a great variety of structures whose properties are strongly related to structural issues such as dimensionality, hybridization, chirality and topology. More recently the research focussed on *sp*- and sp^2-hybridized carbon systems, these systems can sustain π-conjugation, which is the basis of the metallic properties of graphene and carbon nanotubes, and, a necessary property for organic semiconductors (OSCs). As graphene is today considered the ultimate 2-dimensional (2-D) system (1-atom-thick) showing peculiar electronic properties, carbon atomic wires (CAWs) represent a true 1-D system (1-atom diameter). Outstanding properties have been predicted by theoretical studies for CAWs [19] supported by experimental results obtained through the study of the charge transport properties in single isolated molecules [40]. In particular ballistic and oscillatory conductance, spin-dependent transport, and a strain-induced metal-to-insulator transition are predicted in *sp*-carbon atomic wires, making these systems promising candidates for the future of organic electronics.

2.1 -*sp* hybridization: polyynes and cumulenes

Considering an infinite CAW (sometimes called "carbyne" [41]), only two ideal different structures are possible: the so-called "**polyyne**" corresponding to a chain with alternating single and triple bonds ($-C\equiv C-C\equiv C-$) and the "**polycumulene**"

or "**cumulene**" which identifies the opposite case where an equalized geometry is formed by all double bonds (=C=C=C=C=) [42]. The first case can be described as an infinite 1D crystal with a basis of two carbon atoms showing a bond-length alternation (BLA) defined as the difference between the distance of the single and the triple bonds as shown in Fig 2.1.

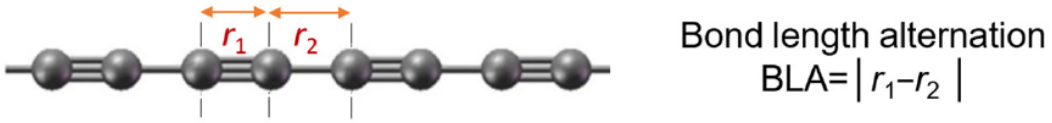

Figure 2.1: *Schematic representation of the bond length alternation (BLA) in a polyyne [41].*

Cumulenes, on the other hand, are characterized by a BLA=0. The importance of the BLA parameter is related to the degree of π-electron conjugation displayed by CAWs. Polyynes show semiconductor properties while cumulenes are metallic and this behavior is indeed directly related to their structure, with a strong structure–property relationship [43]. Polycumulene turns out to be unstable due to *Peierls distortion*, thus, the polyynic structure is expected to be the only stable form for infinite relaxed chains.
Peierls' theorem states that a one-dimensional equally spaced chain with one electron per ion is unstable [44]. The atoms in the lattice rearrange slightly, moving from an equally-spaced crystal to one in which the spacing alternates, in other words, the atoms rearrange in pairs. This is called "dimerization", and costs some elastic energy, since for identical atoms the lowest state must be one of equal spacing. However, the electrons are able to move to a lower energy state by this maneuver. Hence, the resulting lowest energy structure is polyynic and it is characterized by: a BLA$\neq$0, the presence of a band gap between the completely filled valence band and the empty conduction band (semiconducting behavior), and an optical phonon branch. In contrast, the cumulene geometry would be characterized by a BLA=0, a closed band gap with an half filled valence/conduction band and the absence of the optical phonon branch. These two configuration with the respective properties are shown in Fig 2.2.

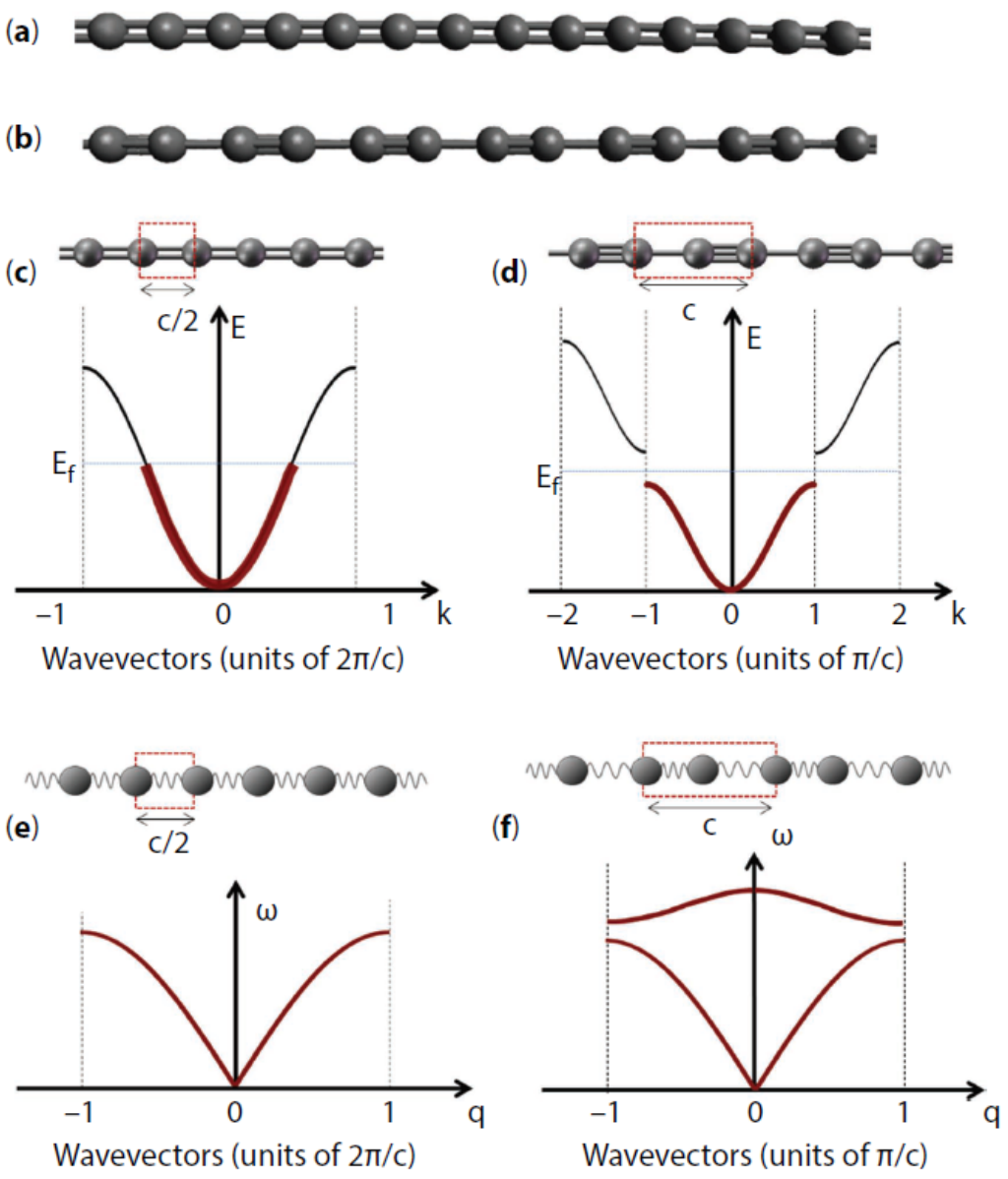

Figure 2.2: *The two structural configurations of carbyne: (a) cumulene and (b) polyyne. The electronic band structure and phonon dispersion relation are shown for cumulene (c–e) and polyyne (d, f), respectively. [43].*

2.2 End-groups

As a matter of fact, the ideal infinite CAW does not exist. Furthermore, CAWs are highly reactive and were only syntesized inside carbon structures (graphite, amorphous carbon, fullerenes, carbon nanotubes or graphene) or with end-groups able to isolate the chain [41]. The latter approach is particularly promising because terminating groups have multiple beneficial effects. As already said, the end-capping moieties are able to isolate the chains one from another, reducing the possibility of cross-linking and the consequent degradation. Moreover, the end-groups affect significantly the structure of the *sp*-domains, and tune the related electronic, optical, and spectroscopic properties.
First of all, the finite carbon chain present different electronic properties with respect to the infinite carbyne. Theoretical works on hydrogen-capped polyynes predict a decreasing value of BLA and energy gap with increasing chain length [11]. Furthermore, based on the type of chemical coordination to the chain, the capping molecules could induce a well-defined structure, promoting a cumulene-like or polyyne-like organization. For instance, capping the chain with specific molecules that create a true double bond with the adjacent carbon atoms, give raise to a "domino effect" through the *sp* carbon domain, forcing the chain to have a cumulene-like geometry. This leads to a low value of electronic gap and the consequent semiconducting behaviour. Finally, the end-groups define the solubility and the crystallization properties of the molecule, fundamental parameters for the application of these systems in solution-processable organic field-effect transistors (OFETs).

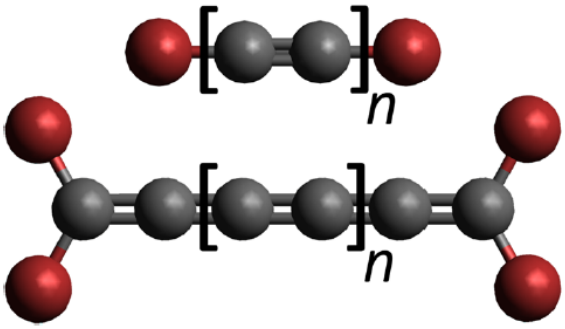

Figure 2.3: *Schematic representation of the structure of a "polyyne-inducing" (above) and "cumulene-inducing" (below) end-groups in sp-carbon chains. The red spheres represent the general functional end-group [41].*

2.3 Charge transport properties

The vast majority of the papers related to charge transport in CAWs are focused on intramolecular transport [11, 45], and very few comprise experimental evidences [40]. Nonetheless, starting from intramolecular charge transport properties, it is possible to get an insight of the reason why CAWs can be good candidates for OFETs.

As already introduced CAWs display high degree of π-electron delocalization and π-conjugation. The electronic behavior is strictly dependent on the conjugation properties, thus CAWs are an extremely interesting system for organic electronic applications. Generally speaking, long molecules conduct electricity through themselves less well than short ones [45]. The conductance G can be expressed as:

$$G =\propto e^{-\beta L} \tag{2.1}$$

where L is the molecular length and β is an attenuation factor. β is usually in the range of 0.2-0.5 Å^{-1} for a conjugated organic π-system, but, in the case of molecules with BLA$\approx$ 0, β becomes close to zero or even negative [45]. Cumulenes are the simplest type of neutral π-system not to exhibit substantial BLA and this makes them the perfect candidate for intramolecular charge transport. Additionally, CAWs offer an approximately cylindrical distribution of electron density along their one-dimensional backbone [46]. In contrast, more commonly employed structures used in organic and molecular electronics are composed by linearly-fused benzene rings which display an interruption of π-conjugation upon twisting. This property is particularly promising for their application in single molecule electronics, but can be a strong point also in organic electronics where, as already said in Section 1.3.1, the transport efficiency is highly influenced by the molecular orbital overlap.

2.4 Stability

The main problem of CAWs is related to their stability. The *sp*-carbon chains have to be isolated from one another by means of carbon structures or end-groups, in order to avoid crosslinking. Even if it is possible to obtain stable chains at room temperature, crosslinking is difficult to avoid upon irradiation or at high temperatures. The most common degradation mechanism in cumulenes is the thermal dimerization, a formal cycloaddition reaction, between two molecules (reported in a schematic example in Fig 2.5) [47], but also trimerization, involving three molecules, has been reported in one work [48].

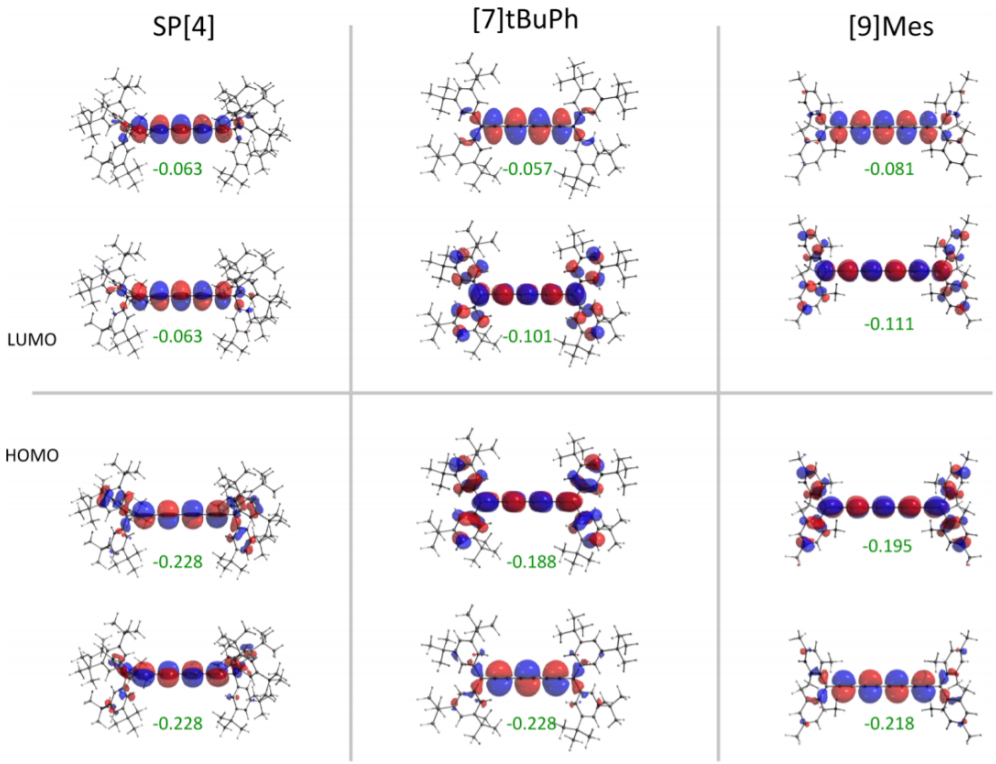

Figure 2.4: *Frontier orbitals of SP*[4] *polyyne (left column),* [7]*tBuPh (central column), and* [9]*Mes cumulene (right column), from DFT calculations with the respective energies of the orbitals, reported in atomic units [49].*

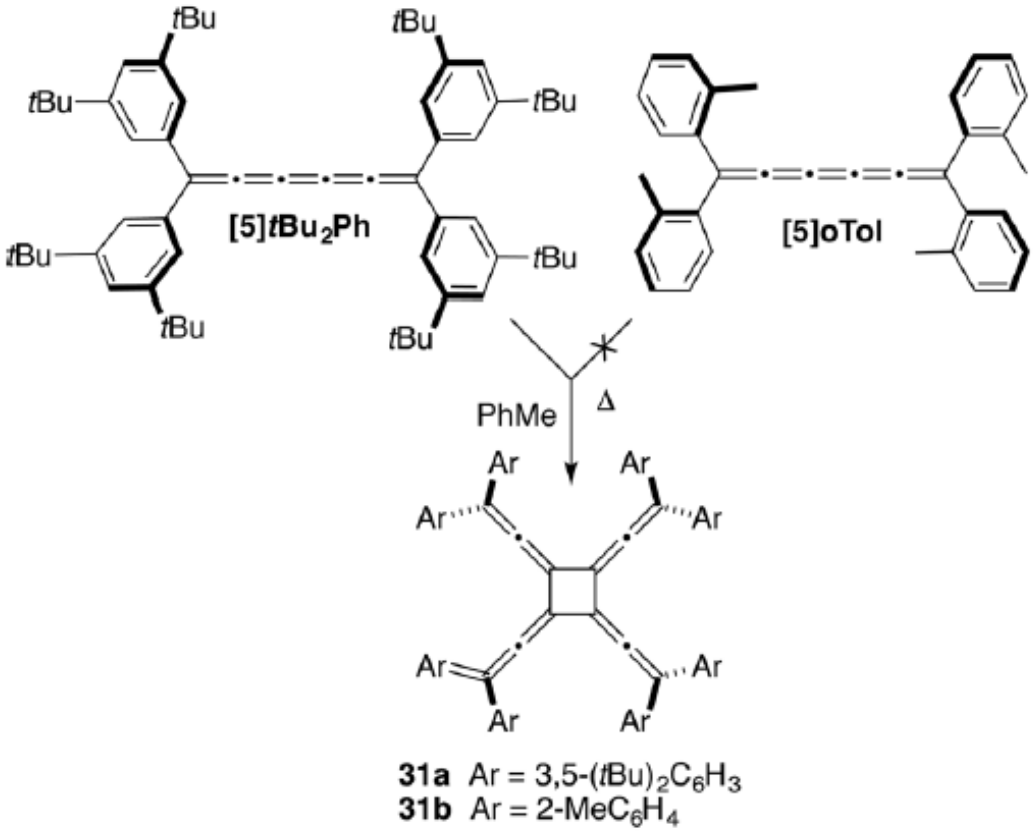

Figure 2.5: *Example of thermal dimerization between two [5]cumulene molecules [47].*

Chapter 3

Design of experiments and machine learning

During the study of a material, the main objective is usually to predict and optimize one of its properties. However, the experimental process required to achieve this objective is often difficult and time-consuming, especially when a fundamental understanding of the chemistry or physics behind the property is lacking [3].
Usually, the experimentalist has to perform many experiments and evaluate the system response, trying to understand the cause-effect relationship. The system response can be described as a "black-box" function, i.e. a function that does not have a closed-form representation, does not provide function derivatives, and only allows point-wise evaluation [50]. The experimentalist performs point-wise evaluations by choosing the fabrication or simulation parameters and observe the system response by measuring the dependence of the chosen property ("output") on the "input".
In the field of materials optimization, the property to be optimized is often influenced by a large number of factors and, for this reason, it is hard to find a model able to take into account all these dependencies. The usual approach is to perform a large number of experiments changing one variable at a time (OVAT) until the required performances are achieved. This approach, however, is highly inefficient and can be seen as a "blind" search over the black-box function of the system response.
Machine learning-assisted methods, combined with experimental design, on the other hand, offer a powerful and efficient alternative to this kind of optimization problems. Indeed, this approach uses fitting techniques able to approximate the "black-box" response function. The predicted function can then be plotted, pro-

viding the experimenter a better visualization of the outcome, thus, allowing the design of a smarter experimental route, reducing costs both in terms of money and time. In addition, when some physical or chemical insight is present, the additional information can be included in the model, providing a more powerful (and physically meaningful) prediction. Ultimately, in some specific cases, machine learning techniques can be not only good in interpolating the data but can be used in order to make extrapolations and, thus, prediction outside the input data domain [51].
The field of machine learning-assisted optimization has seen a growing interest in the field of materials optimization and discovery in recent years. This is probably due to the fact that machine learning algorithms are becoming more available and user-friendly [3].
In the field of material research, machine learning has been used in two main different ways:

- as a tool for classifying and interpolate a large number of data taken from existing databases in order to make predictions and **discover** new kind of materials [51, 52].
- as a way to guide experiments starting from experimental design without relying on external data in order to **optimize** the required material properties [3, 50, 53].

In both cases machine learning has proven to be an extremely useful tool, able to exclude preconceived bias or notions, enabling a "big picture" vision. With this tool, indeed, the experimentalist is able to "*leave a narrow valley of one-dimensional data and view the landscape from a mountain ridgetop*" [3].

3.1 Design of experiments

Every experiment has two components [54]: a measurable **outcome** which is the *response* of the experiment, that is, in general, the quantity to optimize or predict; and one or more **variables** or **factors**. The factors can be *numerical* (quantitative), if quantifiable by measurements, or *categorical* if qualitative and not orderable.

In academic laboratories, the usual strategy to experimentation is the OVAT approach [3]. While this technique does not confound the roles of different factors, it is time-consuming and rarely results in discovery of optima. The design of

experiments (DoE) approach, instead, enables the experimentalist to sample a large, multidimensional *parameters space* in a rational manner, greatly decreasing the number of experiments while keeping an high level of obtainable information. The general approach during DoE, is to subdivide the numerical factors (i.e. parameters) in different *levels* and construct a grid in the parameters space. Each experiment will be characterized by a unique set of variables, each one with its own levels. In order to sample the parameters space, different designs are possible, the most used ones are *full factorial*, *fractional factorial* and *latin square* (or *latin hypercube*) design. In full factorial design (Fig 3.1*(a)*) all the possible combinations of parameters are tested. It yields the highest fidelity but requires an unfeasibly large number of experiments. Assuming the same number of levels for each parameter, the number of experiments required in this design scales as:

$$N = L^P \tag{3.1}$$

where L is the number of levels and P the number of parameters. In fractional factorial design (Fig 3.1*(b)*) the number of experiments is reduced as a fraction of the full factorial design, the level of fidelity remains relatively high while the number of experiments is strongly reduced. Finally, in the latin square design (Fig 3.1*(c)*) each parameter level is tested only once, the number of experiments is reduced at its minimum but the fidelity obtained is very low. In this design the number of experiments simply scales as

$$N = L \tag{3.2}$$

thus, it does not depend on the number of parameters.

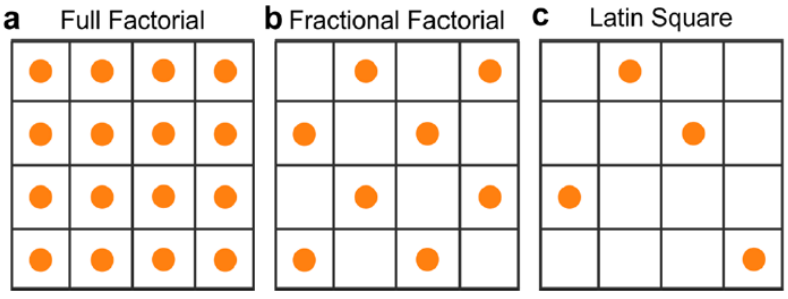

Figure 3.1: *Examples of factorial sampling in two-factor 4-level system showing (a) full factorial, (b) fractional factorial, and (c) Latin square design. [3].*

Each of these designs has its own advantages and is more suitable for one of the three main experimental stages [54]:

- **Screening**: phase aiming at getting a better understanding of the system, identifying the suitable range for each factor and isolating the important effects. It generally uses a *latin square* design or a *fractional factorial* design with a strong fraction, able to test a large number of factors in a fast way.
- **Sequential experiments**: second run of experiments based on the information obtained during the screening phase. It aims at increasing the resolution and identifying the main effects and the factor interactions. A *fractional factorial* design is generally used.
- **Optimization**: once the main effects and factor interactions are known, it is possible to use a higher resolution in order to increase the predictive precision and optimize the outcome. The precision required is achieved with a *fractional factorial* design with a low fraction or with a *full factorial* design.

Once the experiments are performed, it is possible to use machine learning techniques in order to fit the data and obtain predictive curves able to guide the experimentalist towards the optimization of the system.

For instance, take a simple material or a device to optimize that has two uncorrelated parameters, like the one seen in Fig 3.2*(a,b)* [3]. The blue cloud represents the region of best/optimum performance that the experimentalist would like to find. Following the OVAT approach, one of the two parameters would first be chosen to be *screened* (green line). Successively, the experimentalist would take the optimum on the green line as the starting point for orthogonal screening of the second variable (orange line). In this simple example, with a sequential experimental approach, the experimentalist would find the optimum as this approach does locate the center of the blue region that represents best performance or characteristics.
For more complex systems with greater number of parameters or correlations, this simple experimental approach would require a larger number of experiments and yet could miss the optimum, as demonstrated in Fig 3.2*(c,d)*. In the first series of tests (shown in green), the experimentalist observes a maximum, but unlike the previous uncorrelated system shown in Fig 3.2*(a,b)*, starting from this maximum the orthogonal second set of experiments (orange line) does not yield the

optimum value for the system. The experimentalists could be self-deceived into thinking that they had found the best performance, when in fact, they did not. This method cannot reveal if the actual maximum has indeed been found because a simple OVAT optimization approach reveals little about correlations between the system parameters.

Considering the case where the experimentalist tackles the same correlated system, but instead of choosing points on lines via serial optimization, they choose specific points in parameters space using DoE principles, where the points are distributed orthogonally and evenly like those found in Fig 3.2*(e)*. With the data from these points, data analysis techniques from machine learning can be used to build a map of the whole parameters space (Fig 3.2*(f)*), instead of only having linear series of data along a small number of lines (directions). This map from the first six experiments also does not currently contain the maximum, but it shows an *area of interest* and reveals correlations between the parameters. At this point, the experimentalist would use this map to design a second set of experimental points focused on the area of interest. Continuing in this way, the experimentalist will likely find the system optimum, with an arbitrary degree of confidence.

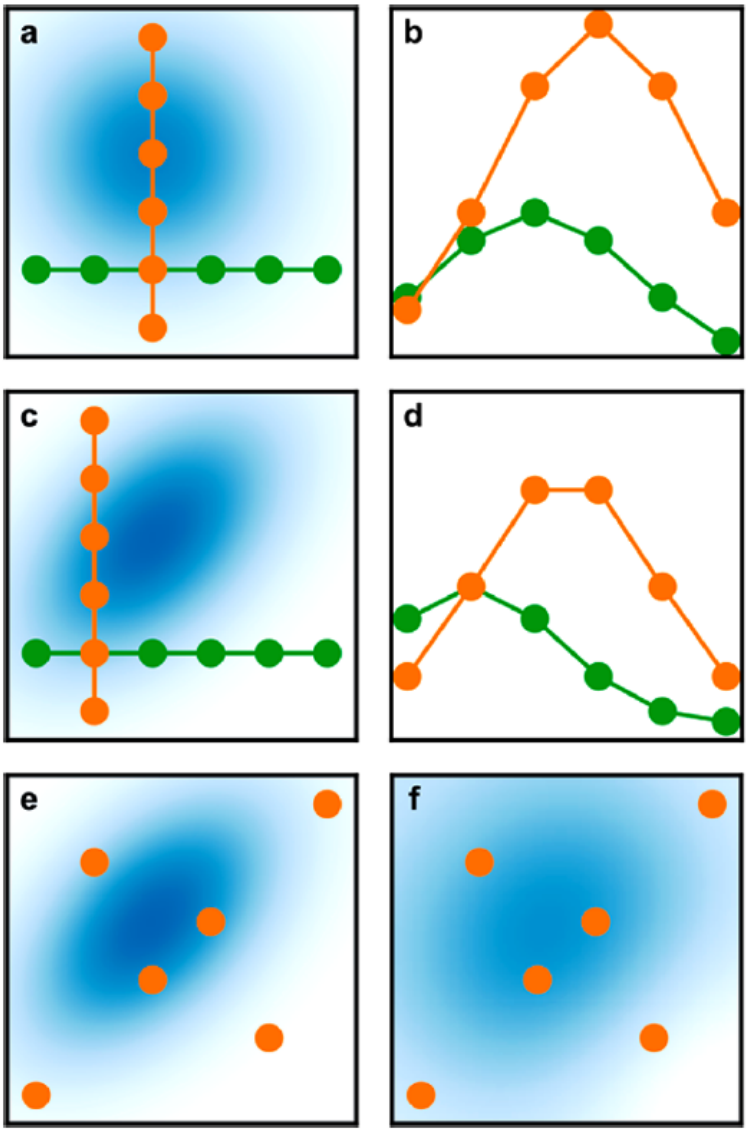

Figure 3.2: *Optimization of a two-factor system: DoE vs OVAT. (a,c,e) Map of the true values (blue gradient) of the outcome as a function of the two input parameters (horizontal and vertical axes). (a,b) OVAT sampling of an uncorrelated system will generally lead to finding the optimum value of the outcome. (c,d) OVAT sampling of a correlated system will generally not result in finding the optimum value of the outcome. (e) DoE approach with orthogonal sampling of a correlated system. (f) Approximation of the true outcome map produced by machine-learning fitting methods applied to the six data points acquired by DoE in (e). [3].*

3.2 Machine learning

Machine learning is the study of computer algorithms that improve automatically through "experience". In order to make predictions, machine learning algorithms build a mathematical model based on sampled data, known as "training data" without being explicitly programmed for the specific problem.
There are many different machine learning algorithms, the one used in combination with DoE is usually *supervised regression*. *Supervised learning* implies that the training dataset is composed by both the inputs, in the form of labeled variables (also called *features*), and the output, in the form of the experimental outcome. *Regression analysis* aims at fitting a multidimensional curve on the data, this curve should be able to predict and forecast the outcome of an experiment based on the input parameters.

3.2.1 Linear regression

Undoubtedly, the simplest case of regression is the "one-variable linear regression". In this case the objective is to fit a straight line to a set of data composed of one variable and one outcome ((x_D^1, y_D^1), (x_D^2, y_D^2), ... (x_D^m, y_D^m)). The point from the dataset will be denoted with a subscript "D". This data can be plotted, as a set of points, in a x-y plane, where the horizontal axis represent the value of the variable and the vertical axis the outcome value. The fitted line will predict the outcome given a generic variable.
In general the data will not be aligned, thus, the fitted line will present a certain degree of error, the aim is to find the line parameters which minimize the error.
A straight line is described by the following equation:

$$\hat{y} = \omega_0 x + b \tag{3.3}$$

where ω_0 is the slope, b is the intercept, x is the generic input variable and $\hat{y}$ the predicted outcome. In order to "fit" the line it is necessary to define the error. There are many ways to calculate the error, one of the most commonly used is the mean squared error (MSE) function, defined as:

$$MSE = \frac{1}{2m} \sum_{i=1}^{m} (\hat{y}_D^{(i)} - y_D^{(i)})^2 \tag{3.4}$$

where the sum is over the points of the dataset (numerated from 1 to m), $\hat{y}_D^{(i)}$ is

the predicted outcome calculated from the input $x_D^{(i)}$ of the dataset, $\frac{1}{2m}$ is a scaling factor, and the term $(\hat{y}_D^{(i)} - y_D^{(i)})$ is called *residual* and is the difference between the predicted value and the actual value taken from each data point (represented in Fig 3.3 as red line).

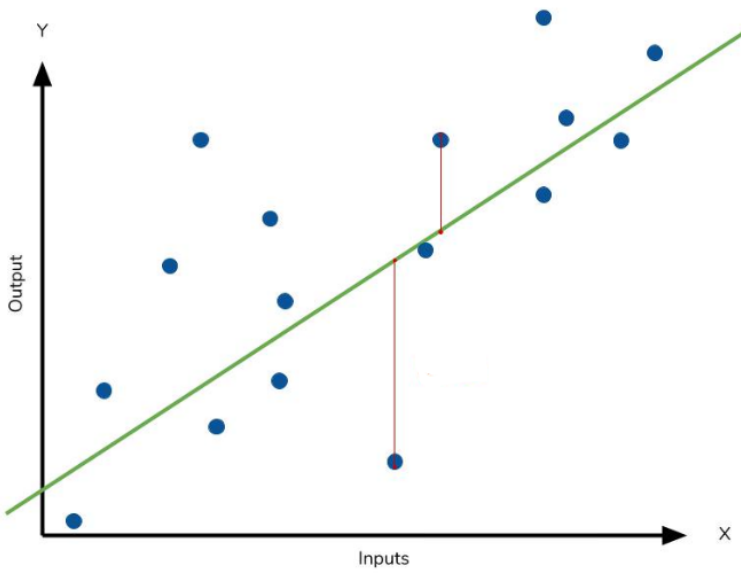

Figure 3.3: *Example of linear regression: the blue dots are the data, the green line is the fitted line and the residuals are graphically represented, for two points, as red lines.*

Substituting Eq 3.3 in Eq 3.4 we obtain the expression for the so-called "loss function":

$$J(\omega_0, b) = \frac{1}{2m} \sum_{i=1}^{m} ((\omega_0 x_D^{(i)} + b) - y_D^{(i)})^2 \tag{3.5}$$

Now it is possible to minimize J, and thus the error, as a function of the line parameters ω_0 and b. There are many ways to do that. A very simple and intuitive one is to use *gradient descent*. Gradient descent is an iterative approach which can be expressed as:

$$\omega_0' = \omega_0 - \alpha \cdot \frac{\partial J(\omega_0, b)}{\partial \omega_0}$$
$$b' = b - \alpha \cdot \frac{\partial J(\omega_0, b)}{\partial b} \tag{3.6}$$

During each iteration the value of ω_0 and b is updated in the direction that minimize J. α is a tunable parameter that governs the step of the descent. With low values of α the descent will be slow and will take many iteration, while with a value too large process may diverge and thus be unable to minimize the error. A visual representation of this process is shown in Fig 3.4 where three iteration steps are reported (1, 6 and 16). The parabola represents the error J as a function of ω_0 with the black dots being the error value for each iteration. On the right are reported the data points and the resulting fitted straight line.

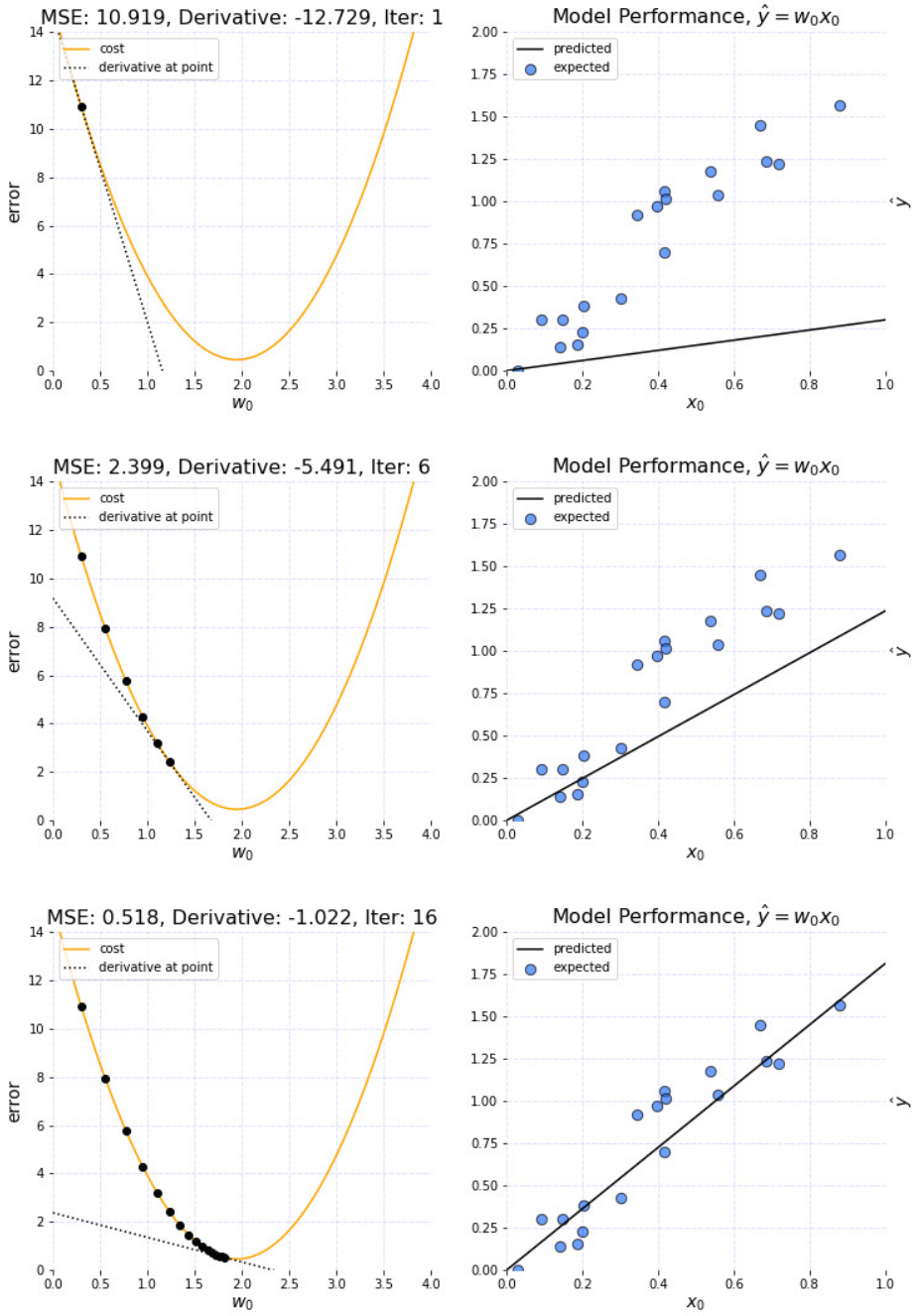

Figure 3.4: *Example of linear regression using mean squared error and gradient descent: the iterative process is represented from top to bottom (iteration 1, 6 and 16).*

3.2.2 Support vector regression

Not every problem has a single input variable or is well fitted by a straight line, for this reason different kinds of regression models were developed. During the last two decades, the machine learning research focused on the study of support vector machines (SVMs).
SVMs are a set of supervised learning methods used for classification, regression and outliers detection [55]. SVMs can be extended to solve regression problems. This method is called support vector regression (SVR).

The working principle of SVR is similar to the one of linear regression explained above. The main difference lies in the loss function and in the use of a *kernel* which allows the fitting of functions different from straight lines.
As for the the linear regression, the aim of SVR is to predict a scalar observable $\hat{y}$ (the outcome) as a function of one of more variables [56]. If more than one variable is present, it is possible to express them in a vector $\boldsymbol{x}$, this will increase the problem dimensionality and the obtained curve will lay in a space with dimension equal to the number of variables + 1. In the case of *linear* SVR the resulting curve will be an "hyperplane", and, similarly to Eq 3.3, will be described by:

$$\hat{y} = \langle \boldsymbol{w} \cdot \boldsymbol{x} \rangle + b \tag{3.7}$$

$\boldsymbol{w}$ is a vector containing the curve parameters (also called *weights*), $\langle \cdot \rangle$ represent the dot product, and b is similar to the intercept for the case of linear regression but, in this context, is called *bias*. The final objective is to find the parameters $\boldsymbol{w}$ and b that minimize the *risk functional*:

$$R = \frac{1}{2}\|\boldsymbol{w}\|^2 + C\sum_{i=1}^{m} |\hat{y}_D^{(i)} - y_D^{(i)}|_\epsilon \tag{3.8}$$

where $\|\boldsymbol{w}\|^2$ is the square of the euclidian norm of the vector $\boldsymbol{w}$, thus, nothing else than the sum of the squares of its components, C is a positive constant and $|\hat{y}_D^{(i)} - y_D^{(i)}|_\epsilon$ is the ϵ-insensitive loss function defined as:

$$|\hat{y}_D^{(i)} - y_D^{(i)}|_\epsilon = \begin{cases} |\hat{y}_D^{(i)} - y_D^{(i)}| - \epsilon & \text{for } |\hat{y}_D^{(i)} - y_D^{(i)}| \geq \epsilon \\ 0 & \text{otherwise} \end{cases} \tag{3.9}$$

In the case of SVR, the risk functional has a slightly deeper meaning than the

simple loss function used in linear regression. Indeed, the objective is not only to minimize the error by means of the loss function, but also ensure that the fitted curve is as smooth as possible. For this reason also the term $\|\boldsymbol{w}\|^2$ has to be minimized. The constant C determines the trade-off between the training error and the "smoothness" of the function.

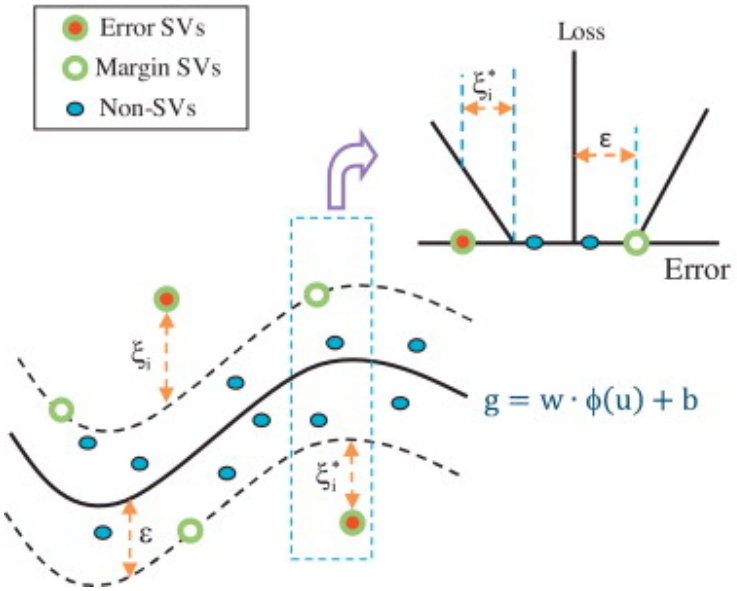

Figure 3.5: *One-dimensional nonlinear SVR with ϵ-insensitive loss function: only the points outside the ϵ margin contribute to the error [57].*

Finally, in order to fit functions different from the trivial straight line, the *Kernel* method has to be introduced[1].
Instead of acting on the curve parameters $\boldsymbol{w}$ the Kernel method "maps" each input data $\boldsymbol{x}_D^{(i)}$ into a higher dimensional space using a specific transformation dictated by the kernel function [58]. In the higher dimensional space, the data are fitted with a linear model, as described above, and then mapped back. The final result is a non-linear curve obtained without the computational expense of fitting complex functions.
There are many kernel functions available, the most common ones are reported in Table 3.1.

[1]Here just an intuitive description of the Kernel method is reported, for a more rigorous approach refer to Appendix A.

Function	**Expression**	**Parameters**
Linear	$k(\boldsymbol{x}_D, \boldsymbol{x}) = \langle \boldsymbol{x}_D, \boldsymbol{x} \rangle$	
Polynomial	$k(\boldsymbol{x}_D, \boldsymbol{x}) = (\gamma \langle \boldsymbol{x}_D, \boldsymbol{x} \rangle)^d$	γ, d
RBF	$k(\boldsymbol{x}_D, \boldsymbol{x}) = exp(-\gamma \lVert \boldsymbol{x}_D - \boldsymbol{x} \rVert^2)$	γ

Table 3.1: *Table reporting three of the most common kernels.*

With a radial basis function (RBF) kernel, the algorithm will fit best to Gaussian-shaped features that would normally be found in cases of optimization [3]. For this reason, RBF was the kernel selected for this work. The parameter d determines the degree in the polynomial kernel while γ, present in many kernels, defines the range of influence that a single training point $\boldsymbol{x}_D^{(i)}$ has. Two data points close to each other in the parameters space will have a concomitant influence on the fitting, particularly if a small γ is chosen for the fitting.

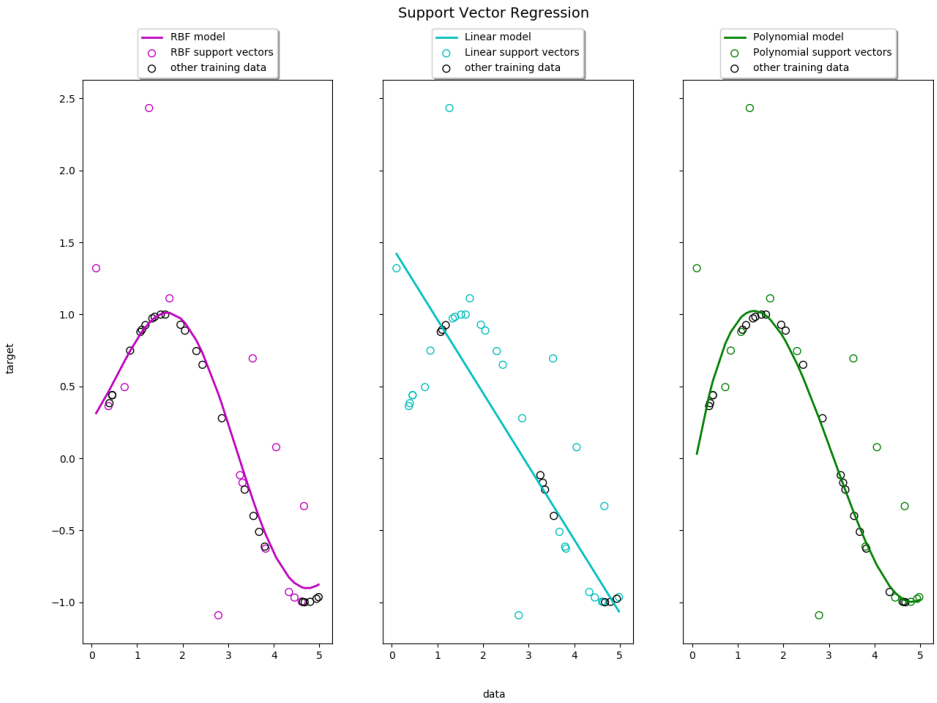

Figure 3.6: *Example of SVR using three different kernels: from left to right RBF, linear and polynomial kernel [55].*

3.2.3 Hyperparameters tuning

In the previous section some key parameters were introduced: ϵ, γ and C, along with the *Kernel function*. These parameters are called *hyperparameters* and are constant and independent from the dataset, thus, have to be tuned "manually" in order to optimize the fit.
It is possible to distinguish between three fitting regimes (Fig 3.7):

- **Underfitting**: the curve is not able to fit the input data nor to predict in a reliable way new data.
- **Overfitting**: the curve fit the data with minimal error, although is not able to predict new data in a reliable way. It is too specific for the input dataset.
- **Optimal fit**: the curve fit the data with low error and is still able to generalize and thus predict new data in a reliable way.

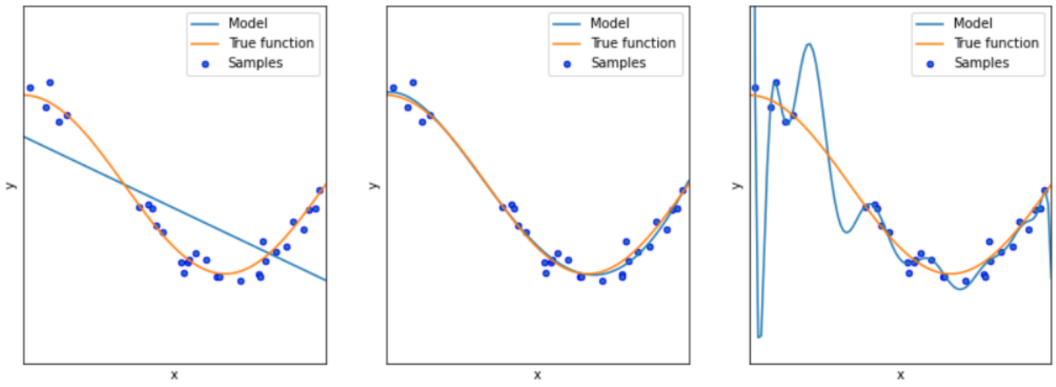

Figure 3.7: *Representation of the three fitting regimes for a one-dimensional non-linear regression (fitted curve reported in blue): from left to right underfitting, optimal fitting and overfitting.*

The general approach to understand the fitting regime is to subdivide the dataset in *training* set and *test* set. In this way, it is possible to "train" the model with the training set and test its performances with the test set. By changing the hyperparameters and the kernel it is possible to govern the fit and, by plotting the training and test error, it is possible to find the optimal value for each parameter. A table reporting the effect of each SVR hyperparameter on the fitting is reported in Table 3.2.

Parameter	**Effect**	**Too high**	**Too low**
γ	Governs the range of influence of each training data	Minimal range, the curve is fitted only very close to the training point (overfitting)	The range of influence of each training point gets confounded with the others, resulting in a smooth curve (underfitting)
C	Governs the smoothness of the curve	The curve is too peaked (overfitting)	The curve is too smooth (underfitting)
ϵ	Governs the tolerance of the model on the noise of the data	The fit consider all the data as noise (underfitting)	The curve fit also the noise that may be present in the data

Table 3.2: *Table reporting the influence of the hyperparameters and the effect of a bad tuning.*

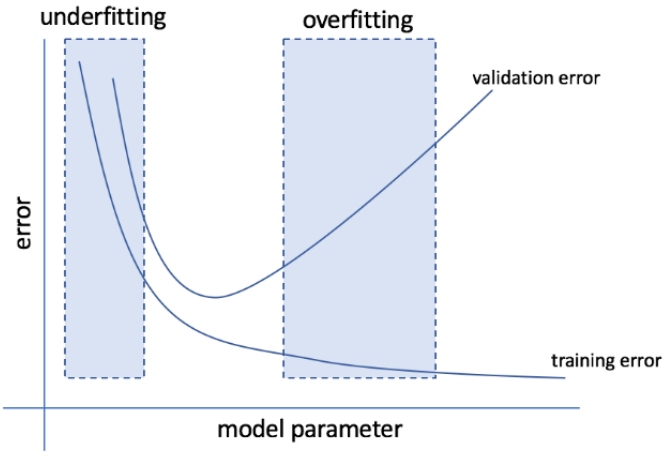

Figure 3.8: *Representation of the error for the three fitting regimes: underfitting is characterized by an high error both in the training set and test set (validation set), overfitting has an low error for the training set and an high error for the test set and, finally the optimal fit has a low error for both training and test set.*

In order to avoid the possibility of a "lucky" train/test set subdivision, the usual approach is to use a technique called *cross-validation*. Cross-validation consists in iterating the train-test set split many times and test the model for each different subdivision. The final result is an average error that exclude the possibility of testing on a "lucky" test-set. This approach is schematized in Fig 3.9. The split of the data is arbitrary, however, increasing the number of subdivisions increase the cross-validation efficiency. A high number of splits although requires a high number of iteration and can thus result in long computational times. Due to the small dimension of the training set, in this work, the finest cross-validation, called "leave-one-out" cross-validation, was adopted. In this approach, the test set is composed by a single sample and the number of iteration is equal to the size of the dataset.

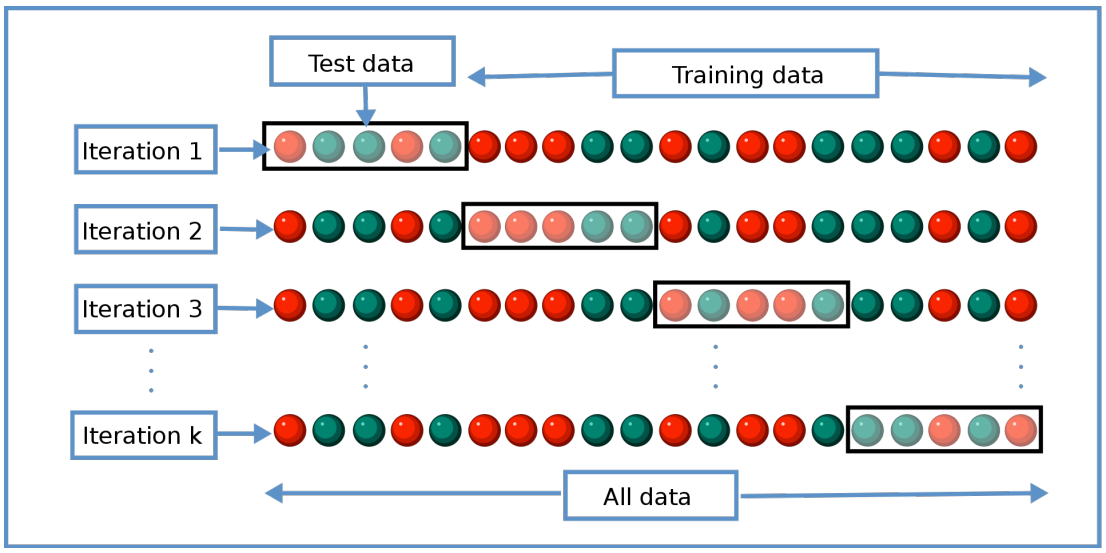

Figure 3.9: *Schematization of the cross-validation technique: the entire dataset is divided in a different train and test set for each iteration.*

3.2.4 Bayesian optimization

In classical experimental design, modelling and optimisation are separate processes, but newer model-based approaches can potentially sample more efficiently by adapting to the response surface, and can incorporate optimisation into the modelling process [50]. Bayesian optimization (BO) is an iterative process which uses a model-based approach with an **adaptive sampling** strategy to minimise the number of function evaluations (experiments). For these reasons it is perfectly suited for the optimization of expensive "black-box" systems. Moreover, compared to the SVR strategy discussed in Section 3.2.2, it does not require the experimentalist to "read" the fitted curves, thus allowing a higher dimensional optimization comprising a larger number of variables.
BO is based on two main ideas: a **Gaussian process (GP)** to fit the data; and an **acquisition function**, which, based on the GP prediction, returns the most promising set of parameters for the next experiment.
Given a set of observations, a GP regression returns a "posterior distribution", that is, a normal distribution with mean $\mu^{(t)}(\boldsymbol{x})$ and uncertainty $\sigma^{(t)}(\boldsymbol{x})$ at each point $\boldsymbol{x}$ in the parameters space. Where $\boldsymbol{x}$ is the generic set of parameters and the superscript "(t)" indicates that the function gets "updated" when new experiments are performed during the adaptive sampling. An **acquisition function** is then derived from $\mu^{(t)}(\boldsymbol{x})$ and $\sigma^{(t)}(\boldsymbol{x})$ of the GP model. The acquisition function allows a balance between *exploitation* (sampling where the objective mean μ is high) and *exploration* (sampling where the uncertainty σ is high), and its global maximiser is used as the next experimental setting. In Fig 3.10 an example of a GP regression and its associated acquisition function is reported, while in Fig 3.11 is schematized the general BO iterative process.

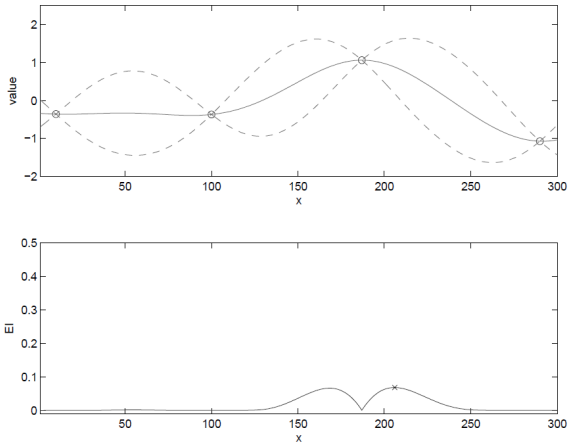

Figure 3.10: *The upper panel shows the Gaussian process (GP) model in a problem with a one-dimensional input space: the circles are previously measured points, the solid line is the GP mean $\mu^{(t)}(\boldsymbol{x})$, and the dashed lines are at $\mu^{(t)}(\boldsymbol{x}) \pm 2\sigma^{(t)}(\boldsymbol{x})$. The lower panel shows the acquisition function (Expected improvement $EI(\boldsymbol{x})$) computed from the GP model. An "x" marks the point with the largest expected improvement, which indicates where the next experiment will be performed. [53].*

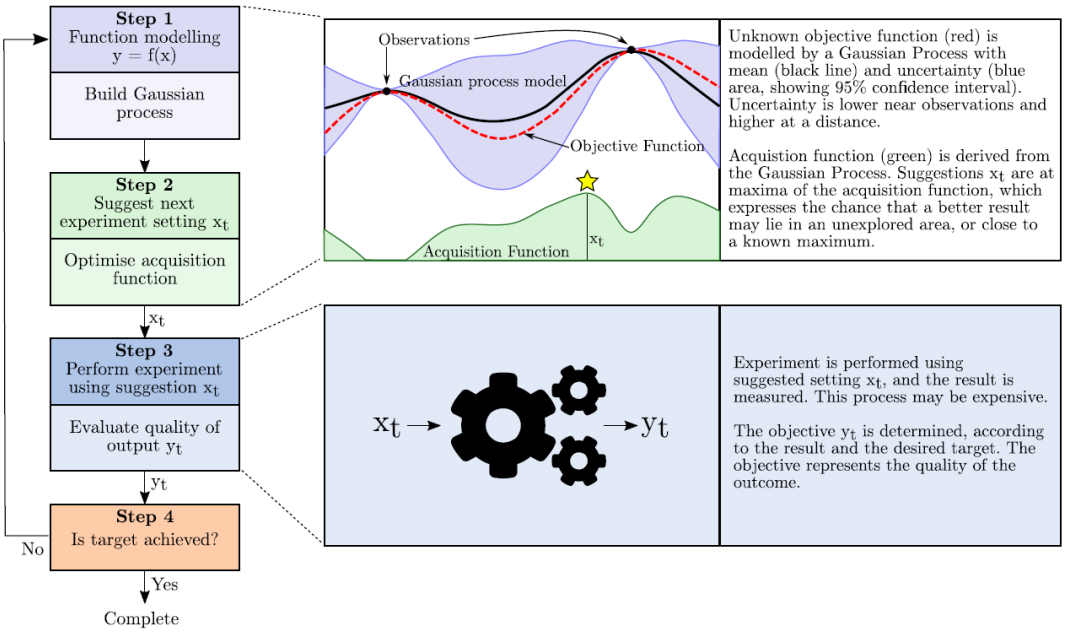

Figure 3.11: *Schematization of the iterative process of bayesian optimization [50].*

Chapter 4

Materials and methods

4.1 Materials

In order to validate and compare bayesian optimization (BO) and support vector regression (SVR) guided approaches, top-gate bottom-contacts (TGBC) organic field-effect transistors (OFETs) were fabricated using a well known semiconductive polymer (P(NDI2OD-T2)) as active material. The same Machine learning approach was then used to guide future experiments for a cumulenic system (tetraphenyl butatriene) based on experimental data taken from previous works of Printed and Molecular Electronics (PME) group [14, 19].

4.1.1 N2200

P(NDI2OD-T2), also known as ActivInk "N2200", is an organic semiconductor (OSC) produced by Flexterra, formerly Polyera, whose chemical structure is shown in Fig 4.1.
This OSC is a preferential electron conductor (n-type OSC) characterized by an highest occupied molecular orbital (HOMO) and lowest unoccupied molecular orbital (LUMO) levels around $-4\ eV$ and $-5.6\ eV$ respectively [59] and mobilities exceeding 1 $\frac{cm^2}{V \cdot s}$ [31]. N2200 tends to pre-aggregate when dissolved in specific solvents, forming a liquid-crystalline like phase, and this property can be exploited in order to obtain higher mobility OFETs. Indeed, it was demonstrated that, by means of off-center spin coating, it is possible to maintain the long-range order and obtain extended orientational domains of hundreds of micrometers in the deposited film [31]. As discussed in Section 1.3.3, the ordered molecular packing favours the charge transport leading to higher mobilities. In the case of N2200,

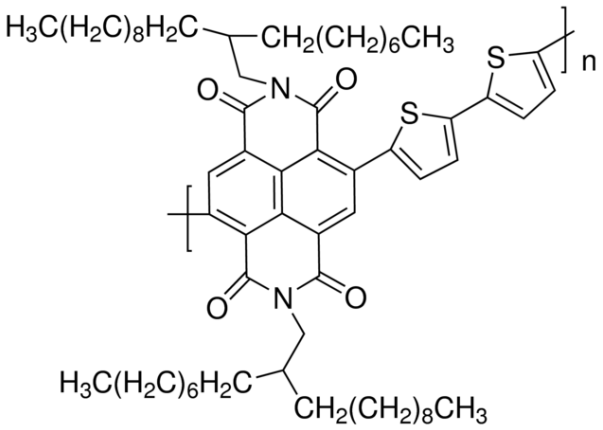

Figure 4.1: *Chemical structure of N2200.*

the increase in mobility values in the direction parallel to the domains alignment is due to a faster intrachain transport parallel to the polymer backbone [60]. The domain size depends mainly on two factors [61]:

- **Molecular interaction between the polymer and the solvent**: it governs the degree of pre-aggregation in solution and can be quantified with UV-Vis absorption techniques [62].
- **Solvent boiling point**: higher boiling point solvents maintain the polymer in a metastable state for a longer time during the deposition, and lead to a better alignment of the domains.

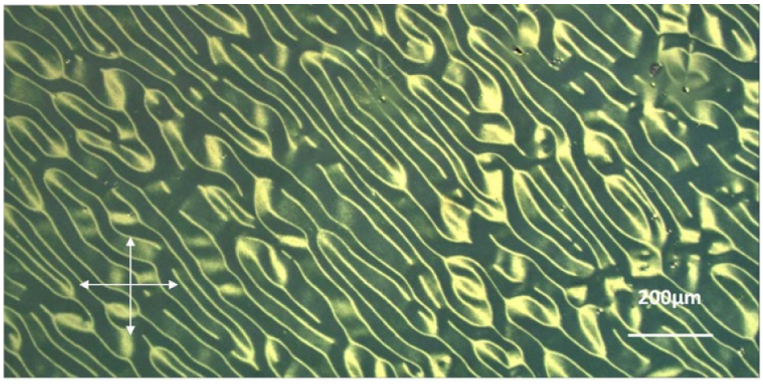

Figure 4.2: *Cross polarized optical microscopy image of N2200 deposited on glass substrate from toluene: the birifrangent domains are clearly visible, the darker areas reveal that the polymer chains are aligned along one of the two polarizes directions (represented by the two arrows), while the polymer chains aligned at 45 degrees appear as brighter areas [31].*

4.1.2 [3]Ph

Tetraphenyl butatriene, also knwon as "[3]-cumulene" or "[3]Ph", is a small-molecule OSC containing a cumulene-like carbon atomic wire (CAW) [14]. The molecule is characterized by a short carbon chain composed of three cumulated double bonds (i.e., four carbon atoms) and terminated at each end by two phenyl moieties (Fig 4.3). The cumulene-like structure in the molecule leads to a HOMO-LUMO gap of 3.2 eV [19] and results in its semiconducting behaviour. The phenyl end-groups have multiple functions: (i) they are able to isolate the carbon chain making the molecule stable up to ∼250 °C in ambient conditions [19], (ii) they induce a cumulene-like organization thus reducing the bond-length alternation (BLA) and the HOMO-LUMO gap as described in Chapter 2.2, and finally (iii) they make the molecule soluble in commercial solvents thus allowing its deposition from solution. The solubility of [3]Ph in different solvents is reported in Table 4.1. The molecule was produced by R. Tykwinski et al. [47]. The deposition from solution of [3]Ph, as for most small-molecules OSC, is characterized by a fast crystallization process. This effect causes a non-uniform coverage of the transistor, detrimental for the OFET performance [19]. In order to have a better control of the deposited film microstructure, [3]Ph can be blended with a suitable polymer. In a previous work [14], atactic polystyrene (PS) with a molecular weight of 2000000 g/mol was chosen as blending polymer. In order to increase the charge injection efficiency, a self-assemble monolayer (SAM) can be applied on the gold electrodes. Being [3]Ph a p-type OSC, a suitable SAM is pentafluorotiophenol (PFBT). PFBT lowers the gold work function (W_f) reducing the contact resistance. Anyway, the presence of the SAM strongly affects the crystallization process. Hence, while it improves the charge injection, it is still not clear if it benefits the overall performance of the transistors.

[3]Ph solubility	
Solvent	**Solubility (g/L)**
Acetone	0.8
Ethanol	0.07
Hexane	0.15
Dichloromethane	12.6
Toluene	6.07

Table 4.1: *Solubility of* [3]*Ph in different solvents [14].*

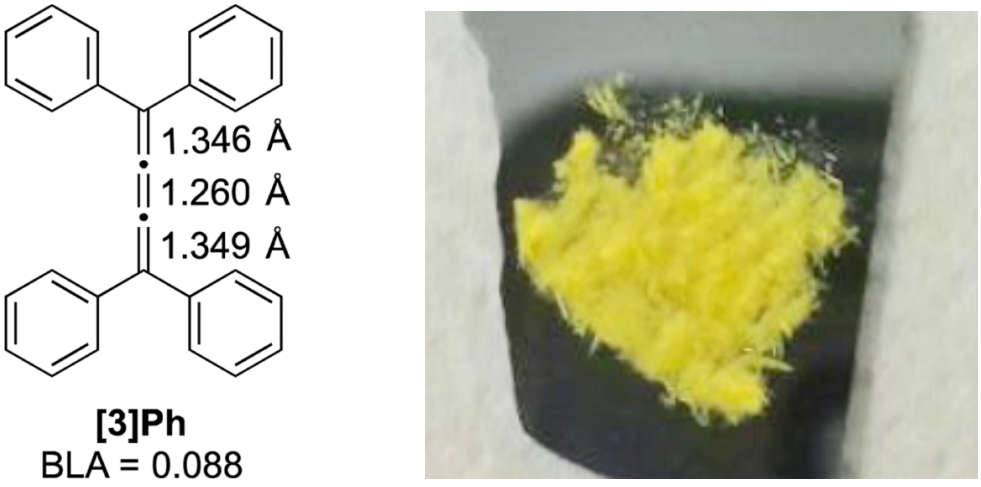

(a) *(b)*

Figure 4.3: *(a) Lewis structure and BLA of the* [3]*Ph molecule [47] and (b) the pure molecule in the solid form [14].*

4.2 Device fabrication

In this section, the procedures adopted to fabricate the devices with N2200 as active material will be described in detail. The devices fabrication was carried out following a procedure similar to previous works [31, 63]. Regarding the OFETs architecture, TGBC was chosen. Indeed, this structure helps protecting the active material from possible environmental contaminations and allows the deposition of the dielectric from solution. Being the stability of N2200 well known, the application of the dielectric via solution process allowed a cheap and fast deposition without altering the semiconductor properties. All the fabrication steps were carried out in a nitrogen glove box in order to minimize contaminations, except from the solutions preparation carried out under a chemical fume hood.

4.2.1 Contact deposition

The source and drain interdigitated electrodes where fabricated on top of Corning glass substrates using conventional photolithography. The LOR 5B underlayer and the MICROPOSIT S1813 layer were deposited exposed and developed in MF 319. The substrates with the patterned resist were brought into the "PROvap Glovebox Integrated M-braun Thermal Evaporator" without mask for the contacts evaporation and brought in high vacuum. On top of the substrates a thin layer

of chromium with a thickness of 2 nm was deposited by thermal evaporation in order to increase the adhesion of the gold contacts with the glass substrate. Over the chromium layer a gold layer with a thickness of 30 nm was deposited. Afterwards, the substrates were put in a bath of n-Methyl-2-pyrrolidone (NMP) and left overnight for the lift-off. The process is reported in Fig 4.4 while the final gold patterned substrate is reported in Fig 4.5. After the semiconductor, dielectric and gate deposition each final substrate (sample) is composed of 16 transistors with two orthogonal orientations and four different channel lengths (20, 10, 5 and 2.5 μm).

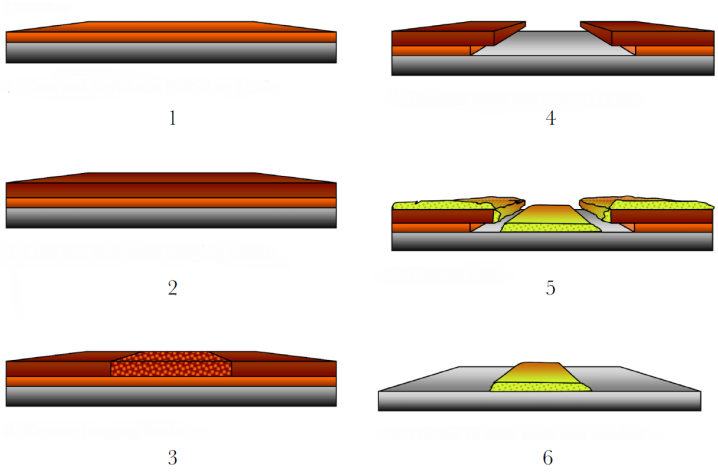

Figure 4.4: *Schematic representation of the photolithography: 1)Deposition of LOR5B, 2) deposition of MICROPOSIT S1813, 3) exposure of the photoresist to UV light, 4) development of the photoresist, 5) chromium and gold deposition, 6) lift-off.*

4.2.2 Solutions preparation

Four different solvents were used in order to dissolve N2200: toluene (Tol), mesitylene (Mes), chlorobenzene (CB) and 1-chloronaphthalene (CN), with boling points of 111 °C, 164.7 °C, 131 °C and 263 °C respectively. N2200 was weighted using a microbalance and then dissolved in the different solvents listed above, the process was performed under a chemical fume hood. Four different solutions with concentration of 15 g/L were prepared, then stirred overnight at ambient temperature in order to completely dissolve the polymer. When needed, part of the solutions was taken out and diluted in a new vial after stirring the original solution for an hour.

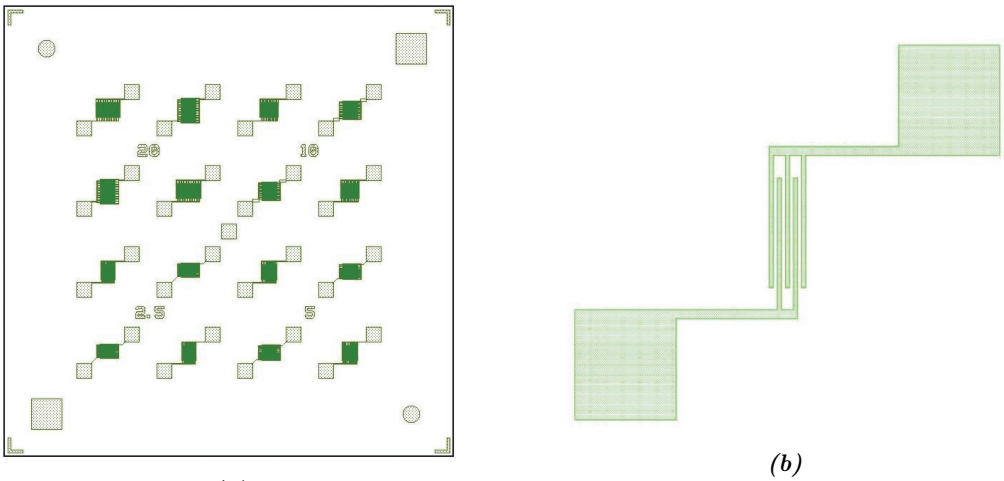

(a) *(b)*

Figure 4.5: *a) Schematic representation of the substrate composed of 16 contacts with two different orientations and four different channel lengths. b) Schematic representation of the single interdigitated electrode.*

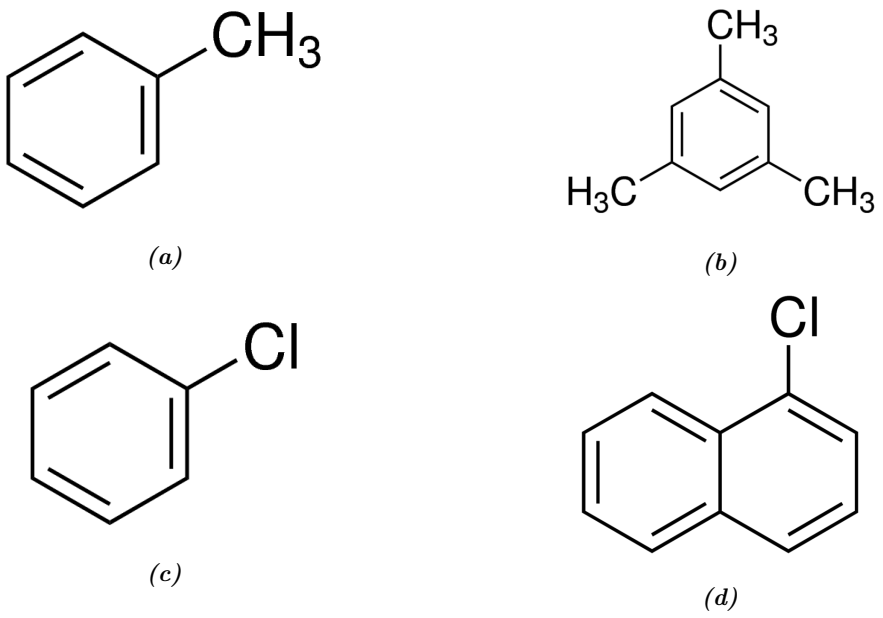

(a) *(b)* *(c)* *(d)*

Figure 4.6: *Chemical structure of the four solvent used to dissolve N2200: a) Toluene, b) Mesitylene, c) Chlorobenzene and d) 1-Chloronaphthalene.*

4.2.3 Substrate preparation

The gold-patterned substrate were carefully cleaned, just before the OSC deposition, by following a cleaning protocol. The first cleaning step was performed by ultrasonic bath in acetone (five minutes) and isopropyl alcohol (five minutes) followed by a drying step done with a nitrogen gun. This process aims at removing the impurities which may be still present from the lithography such as gold fragments or resist leftovers and all the macroscopic particles such as dust. Afterwards, the substrates were treated for five minutes with an O_2 plasma in order to "burn" any organic impurities left. A "Diener Electronic Femto Plasma asher" was used. Molecular oxygen was injected in the chamber at pressure of 0.4 $mbar$ with a flux of 0.5 $SCCM$ and the plasma with a nominal power of 100 W. The cleaned substrates were then immediately brought in the glove box for the deposition of the semiconductor.

4.2.4 Off-center spin-coating

The semiconductor deposition was performed in a nitrogen glove box by means of off-center spin-coating. This technique allows to deposit an OSC from solution and obtain a uniform layer, furthermore, during the deposition a centrifugal force is applied on the solution which lead to an alignment of the crystalline domains in the deposited film [27]. The semiconductor film thickness mainly depends on two parameters: viscosity of the solution and spin-coating-speed [64]. The film thickness decrease with decreasing viscosity and increasing spin-coating-speed. The resulting semiconductor thickness affects the transport properties. For instance, in TGBC OFETs, carriers have to be transported in bulk to reach the channel at the interface with dielectric. This causes the presence of a bulk resistance, that can not be neglected if the film is thick. On the other hand, if the film is too thin there might be a poor active material coverage, detrimental for the charge conduction. The chosen setup was composed by a microscope slide with, at one side, a double-side adhesive carbon tape over which was attached the substrate, and on the other side a counterweight. The carbon tape, and thus the substrate center, was positioned at a distance of 3 cm from the spin coating center. 70 μL of solution was deposited on the substrate prior to the beginning of the spin-coating program, carefully paying attention that the solution covers every gold electrodes.

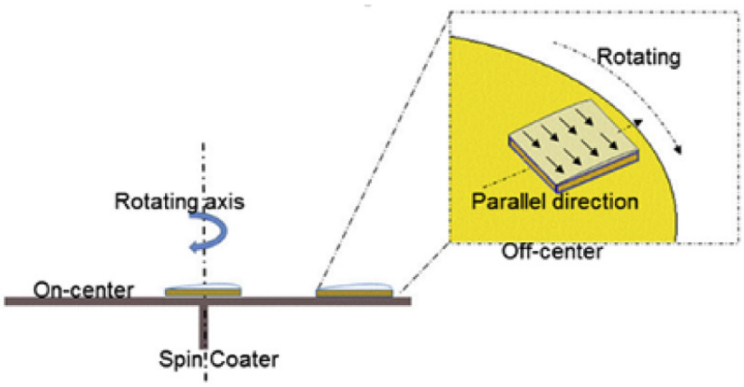

Figure 4.7: *Schematic representation of on-center and off-center spin-coating [27].*

The deposited liquid is subjected to two forces able to align the domains: a centripetal (and centrifugal) force, due to the rotational speed, which align the domains in the direction radial with respect to the spin center, and, a tangential force due to the angular acceleration which tends to align the domains in the direction tangential with respect to the spin center. The tangential force is present only in the first section of the spin coating process, indeed, the tangential force becomes null once the maximal rotation speed is reached. In order to minimize the tangential force and thus the tangential alignment of the domains, a two step spin coating program was selected: a first step characterized by a low angular acceleration and a second step during which the target speed is reached and maintained. Specifically, the first step was characterized by an angular acceleration of 50 rpm/s for 10 seconds reaching a rotation speed of 500 rpm, and the second step, lasting 60 seconds, with 2000 rpm/s acceleration until the required speed was reached.

4.2.5 Kinetically controlled crystallization

Immediately after the spin-coating process the coated substrate was put on a hot plate for the kinetically controlled crystallization (KCC) treatment. This process aims at controlling the crystallization mechanism by changing the rate at which the solvent evaporates [63]. By controlling the crystallization rate it is, in principle, possible to influence the dimension and distribution of the polymer domains. Two main factors are involved: the nucleation rate and the growth rate. The nucleation rate increases with temperature due to an activation energy for diffusion (Q_d) following an Arrhenius-like equation, but it is suppressed at high temperature due to the high energy barrier for phase transformation of the polymer from solid to

liquid (ΔG^*) given by the difference in Gibbs free energy between the solid and the liquid state. The latter energy barrier is proportional to $\frac{1}{(\Delta T)^2}$, thus it is responsible for the suppression of the nucleation rate at high temperatures. It is possible to express the nucleation rate N as:

$$N \propto exp\left(\frac{-(Q_d + \Delta G^*)}{K_b T}\right) \propto exp\left(\frac{-Q_d}{K_b T} - \frac{1}{K_b T(T - T_m)^2}\right) \tag{4.1}$$

where K_b is the Boltzmann constant and T_m is the melting point of the polymer. The growth rate, on the other hand, depends only on the diffusion energy and, thus, keeps growing with increasing temperature. It is possible to distinguish between three main regimes:

- **Low temperature KCC (∼60 °C)**: both nucleation and growth rates are low, the resulting domains are small.
- **High temperature KCC (∼150 °C)**: high nucleation and growth rate lead to a large number of nucleation points, the domains does not have space to grow.
- **Moderate temperature KCC (∼100 °C)**: sufficiently high growth rate and moderate nucleation rate give time to the polymer domains to grow, allowing optimal domain extension.

The KCC was performed between 30 °C and 150 °C until all the solvent evaporated, thus the treatment time was different for each sample and was chosen based on the deposition and solution parameters, KCC temperature, and, after visual check of the samples. The treatment time increases with increasing boiling point of the solvent, solution concentration and decreasing KCC temperature and spin-coating speed, because higher concentrations and slower spin coating speeds lead to thicker films and, thus, slower evaporation rates. Once the films were dry, an annealing at 200 °C was performed for 30 minutes. This treatment aims at completely evaporates the residual solvent and helps to slightly rearrange the polymer chains without causing drastic changes in the film morphology [60].

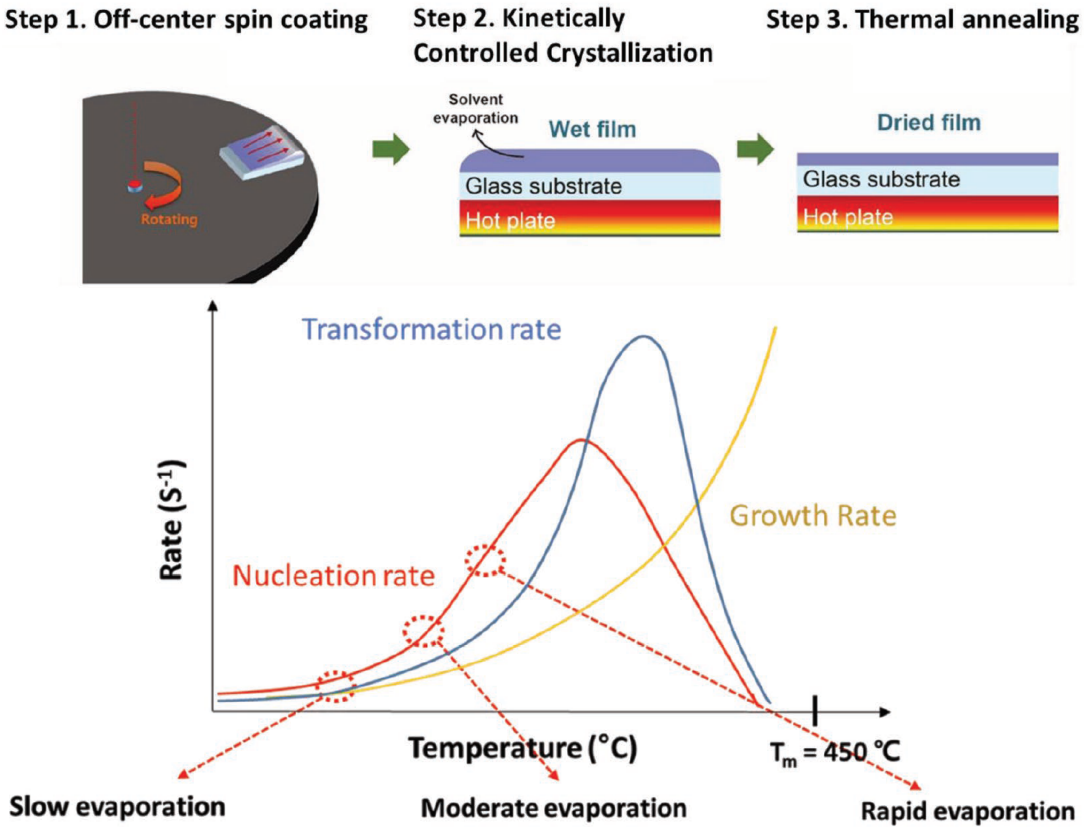

Figure 4.8: *Schematic representation of the KCC process and the expected transformation rate as a balance between nucleation and growth rate [63].*

4.2.6 Dielectric and gate deposition

Poly(methyl methacrylate) (PMMA) was chosen as dielectric material because it provides a suitable interface with N2200 for the charge transport (trap-free). In addition, by chosing a suitable solvent unable to dissolve N2200, PMMA can be deposited from solution with a cheap and fast process. PMMA with average molecular weight of 120000 g/mol purchased from Sigma-Aldrich was weighted using a microbalance and dissolved in n-butyl acetate, preparing a solution with concentration of 80 g/L. The solution was then put on a hot plate for 2 hours at 80 °C with strong stirring in order to completely dissolve the PMMA in the solvent. The solution was then brought into the glove box and let it cool down to ambient temperature. In order to obtain a uniform PMMA film, 80 μL of solution was placed on top of the substrates just before on-center spin-coating at 1300 rpm for 60

seconds with an acceleration of 1000 rpm/s. Then, the coated substrates were put on a hot plate and annealed at 80 °C for 2 hours in order to completely evaporates the solvent. This procedure allowed to obtain a PMMA film with a thickness around 500 nm, assessed by means of mechanical profilometer. After deposition of the dielectric the samples were brought into the "PROvap Glovebox Integrated M-braun Thermal Evaporator" for the aluminum gate deposition. Aluminum was chosen because it is cheap, easy to evaporate and compatible with most organic materials. Using a specific shadow mask reported in Fig 4.9, the aluminum gate with thickness of 50 nm was deposited on top of the PMMA layer yielding the final transistor (schematized in Fig 4.10).

Figure 4.9: *Picture of the mask used for the aluminum gate evaporation.*

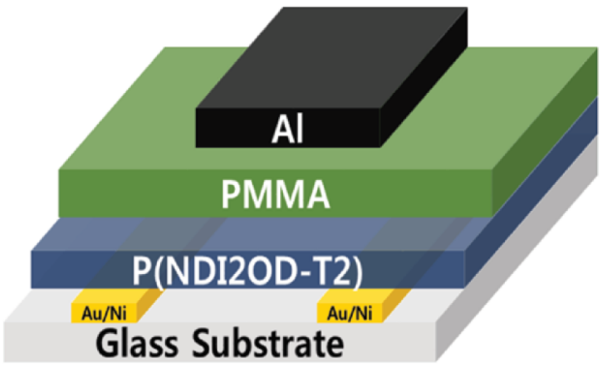

Figure 4.10: *Schematic representation of the complete OFET [63].*

4.3 Characterization

In this section the characterization techniques are reported. Starting from the characterization of the solutions, followed by the film and material characterizations and ultimately the device electrical analyses.

4.3.1 UV-Vis spectroscopy

In order to address the pre-aggregation level in solution, the most straightforward way is to use UV-Vis absorption spectroscopy. Indeed, it was demonstrated that the presence of chain aggregation leads to the appearance of an absorption peak around 710 nm and a shoulder peak around 800 nm [62]. These absorption features have an absorption wavelength mostly independent on the solution concentration while it is highly dependent on the solvent. In the case of CN, these "low energy" features are not present, instead the absorption spectrum is characterized by a broad and featureless band centered around 620 nm. This features were attributed to the fact that N2200, when dissolved into CN, does not aggregate and the absorption around 620 nm is due to intrachain excitons in the isolated chains. On the other hand, when the aggregation in solution is present, the change in conformation of the polymer upon stacking leads to a red-shift of the absorption spectra. The two different features at 710 and 800 nm were attributed to two different aggregation states, called "aggregate I" and "aggregate II". Finally the "high energy" peak present around 400 nm is related to the $\pi - \pi^*$ transition and it is slightly influenced by the aggregation state. The UV-vis Absorption spectra were obtain by measuring transmission spectra on a "PerkinElmer Lambda 1050 UV/Vis/NIR" spectrometer.

4.3.2 Optical polarized microscopy

The supramolecular structure transferred from the pre-aggregation in solution to the deposited film can be addressed by means of polarized light microscopy (PLM) [31]. In this technique, polarized light is shined on the substrate, then the reflected or transmitted light is observed through another polarizing filter, by rotating the second filter it is possible to operate in different regimes. In particular when the second polarizing filter is oriented at 90° with respect to the first, the technique is called "cross polarized optical microscopy" and only the light that is being rotated in polarization by the sample will be observable. When a birefringent material is observed, the polarized beam is splitted into two different beams with different

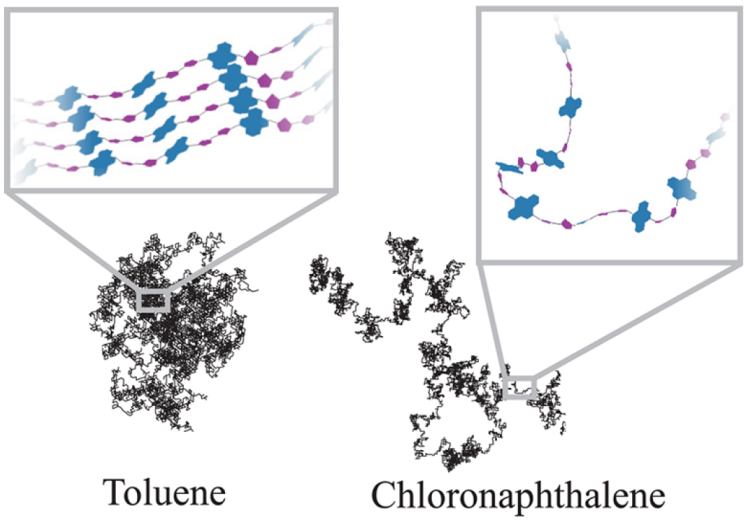

Figure 4.11: *Schematic representation of the aggregation state of N2200 in toluene and chloronaphtalene [62].*

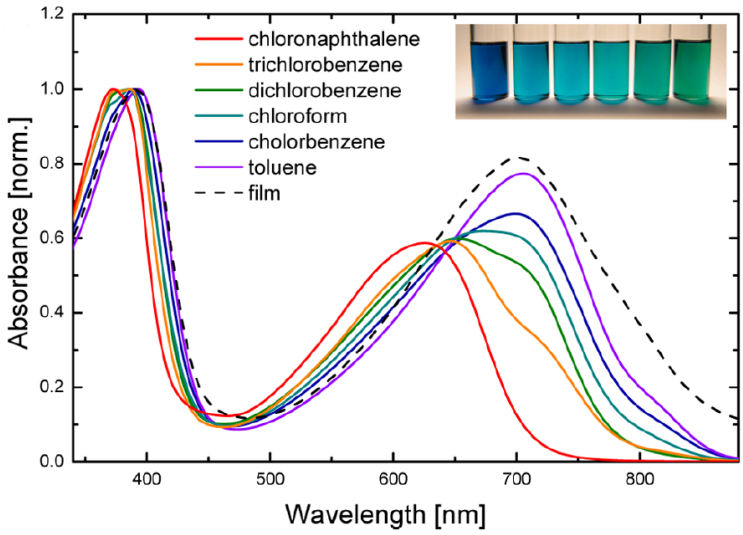

Figure 4.12: *UV-Vis absorption spectra of N2200 dissolved in different solvents (concentration of 1 g/L), and in the film form. The spectra were normalized at their maximum [62].*

phases and polarizations, thus making the sample observable. Using the latter approach, it is possible to exploit the birefringence in the deposited N2200 film in order to distinguish the domains. Indeed, the darker areas in the film can be addressed as zones in which the polymer is oriented along one of the two polarized directions, the brighter areas, instead, are observed when the polymer is oriented at

45°. PLM is therefore able to distinguish the orientation of the polymer chains and thus makes the observation of the domains possible. The cross polarized optical microscopy analyses were carried out using a "Zeiss Axioscope A1" microscope both in reflection and transmission mode and captured using a camera directly mounted on the microscope.

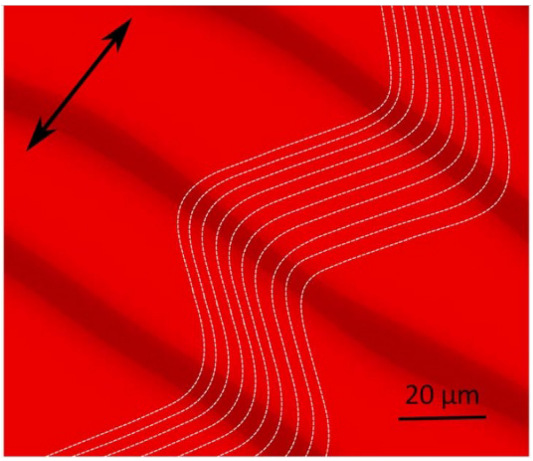

Figure 4.13: *Optical polarized microscopy image of a N2200 film deposited from toluene, the domains are clearly visible. A sketch of the polymer chain orientation, based on of AFM measurements, is reported [31].*

4.3.3 Mechanical profilometer

The evaluation of the film thickness was carried out using a mechanical profilometer, in particular the instrument was a "Alpha-Step IQ surface profilometer" in contact mode. In order to characterize the dielectric thickness, during each dielectric deposition a PMMA film was deposited on a microscope slide, previous cutting followed by the cleaning processes described in Section 4.2.3. The deposited film was then carefully scratched with a pair metal tweezers. By measuring in the direction perpendicular to the scratch, and comparing the height measured on the scratch with the one of the film, it was possible to address the film thickness.

4.3.4 Semiconductor parameter analyzer

The electrical measurements were performed using a semiconductor parameter analyzer (SPA) "Agilent Technologies B1500A Semiconductor Device Analyzer" with a current resolution of 0.1 fA, placed into a nitrogen glove box. With the use of this instrument it was possible to obtain the "transfer curves" and the

"output characteristics" of the devices. Prior to the measurement, the devices were annealed at 120 °C overnight in order to remove any moisture and oxygen residues, then were placed under the microscope and contacted with the instrument. The device characteristics were obtained with a sweep in the gate voltage from -10 V to 40 V and back, while the source was at ground voltage and the drain voltage at 10 V and 40 V for linear and saturation regimes respectively. Only the devices with channel lengths of 20, 10 and 5 μm were measured in order to not take into account "short channel effects" and thus obtain more reliable results. The SPA measures three currents as a function of the gate voltage: the source current, the drain current and the gate current also known as "leakage current". The leakage current comes from the charges that are able to penetrate the dielectric. Of course, this effect is non-ideal and is a source of noise in the measure, for this reason it should be minimized. In saturation regime the leakage current usually has a minor influence because the potential between source and drain is greater than the potential between the gate and the other contacts. For this reason the extraction of the mobility in the saturation regime is usually more reliable and was chosen as the quantity to be optimized in this work. An example of the obtained transfer curve is reported in Fig 4.15.

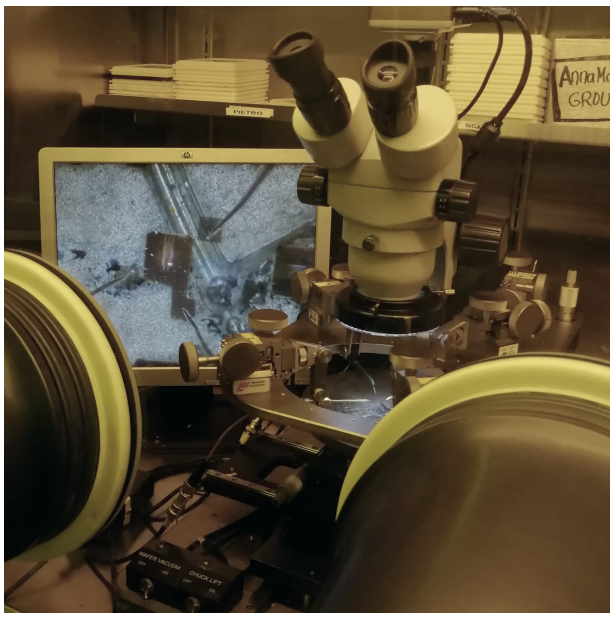

Figure 4.14: *Picture of the SPA setup.*

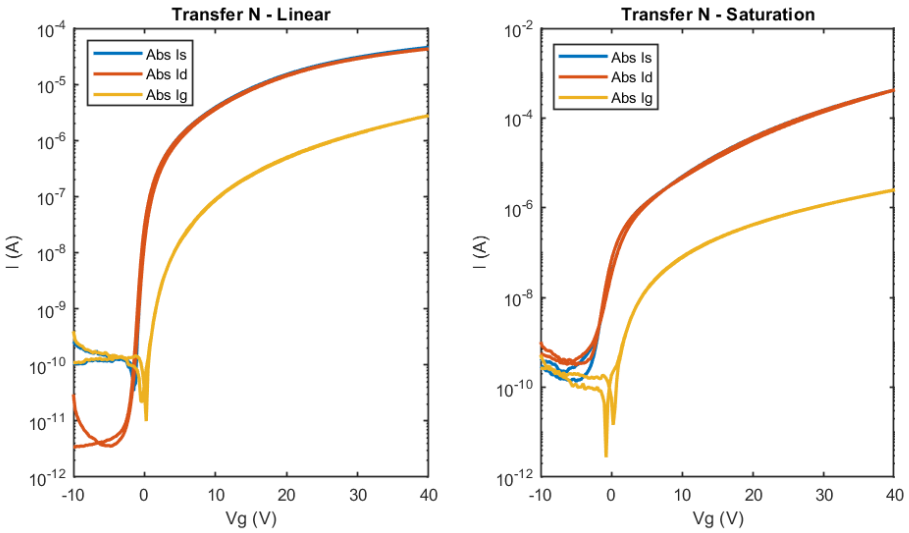

Figure 4.15: *Example of the transfer curve obtained in linear and saturation regime.*

4.3.5 Parameters extraction

The aim of this work was to optimize the mobility of the semiconductor, in particular in the saturation regime. For this reason, even though it is possible to extract many device parameters from the transfer curves, the focus of this section will be put on the mobility extraction.

Starting from the transfer curves the mobilities in the two different regimes can be calculated as:

$$\mu_{lin} = \frac{L}{WC'_{diel}V_{ds}} \frac{\partial I_{ds,lin}}{\partial V_{gs}} \tag{4.2}$$

$$\mu_{sat} = \frac{2L}{WC'_{diel}} \frac{\partial \sqrt{I_{ds,sat}}}{\partial V_{gs}} \tag{4.3}$$

where W and L are the channel width and length, C'_{diel} is the capacitance per unit area of the dielectric, V_{ds} and I_{ds} are the voltage and the current between source and drain and V_{gs} is the gate voltage. It has to be noted that the mobility extracted from Eq 4.2 and 4.3 does not correspond to the intrinsic mobility of the semiconductor because it is influenced by the non-idealities that may be present in the device such as contact resistance and short channel effects. The obtained transfer curves were analyzed by using a Matlab script written by S. Pecorario.

In order to obtain a more reliable extraction of the mobility, the derivatives present in Eq 4.2 and 4.3 were calculated by fitting the $I-V$ curve, in the forward sweep, between 20 V and 30 V with a straight line. By calculating the slope of the fitted line, it was possible to estimate the derivative in that region in a precise way. The graphical representation of the method is reported in Fig 4.16. With this method, the extracted saturation mobility is similar to the linear one, and, in general, is understimated. The correct procedure for the extraction of the mobility is still under debate [65]. For instance, in N2200, the mobilities extracted in saturation regime increase with increasing gate voltage [31]. However, the values extracted at high potentials are less reliable because the non-ideal effects, discussed in Chapter 1.5, can have a big influence. The goal of this work was to have reliable data to train the machine learning algorithm. For this reason, only the best devices were then measured again with the SPA in an extended range of gate potential in order to make a comparison with the mobility values extracted in the reference work at 60 V [63]. The saturation regime was characterized by a drain voltage of 60V and the gate sweep was between -10 V and 60 V, the mobility was then extracted between 55 V and 58 V.

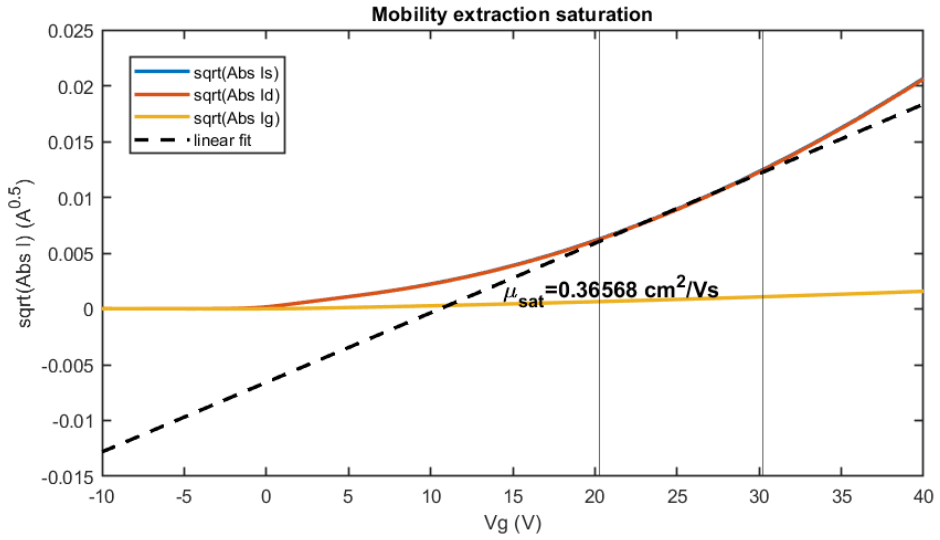

Figure 4.16: *Example of the mobility extraction method adopted in the case of saturation regime.*

4.4 Optimization

The optimization process was carried out in two stages:

- **Validation with N2200 OFETs**: the effectiveness of BO and SVR optimization was validated and compared in the case of N2200 OFETs. The optimization started from design of experiments (DoE) common to the two methods in order to have a reliable comparison. All the data used were obtained during the optimization process.
- **Prediction of [3]Ph OFETs**: the methods validated during the N2200 OFETs optimization were used on an existing dataset in order to make predictions and guide future experiments in the optimization of [3]Ph OFETs.

4.4.1 Software

The scripts for the optimization algorithms were written using Python 3 [13]. For the SVR optimization it was adapted from a script written by B. Cao et al. [3] using Scikit-learn package [66], while the BO script was written using the "GPyOpt" open-source library [12].

Chapter 5

Results

5.1 Validation of the models with N2200 OFET

As already introduced, the work started with the validation of the two machine learning models via the optimization of the saturation mobility of N2200 organic field-effect transistors (OFETs). The optimization process started with the selection of the input variables, followed by the design of experiments (DoE) of the first round of experiments, common to the two optimization methods. After the first round of experiments, the two optimization methods were carried out independently from each other in order to obtain a genuine comparison.

5.1.1 Variables selection

Based on existing literature, four different fabrication parameters were chosen as input variables [31, 63, 61]: solvent type, solution concentration, spin-coating speed and kinetically controlled crystallization (KCC) temperature. The range selection of each variable was based on the reference papers as well, although wider ranges were chosen in order to increase the exploration possibilities. The variables and the related ranges and levels are reported in Table 5.1.

5.1.2 Design of experiments and first round of experiments

The DoE was performed using a package present in GPyOpt [12]. The initial design chosen was a "space filling" design with 15 experiments. By specifying the parameters range and the number of experiments GPyOpt returns the experimental design. The first round of experiments is listed in Table 5.2. A scatter matrix is shown in Fig 5.1 to better visualise the DoE.

Parameters space Round 1			
Variable	**Levels**	**Range**	**Spacing**
Solvent	4	Tol, CN, Mes, CB	/
Solution conc.	15	1 g/L to 15 g/L	1 g/L
KCC temperature	13	30 °C to 150 °C	10 °C
Spin-coating speed	26	500 rpm to 3000 rpm	100 rmp

Table 5.1: *Table reporting the parameters and the related range selected for the first round of experiments.*

A scatter matrix, sometimes called "pairs plot", compactly represents all the numeric variables in a dataset against each other one. The diagonal cells report the histograms of the distribution of the data for each variable (how many experiments are present at that specific level) while the other cells report the scatter plots (i.e. correlation plot) of each variable combination. This visualization is useful in understanding if the DoE is able to fill the parameters space efficiently.

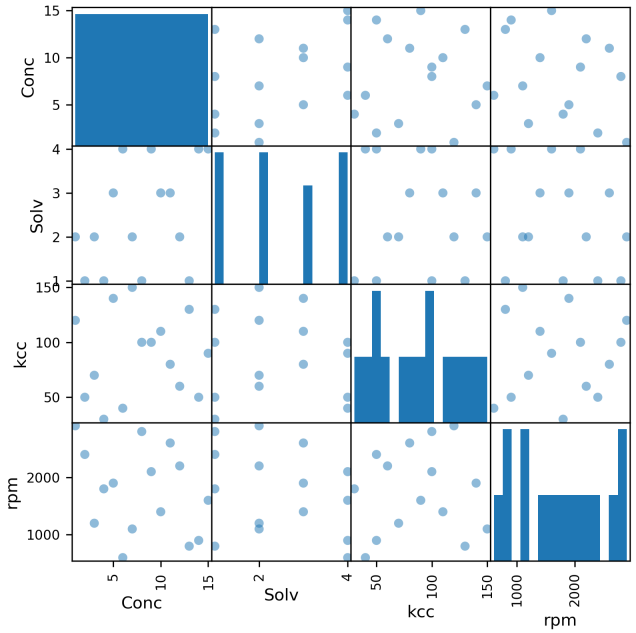

Figure 5.1: *Scatter matrix representing the DoE for the first round of experiments. The solvents are reported as numbers from 1 to 4 (1=Tol, 2=CN, 3=Mes and 4= CB).*

Round 1				
Sample	**Conc.** (g/L)	**Solv.**	**KCC** (°C)	***rpm***
0	6	CB	40	600
1	4	Tol	30	1800
2	8	Tol	100	2800
3	5	Mes	140	1900
4	14	CB	50	900
5	3	CN	70	1200
6	1	CN	120	2900
7	7	CN	150	1100
8	15	CB	90	1600
9	13	Tol	130	800
10	2	Tol	50	2400
11	12	CN	60	2200
12	10	Mes	110	1400
13	11	Mes	80	2600
14	9	CB	100	2100

Table 5.2: *Table reporting the experiments performed in the first round.*

Fifteen different substrates (samples) were then fabricated following the procedure described in Chapter 4.2 with the parameters taken from the DoE. The substrate were then brought into the glove box, annealed overnight at 120 °C and then measured with the semiconductor parameter analyzer (SPA) as described in Section 4.3.4. Each substrate contained 16 OFETs, although the transistors with channel length 2.5 μm were not measured in order to avoid short channel effects in the optimization, resulting in 12 devices for each fabricated substrate. The transfer curves obtained were then analysed in order to extract the mobility of each transistor as described in Section 4.3.5.

5.1.3 Data analysis

After the mobility extraction, only the saturation mobilities of the **aligned** devices (i.e. with polymer domains parallel to the conduction direction) were considered for the optimization. The "outliers", reported in the boxplots as white dots, were not discarded. In Fig 5.2 is reported the outcome of the first round of experiments.

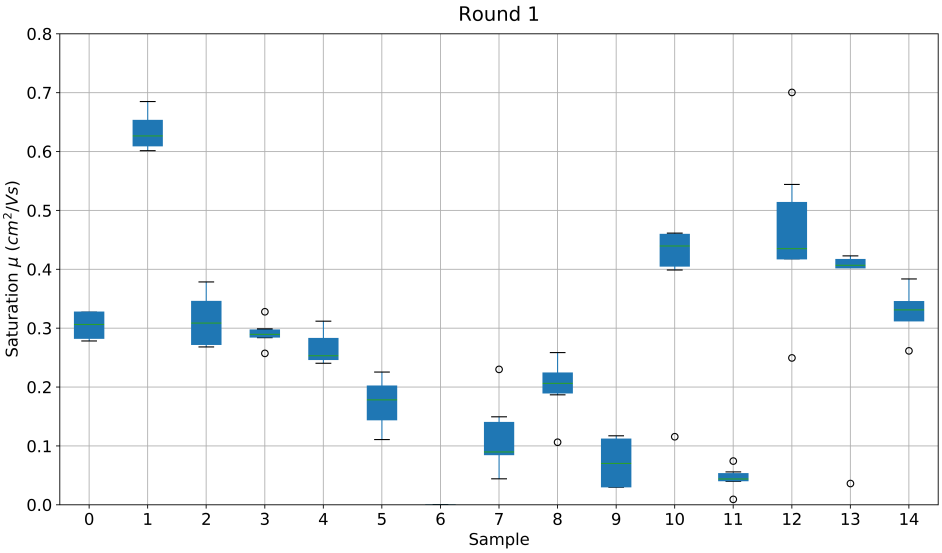

Figure 5.2: *Boxplot reporting the saturation mobility values for the first round of experiments.*

In order to improve the fitting performance of the two machine learning methods, the "solvent" variable was transformed from a categorical to a discrete variable. Categorical variables have the advantage of considering all the variable properties, in this case every solvent characteristic. However, regression methods are not able to fit categorical variables in an efficient way. The resulting fitting is comprised by a different regression for each level of the categorical variable. This approach is more general, although it requires a much larger number of experiments in order to have the same predicting ability. On the other hand, by transforming the categorical variable into a discrete variable, only some variable properties will be considered. However, the regression will be able to fit all the data with a single function, reducing the number of experiments.
During this process, the properties of the categorical variable are "encoded" into a number, which is then orderable on a one-dimensional axis. If two data points are close to each other in the parameters space, they will have a similar fitting, as discussed in Section 3.2.2. For this reason, it is extremely important to encode the variable according to a physical description. Indeed, the aim is to identify the features of a categorical variable (the solvent, in this case) that have an impact on the target property. In this way it is possible to improve the "quality" of the training set, thus the fitting performance and finally the predictive power of the

model. However, one should be aware that this discretization procedure of a categorical variable introduces a bias in the model. For this reason it is important to rely on a solid understanding of the physical phenomena underlying the impact of the categorical variable. As discussed in Section 4.1.1, the two most important factors influencing the formation of extended domains in the deposited film are: (i) the aggregate content of the polymer in solution and (ii) the solvent boiling point. The first property was quantified by analysing the UV-Vis absorption spectra in solution, while the solvents boiling points were taken from literature.

Solid N2200 was dissolved in the four different solvents, obtaining solutions of toluene (Tol), 1-chloronaphthalene (CN) and chlorobenzene (CB) with concentration 0.1 g/L and a solution of mesitylene (Mes) with concentration 0.2 g/L. The solutions were stirred for 2 hours in order to completely dissolve the polymer, then the solutions were transferred into quartz cuvettes and measured with the UV-Vis spectrometer. The obtained spectra are reported in Fig 5.3.

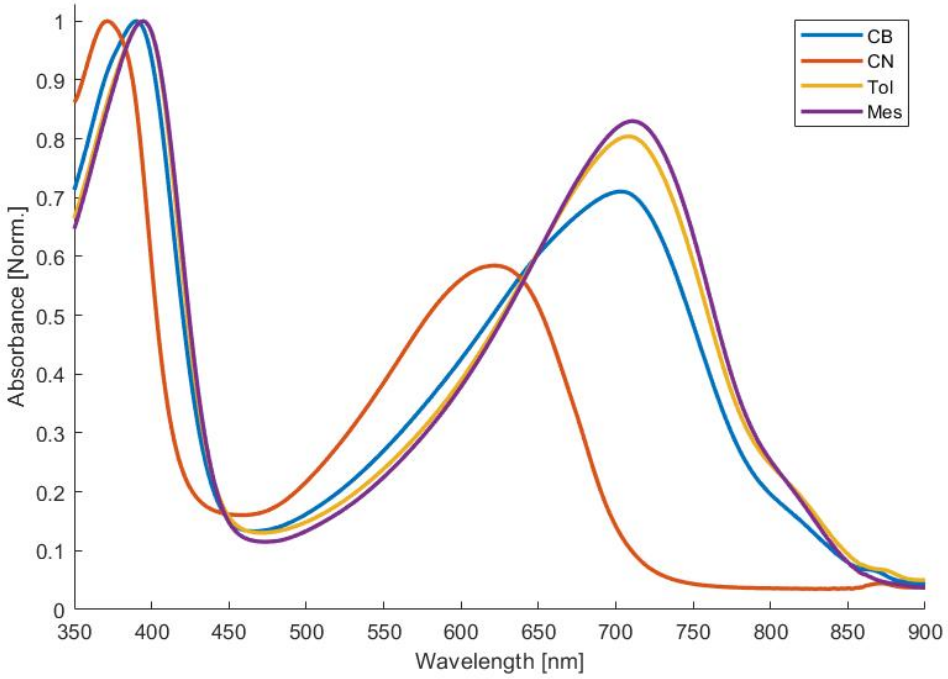

Figure 5.3: *UV-Vis absorption spectra of N2200 dissolved into the four different solvents. The spectra were normalized at their maximum.*

To address the aggregation content in solution, the spectra were normalized at 550 nm and integrated between 500 nm and 900 nm (Fig 5.4). Knowing that CN presents no aggregates in solution and knowing the ratio of the "oscillator strength" of the chains in the aggregate and non aggregate state ($\epsilon_{aggr.}/\epsilon_{amorph.} \approx 2.5$) [62], it is possible to calculate the aggregate content as:

$$Agg(x) = \frac{\epsilon_{amorph.}}{\epsilon_{aggr.}} \cdot \frac{AS(x) - AS(CN)}{AS(CN)} \tag{5.1}$$

where x is the solvent and $AS(x)$ is its integrated absorption spectrum. The calculated aggregation contents are reported in Table 5.3.

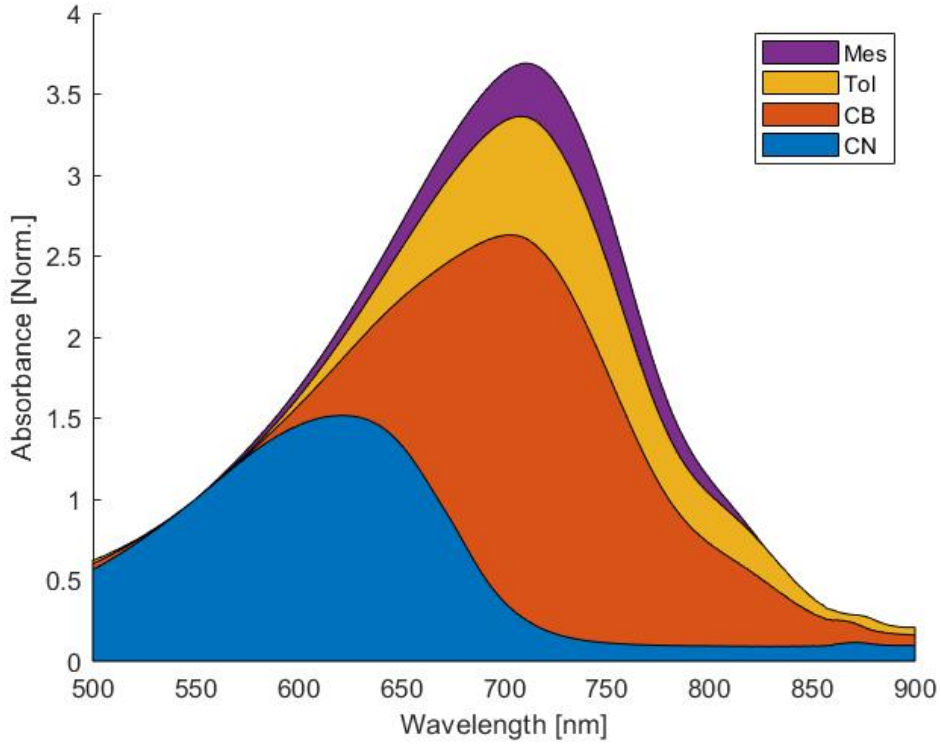

Figure 5.4: *Integrated UV-Vis absorption spectra, normalized at 550nm, of N2200 dissolved into the four different solvents.*

Aggregate content in solution				
	Tol	**CN**	**Mes**	**CB**
Calculated aggregate %	66	0	74	48

Table 5.3: *Table reporting the calculated aggregate content in the four different solvents.*

In order to encode the "solvent" categorical variable into a numerical one, considering the solvent properties listed above, the following function was implemented:

$$f(x) = a \cdot (norm(Agg(x))) + b \cdot (norm(BP(x))) \tag{5.2}$$

where x is the solvent, "Agg" is the aggregate content and "BP" is the boiling point, a and b are arbitrary weights and $norm()$ indicates a normalization function defined as:

$$norm(z) = \left(\frac{z(x) - min(z)}{max(z) - min(z)} \right) \tag{5.3}$$

where $z(x)$ is one of the solvent properties ($Agg(x)$ or $BP(x)$). The function in Eq. 5.2 returns a number between 0 and 1 (if $a + b = 1$) rating the **predicted** solvent ability to deposit high-mobility films. Based on the importance of each factor [61], the arbitrary weights were chosen as $a = 0.9$, $b = 0.1$. Proceeding in this way, it was possible to exploit the existing knowledge on the physics of the system in order to transform the "solvent" variable from categorical to discrete. The solvent properties and the calculated ratings are reported in Table 5.4.

	Agg.	**B. point**	***f***
Tol	0.66	111	0.8
CN	0	164.7	0.1
Mes	0.74	131	0.94
CB	0.48	263	0.6

Table 5.4: *Table reporting the solvent variable encoding.*

It is important to note that there is no need for an extreme precision in the value attributed to the categorical level. The objective is to encode a categorical variable into a discrete one in order to assign an order to the data to be fitted. The assigned value will determine "how close" two data points will be during the fitting. Hence, it is important to assign a physically correct **order** and not a precise numerical **value**, although the latter may influence the convergence speed of the optimisation process.

5.1.4 Support vector regression optimization

The support vector regression (SVR) optimization started with the tuning of the model hyperparameters with the data obtained from the first round of experiments. It is important to chose the correct combination of hyperparameters in order to minimize the prediction error while avoiding overfitting. In order to do so, the training and cross-validation error (loss) were plotted as a function of the three model hyperparameters (γ, C and ϵ), using leave-one-out cross-validation. The error was evaluated as a mean squared error. The hyperparameter values that minimize the error were chosen in order to avoid underfitting and overfitting, as described in Section 3.2.3. The plots used for the selection of γ and C are reported in Fig 5.5 while the selected hyperparameters are reported in Table 5.5.

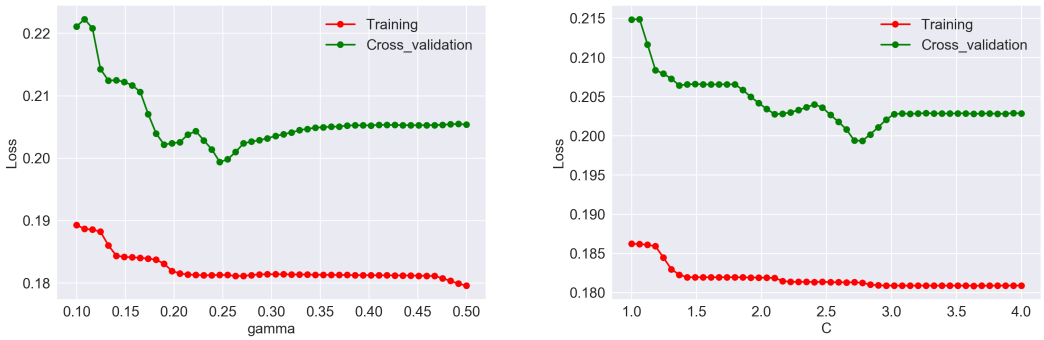

(a) ***(b)***

Figure 5.5: *SVR hyperparameter tuning for the first round: (a) training and cross-validation loss versus γ (b) training and cross-validation loss versus C.*

Round 1 hyperparameters		
γ	C	ϵ
0.25	2.75	0.01

Table 5.5: *Hyperparameters selected for the first round of SVR optimization.*

After the selection of the hyperparameters, the model was trained with the data. In order to check the fitting efficiency, the mobilities predicted for each sample by the model were plotted against the actual measured mobilities. Ideally, the plotted points should all lay on the dashed line (predicted value equal to the real value). This is obviously not the case, since an intrinsic error is present in the measurement and, even for the same sample, a distribution of mobilities is present. In any case, the graph reported in Fig 5.6 show that the fitting was successful and the points are distributed sufficiently close to the dashed line.

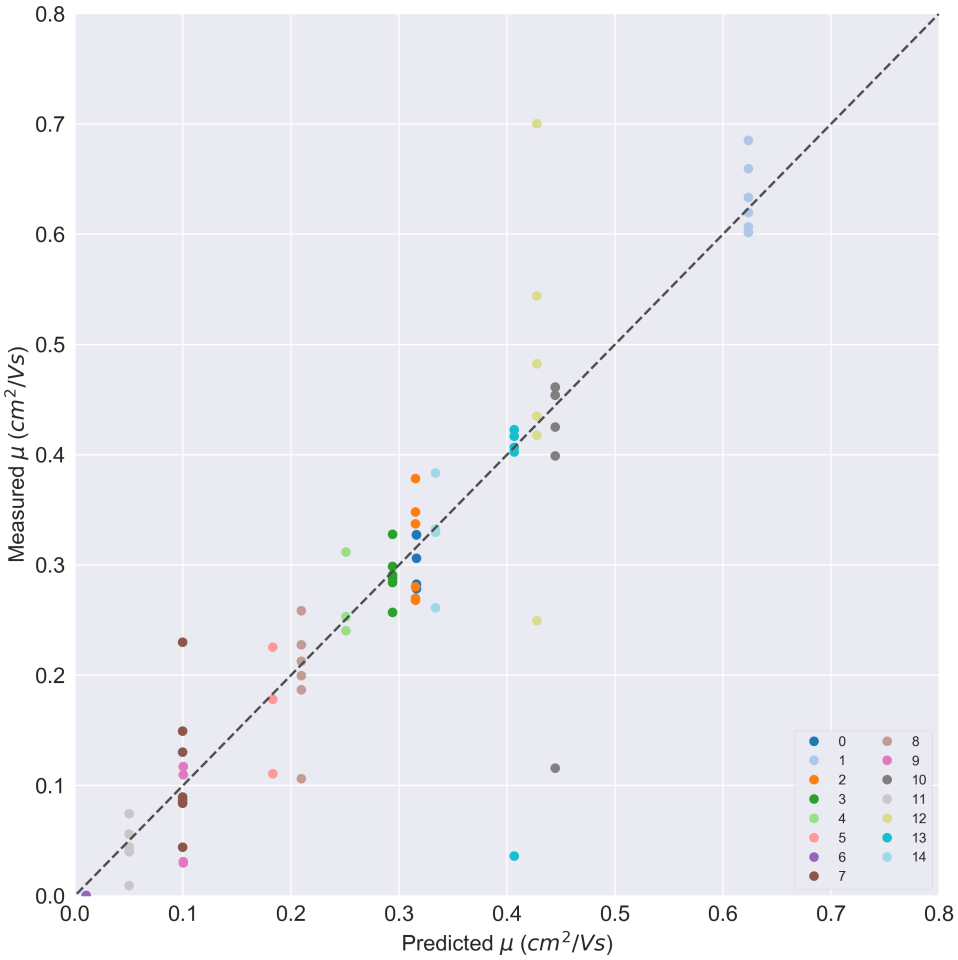

Figure 5.6: *Measured versus predicted mobility from the SVR of the first round of experiments.*

In order to visualize the function fitted by the SVR method, the five-dimensional function was "sliced" and plotted as contour plots reporting the predicted mobility as the contour. The plots in Fig 5.7, 5.8, 5.9 and 5.10 report the complete parameters space with the experimental points of the first round.

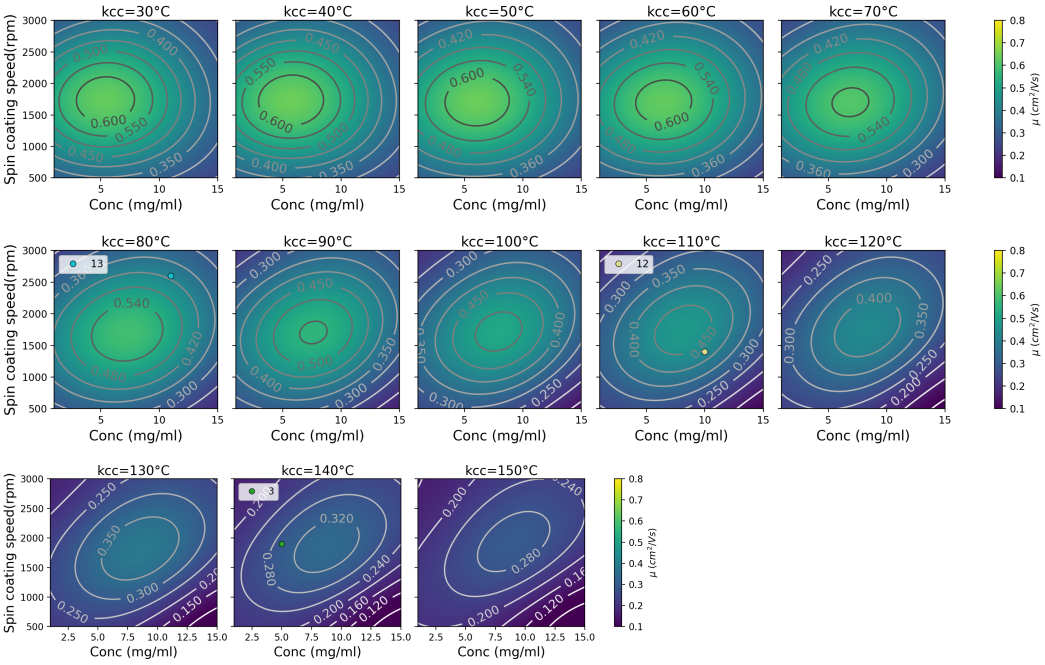

Figure 5.7: *SVR contour plots of the first round of experiments for mesitylene.*

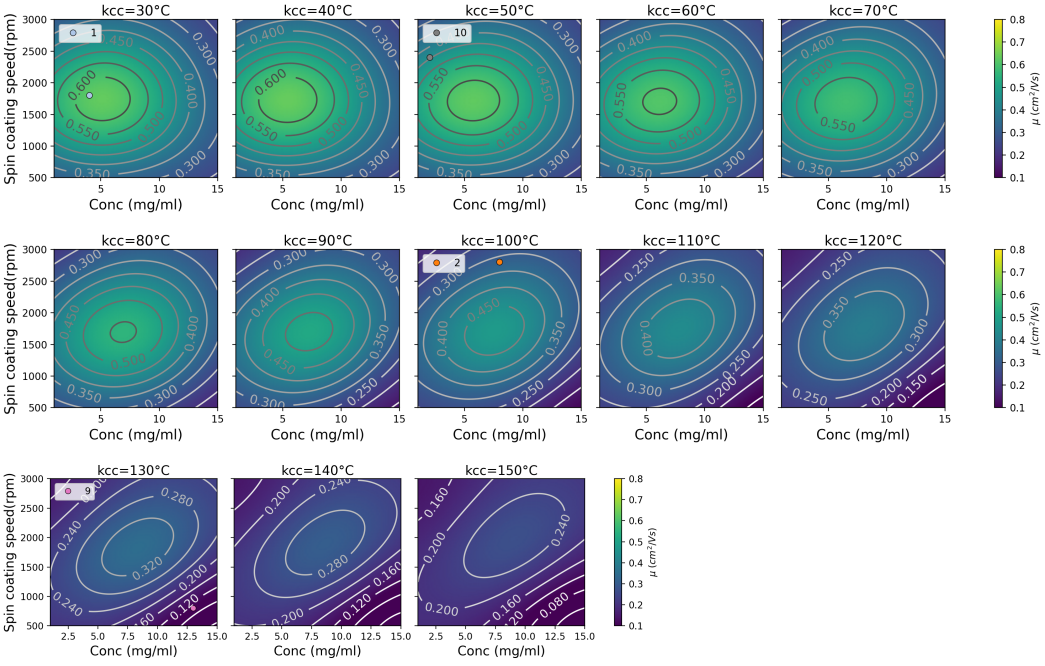

Figure 5.8: *SVR contour plots of the first round of experiments for toluene.*

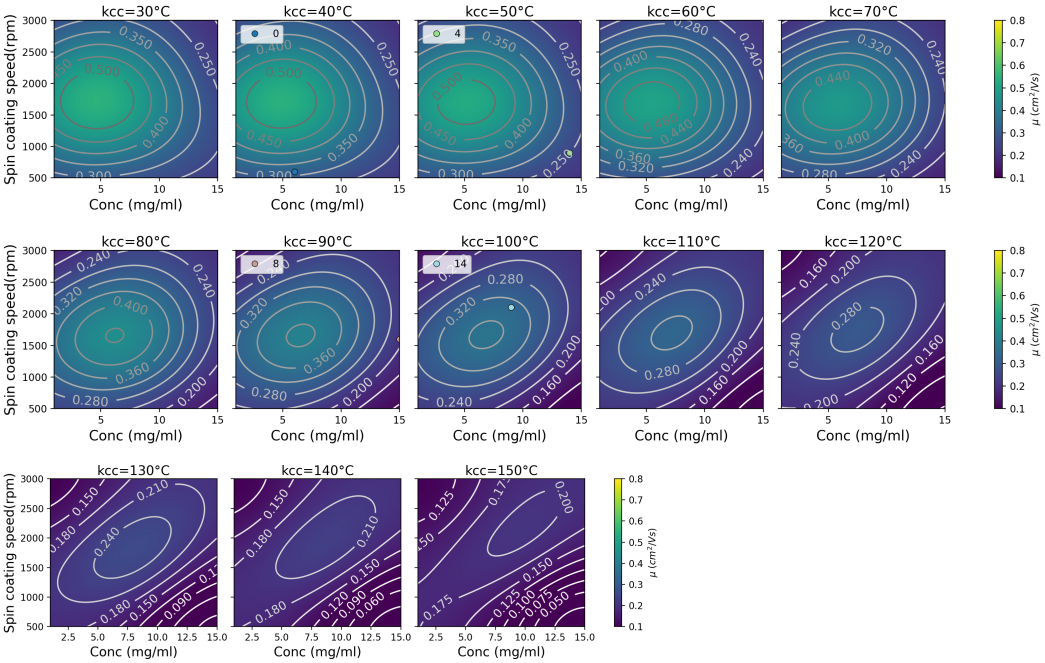

Figure 5.9: *SVR contour plots of the first round of experiments for chlorobenzene.*

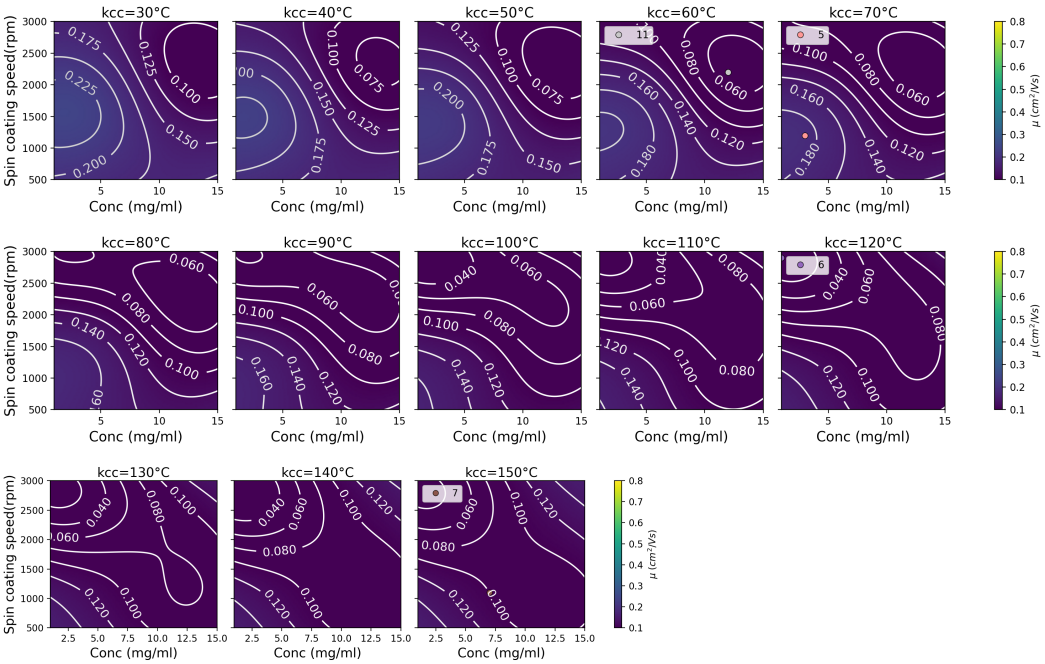

Figure 5.10: *SVR contour plots of the first round of experiments for chloronaphthalene.*

Based on the results of the SVR fitting, it was possible to narrow the parameter ranges and focus the experiments on the area where a higher mobility was predicted. The ranges chosen for the second round of SVR optimization are reported in Table 5.6.

Parameters space DoE Round 2 SVR			
Variable	**Levels**	**Range**	**Spacing**
Solvent	2	Tol, Mes	/
Solution conc.	8	4 g/L to 11 g/L	1 g/L
KCC temperature	5	30 °C to 70 °C	10 °C
Spin-coating speed	11	1200 rpm to 2200 rpm	100 rmp

Table 5.6: *Table reporting the parameters and the related range selected for the second DoE for SVR optimization.*

The second round of experiments was carried out, equivalently to the first round, following the procedure already described. The second round was however composed by only five samples. The experiments were chosen based on a new DoE performed with the new parameters ranges and are reported in Table 5.7. The samples were then measured with the SPA in order to extract the mobility values. The outcome is reported in Fig 5.11.

Round 2 SVR				
Sample	**Conc.** (g/L)	**Solv.**	**KCC** (°C)	***rpm***
15	10	Mes	30	1500
16	5	Tol	50	1700
17	6	Mes	70	1900
18	8	Tol	60	1300
19	9	Tol	40	2100

Table 5.7: *Table reporting the experiments performed in the second round guided by SVR.*

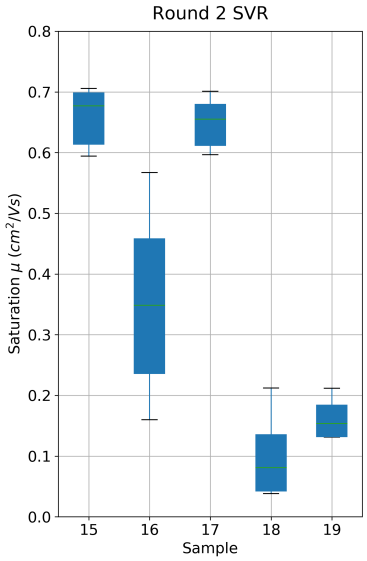

Figure 5.11: *Boxplot reporting the saturation mobility values for the second round of experiments guided by SVR.*

The dataset of the second round was added to the first one and the model hyperparameters were slightly adjusted using the same procedure described above, the updated hyperparamteres are reported in Table 5.8.

Round 2 hyperparameters		
γ	C	ϵ
0.28	15	0.01

Table 5.8: *Hyperparameters selected for the second round of SVR optimization.*

The prediction efficiency was again checked with the graph reported in Fig 5.12. The obtained contour plots, showing the "interesting" updated region are reported in Fig 5.13 and 5.14.

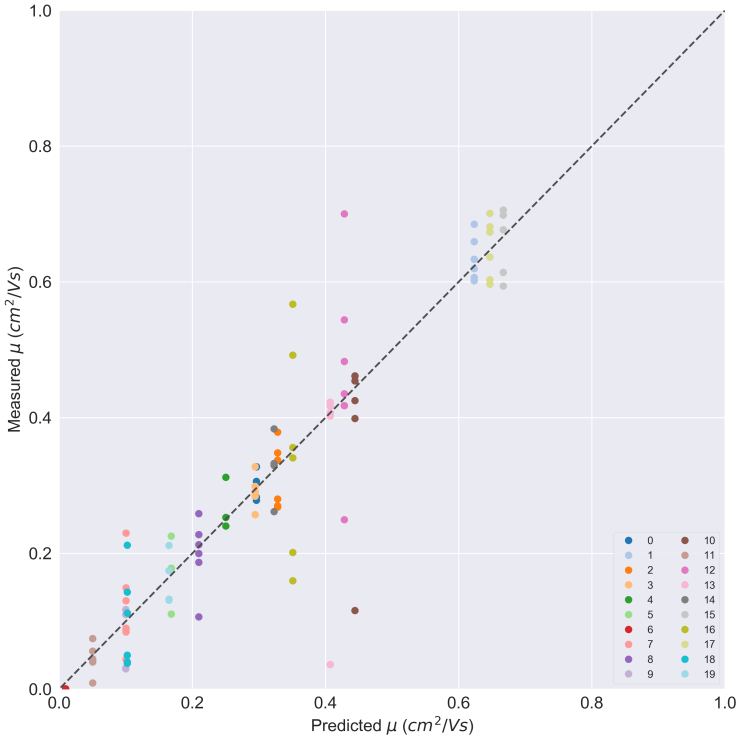

Figure 5.12: *Measured versus predicted mobility from the SVR of the second round of experiments.*

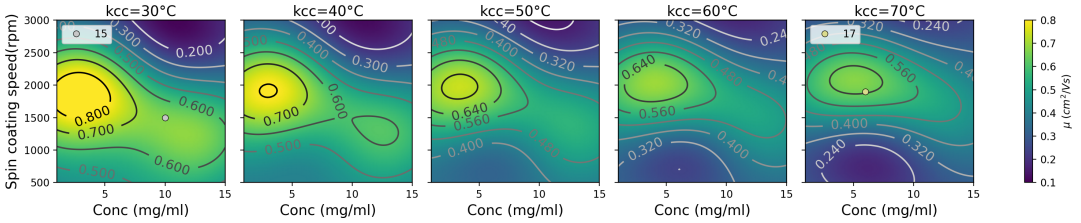

Figure 5.13: *SVR contour plots of the second round of experiments for mesitylene.*

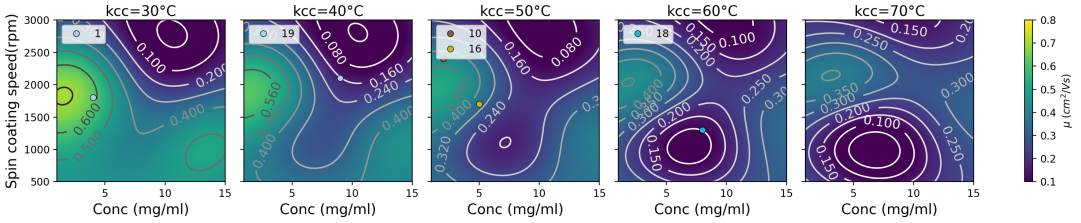

Figure 5.14: *SVR contour plots of the second round of experiments for toluene.*

For the third and last round the parameters range was narrowed again. This time, the "solvent" variable was not considered because the sample deposited from mesitylene clearly showed the best performances. The chosen range is reported in Table 5.9. This time, having only 5 levels for each variables, it was possible to have a proper "latin hypercube" design in which each level is tested one and only one time. The resulting design is schematized in the scatter matrix in Fig 5.15, the experiments are reported in Table 5.10 and the outcome in Fig. 5.16.

Parameters space DoE Round 2 SVR			
Variable	**Levels**	**Range**	**Spacing**
Solvent	1	Mes	/
Solution conc.	5	$6g/L$ to $10g/L$	$1g/L$
KCC temperature	5	30 °C to 70 °C	10 °C
Spin-coating speed	5	$1600rpm$ to $2000rpm$	$100rmp$

Table 5.9: *Table reporting the parameters and the related range selected for the third DoE for SVR optimization.*

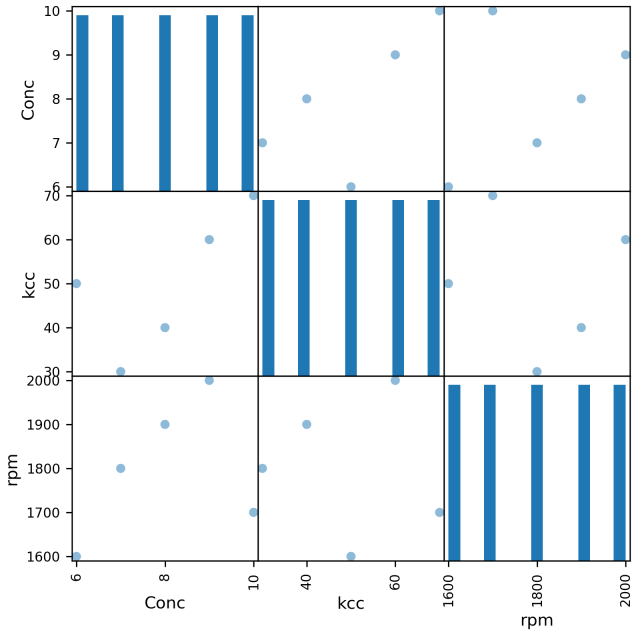

Figure 5.15: *Scatter matrix representing the DoE for the third round of SVR optimization.*

Round 3 SVR				
Sample	**Conc.** (g/L)	**Solv.**	**KCC** (°C)	***rpm***
25	9	Mes	60	2000
26	10	Mes	70	1700
27	8	Mes	40	1900
28	6	Mes	50	1600
29	7	Mes	30	1800

Table 5.10: *Table reporting the experiments performed in the third round guided by SVR.*

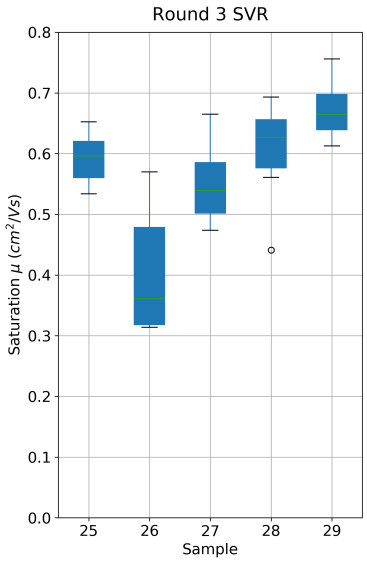

Figure 5.16: *Boxplot reporting the saturation mobility values for the third round of experiments guided by SVR.*

It is possible to conclude that SVR optimization led to an overall increase of the performances of the samples. In the last round, the effectiveness of the optimization is clearly visible. Indeed, the worst device showed a saturation mobility over 0.3 cm^2/Vs and the best one, with a saturation mobility of 0.756 cm^2/Vs, was the best device of the entire SVR optimization.

5.1.5 Bayesian optimization

Bayesian optimization (BO) was performed in parallel with the SVR optimization, starting as well from the first round of experiments and with the "solvent" variable transformed to discrete variable. With this approach, the data are fitted with a Gaussian process (GP), then with the use of an acquisition function, the algorithm is able to return the suggested experiments for the following round. The parameters space chosen for the optimization was the same as the one used for the DoE of the first round of experiments, reported in Table 5.1. Differently from SVR optimization, the BO algorithm does not need an adjustment of the parameters space and it is able to identify automatically the "zones" where to focus the experiments. The chosen acquisition function is called "local penalization" [67]. This acquisition function was designed specifically for "batch optimization" in which each iteration (round) is composed by more than a single evaluation (experiment). The chosen batch had a size of 5 for each iteration, this kind of acquisition function allows to have five different suggested experiments each iteration. In this way, within the batch, the experiments will evolve from **exploitation**-oriented to **exploration**-oriented, resulting in a more explorative optimization compared to the SVR approach.

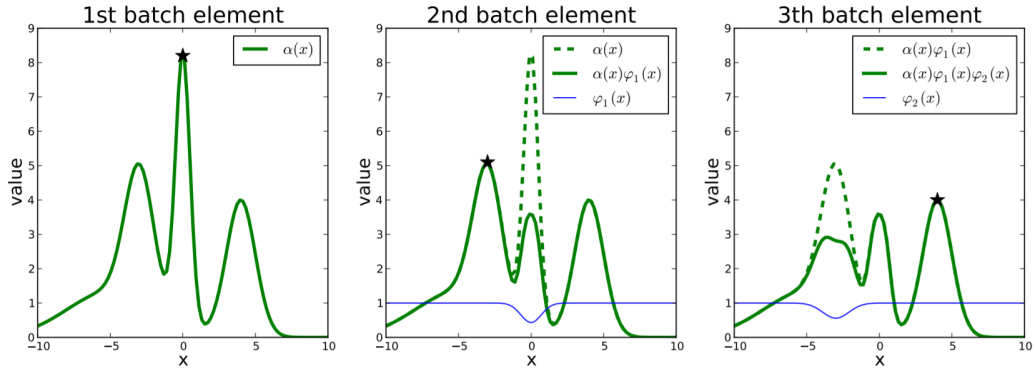

Figure 5.17: *Example of the working principle of "local penalization" acquisition function for a batch BO with batch size=3. The suggested experiments are depicted as black stars. Subsequently to the experiment suggestion, the acquisition function gets locally penalized, this leads to a better exploration of the space within the same iteration [67].*

The experiments suggested for the second round by the BO algorithm are reported in Table 5.11. The samples were then fabricated following the same procedure used previously. The outcome is reported in Fig 5.18.

Round 2 BO				
Sample	**Conc.** (g/L)	**Solv.**	**KCC** (°C)	***rpm***
20	5	Tol	30	1700
21	6	Mes	30	1800
22	3	Mes	30	1500
23	7	Mes	70	1500
24	6	Tol	30	2200

Table 5.11: *Table reporting the experiments performed in the second round of BO.*

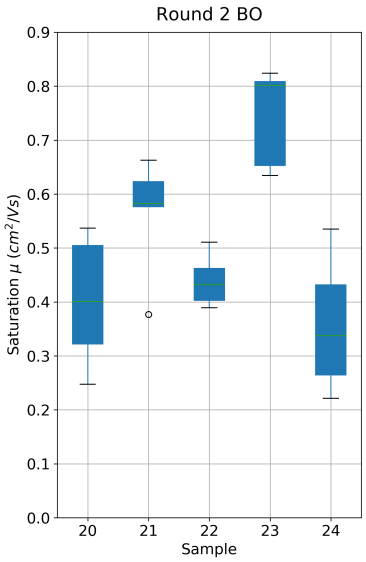

Figure 5.18: *Boxplot reporting the saturation mobility values for the second round of experiments guided by BO.*

The algorithm was then ran again with the data from the first and the second round. The suggested experiments are reported in Table 5.12 and the outcome in Fig 5.18.

Round 2 BO				
Sample	**Conc.** (g/L)	**Solv.**	**KCC** (°C)	***rpm***
30	5	Mes	50	1500
31	2	Mes	30	700
32	5	Mes	30	3000
33	12	Mes	30	600
34	1	Mes	120	500

Table 5.12: *Table reporting the experiments performed in the third round of BO.*

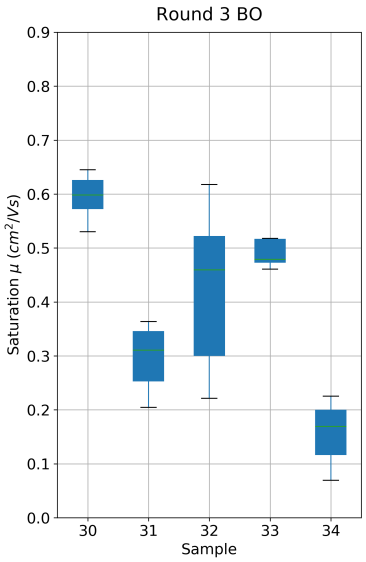

Figure 5.19: *Boxplot reporting the saturation mobility values for the third round of experiments guided by BO.*

Interestingly, in the last BO round it is possible to notice two important facts:

- The algorithm was able to identify the best solvent and, during the second round, all the sample were deposited from mesitylene.
- The first experiment of the batch (sample 30) was suggested "near" the best sample of the previous round (sample 23), this reflects the explotiation-oriented approach. The last experiment of the batch (sample 34), on the other hand, is characterized by a concentration and a spin-coating speed at the edge of the parameters space, where few experiments were performed, reflecting the more explorative approach.

5.1.6 Results

Both optimizations resulted in an overall improvement of the N2200 transistors. The final outcome of the optimization is reported in Fig 5.20 both for the aligned and the misaligned devices. The improvement can be seen by plotting the mean mobility value (Fig 5.21*(a)*) and the best device mobility (Fig 5.21*(b)*) for each round in the two optimization approaches. As expected, SVR optimization, being a more focused approach, resulted in an improvement of the entire batch during each round, as can be seen by the gradual improvement of the mean mobility. BO, on the other hand, being a more explorative approach, does not result in an improvement of the mean mobility during each round. Indeed, in the third round, most of the experiments were suggested in "unexplored" zones, and this resulted in a lower mean value of the overall batch.

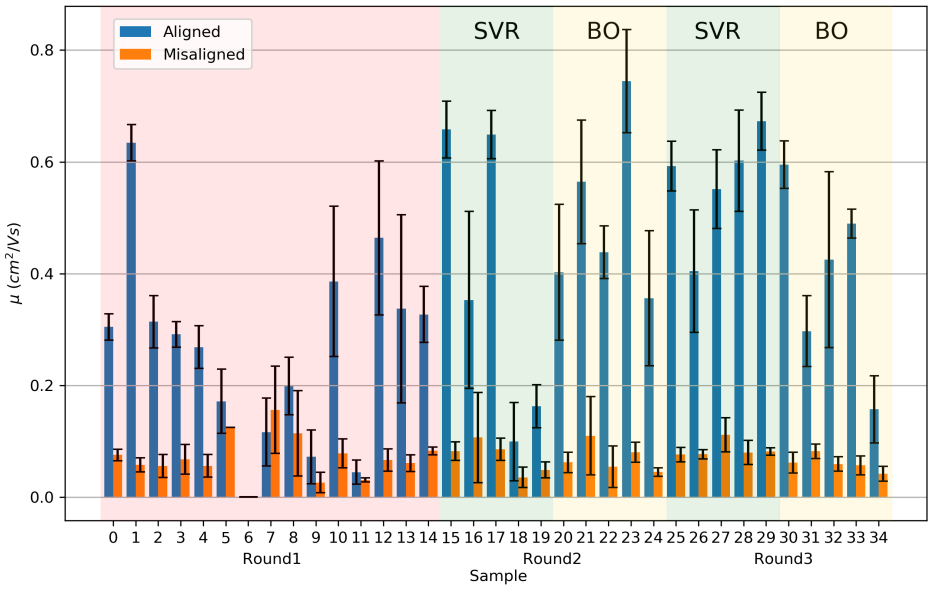

Figure 5.20: *Barplot reporting the outcome of the entire N2200 optimization. The saturation mobilities are reported both for aligned and misaligned devices. The experiments of the first round are highlighted in red, while the experiments of the SVR optimization and BO in green and yellow respectively.*

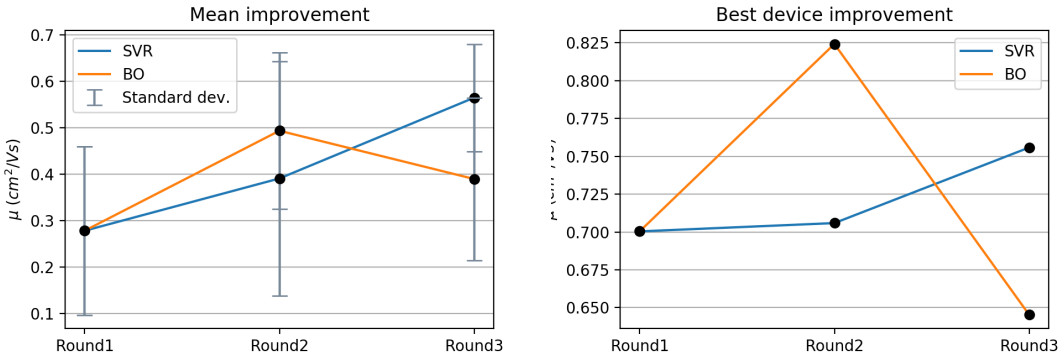

(a) *(b)*

Figure 5.21: *Evolution of the mean (a) and maximum (b) mobility value in each round for the two optimization methods.*

The complete dataset, reported in Table 5.13 and Fig 5.22, composed by all the experiments performed during the two optimizations was fitted using SVR. The hyperparameters for the SVR fitting were selected using the same approach described in Section 5.1.4 and are reported in Table 5.14. The contour plots obtained for the entire parameters space are reported from Fig 5.24 to 5.27.

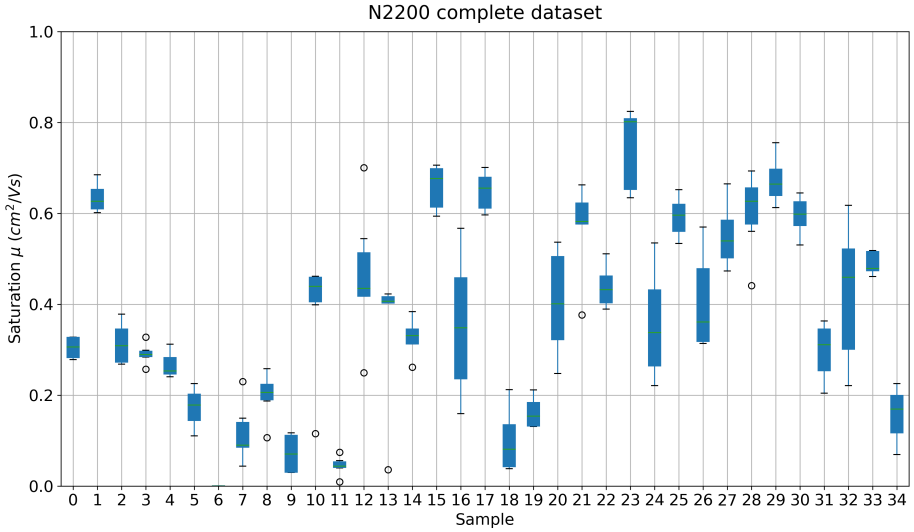

Figure 5.22: *Boxplot reporting the complete dataset obtained during N2200 optimization for the aligned devices.*

N2200 complete dataset					
Sample	**Conc.** (g/L)	**Solv.**	**KCC** (°C)	***rpm***	**Mean** μ (cm^2/Vs)
0	6	CB	40	600	0.304
1	4	Tol	30	1800	0.617
2	8	Tol	100	2800	0.314
3	5	Mes	140	1900	0.291
4	14	CB	50	900	0.269
5	3	CN	70	1200	0.172
6	1	CN	120	2900	$0.2 \cdot 10^{-3}$
7	7	CN	150	1100	0.116
8	15	CB	90	1600	0.199
9	13	Tol	130	800	0.072
10	2	Tol	50	2400	0.386
11	12	CN	60	2200	0.045
12	10	Mes	110	1400	0.464
13	11	Mes	80	2600	0.337
14	9	CB	100	2100	0.327
15	10	Mes	30	1500	0.658
16	5	Tol	50	1700	0.353
17	6	Mes	70	1900	0.649
18	8	Tol	60	1300	0.099
19	9	Tol	40	2100	0.163
20	5	Tol	30	1700	0.402
21	6	Mes	30	1800	0.564
22	3	Mes	30	1500	0.438
23	7	Mes	70	1500	0.744
24	6	Tol	30	2200	0.356
25	9	Mes	60	2000	0.593
26	10	Mes	70	1700	0.405
27	8	Mes	40	1900	0.551
28	6	Mes	50	1600	0.602
29	7	Mes	30	1800	0.673
30	5	Mes	50	1500	0.595
31	2	Mes	30	700	0.297
32	5	Mes	30	3000	0.425
33	12	Mes	30	600	0.490
34	1	Mes	120	500	0.157

Table 5.13: *Table reporting all the experiments performed during N2200 optimization.*

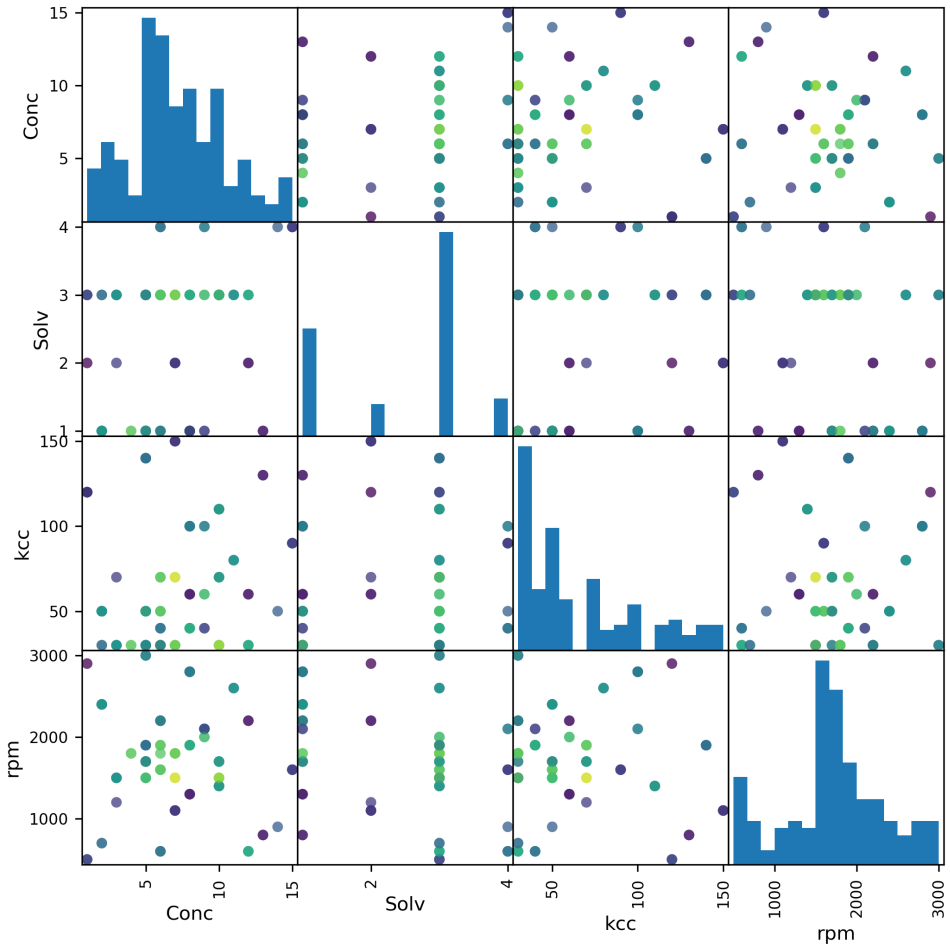

Figure 5.23: *Scatter matrix of the complete N2200 dataset. The solvents are reported as numbers from 1 to 4 (1=Tol, 2=CN, 3=Mes and 4= CB). The saturation mobility of the aligned device is qualitatively reported as color scale (purple="lower mobility" and yellow="higher mobility").*

Complete N2200 hyperparameters		
γ	C	ϵ
0.34	15	0.01

Table 5.14: *Hyperparameters selected for the SVR fitting of the complete N2200 dataset.*

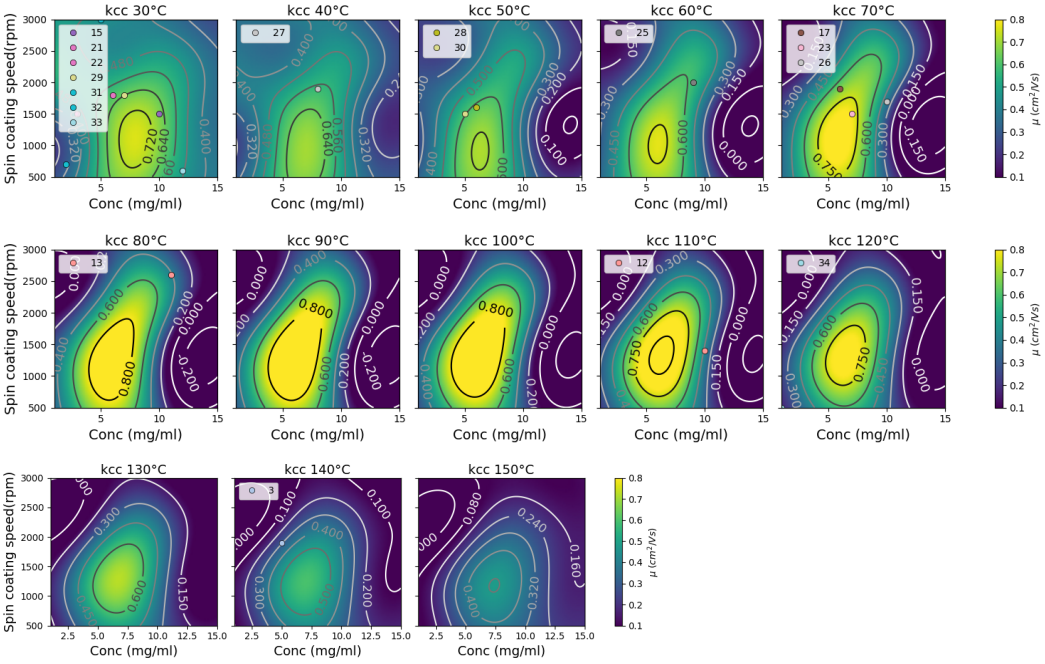

Figure 5.24: *SVR contour plots of the complete N2200 dataset for mesitylene.*

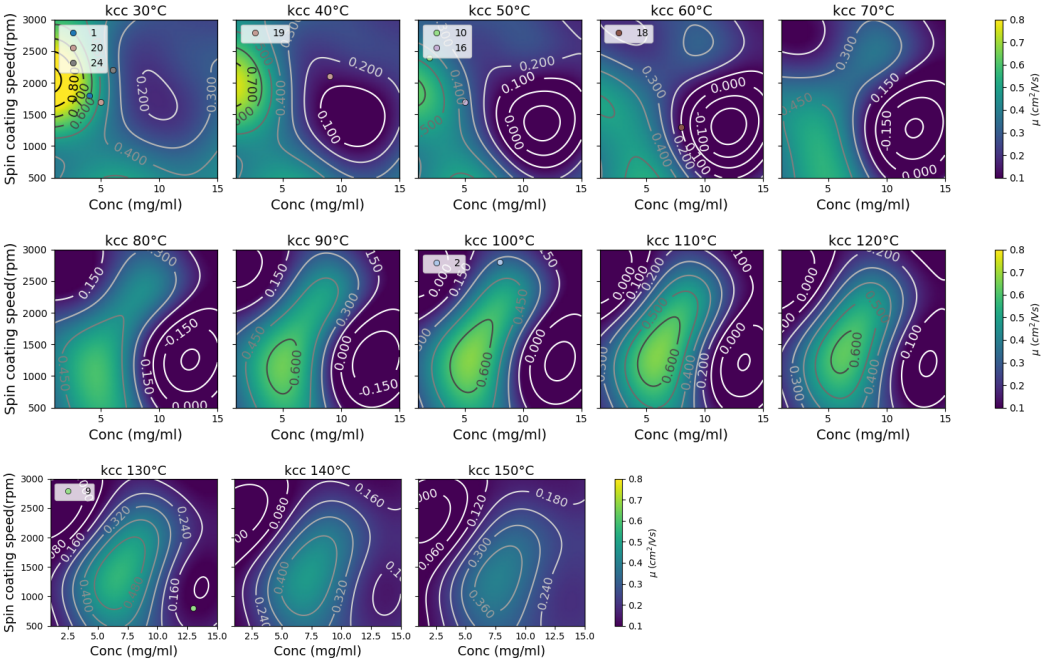

Figure 5.25: *SVR contour plots of the complete N2200 dataset for toluene.*

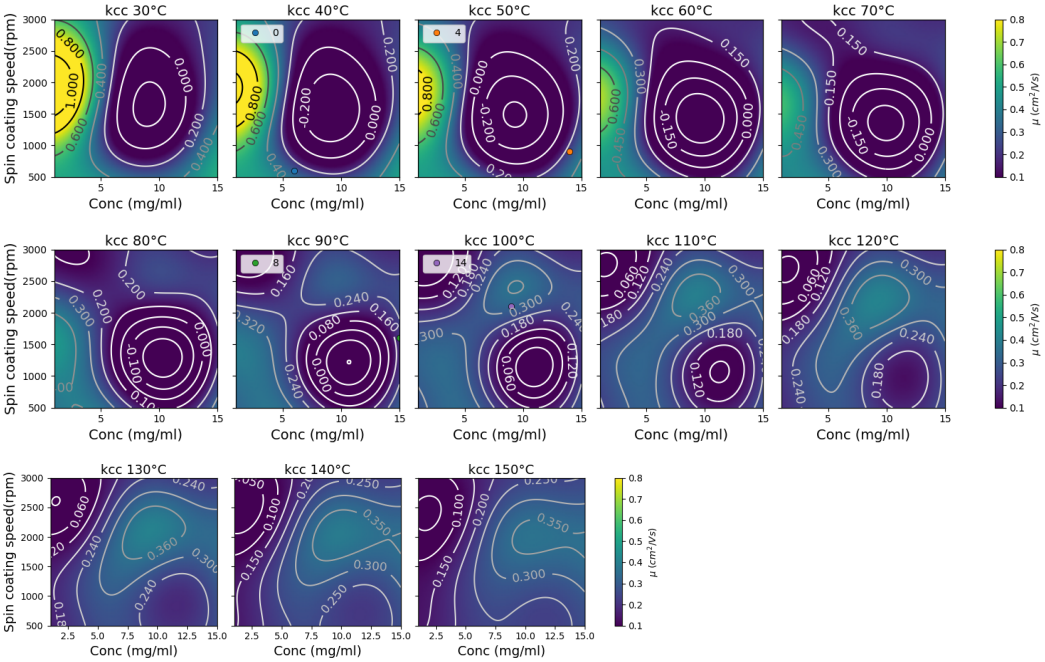

Figure 5.26: *SVR contour plots of the complete N2200 dataset for chlorobenzene.*

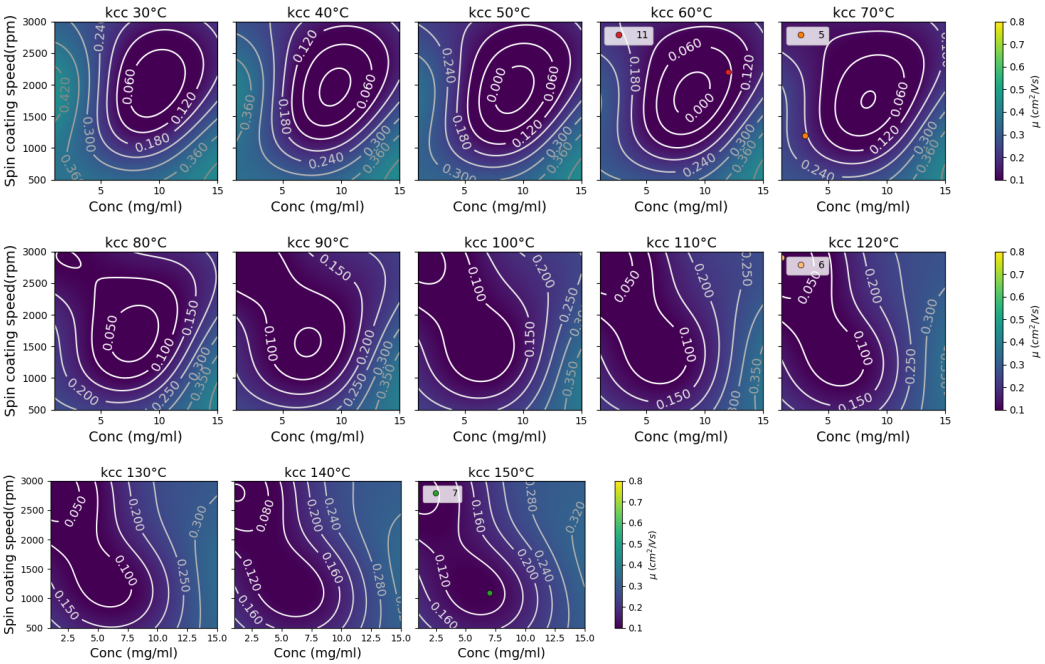

Figure 5.27: *SVR contour plots of the complete N2200 dataset for chloronaphthalene.*

It is interesting to notice that by "slicing" the fitted curve it is possible to obtain some "physically significant" results. For example, by plotting the predicted mobility as a function of the KCC (Fig 5.28*(a)* and *(b)*), it is possible to observe the predicted effect of the KCC. In order to make a comparison, the SVR fitted function was sliced at parameter values similar to the deposition parameters used in the work of Y. Kim et al. (Tol 10 g/L at 1000 rpm) [63]. The slice at $10g/L$ does not show the same trend obtained in the reference paper, although at lower concentrations (5 g/L) (Fig 5.28*(a)*) the trend resembles the results from the paper (Fig 5.28*(c)*), presenting a peak around 100 °C. This difference can be attributed to the other deposition conditions adopted. For instance, in the paper the off-center spin-coating was performed at 2 cm from the center instead of 3 cm. Obviously the lack of experimental data does not allow to draw solid conclusions, although this example demonstrate the power of machine learning-guided optimizations. Even if this work was not focused on the study of the effect of KCC, it was still able to identify the correct physical trend. Furthermore, it enables a "big picture" vision: by slicing at different parameter values, it is possible to see the influence of each variable on the trend of interest (in this example the influence of the concentration on the mobility versus KCC trend).

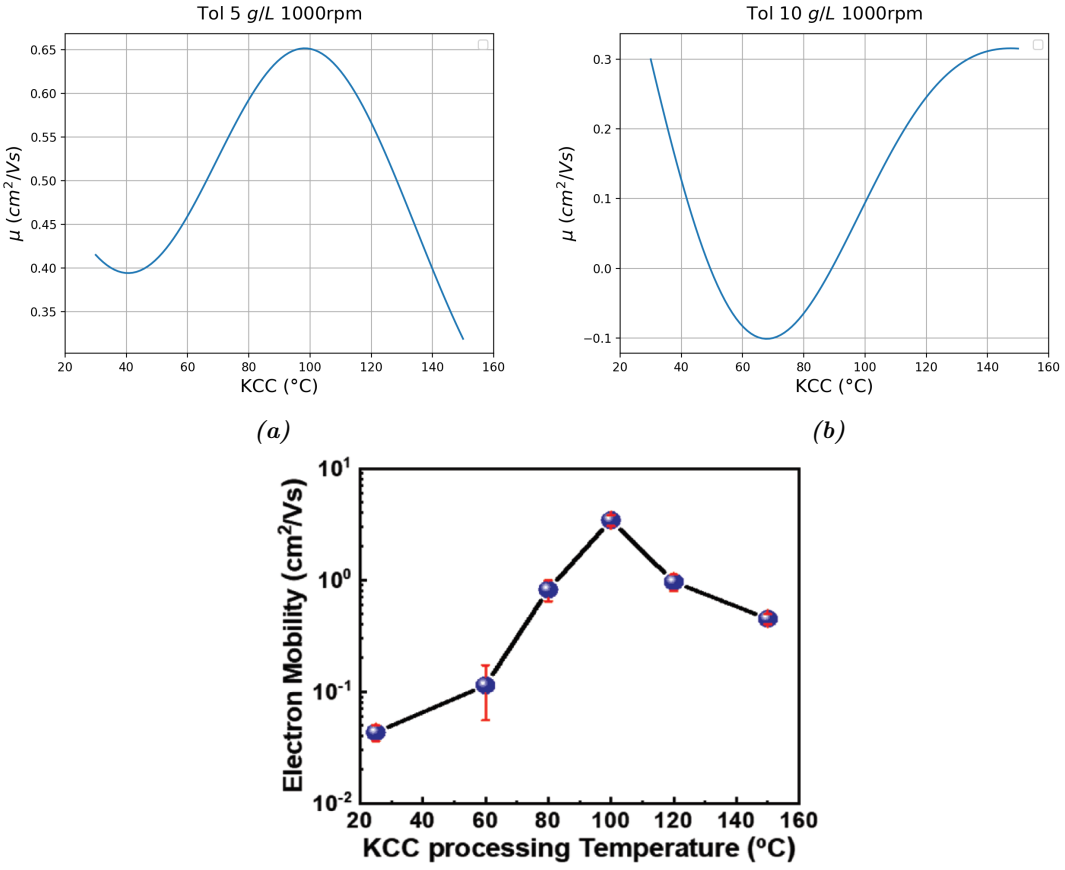

Figure 5.28: *Mobility versus KCC: (a) SVR fitting for Tol 5 g/L at 1000 rpm, (b) SVR fitting for Tol 10 g/L at 1000 rpm and (c) experimental data obtained by Y. Kim et al. [63].*

After the optimization, in order to characterize the film microstructure, N2200 was deposited onto some glass substrates following the same deposition parameters of the most interesting devices. Some microscope slides were cutted with a diamond-tip glass cutter and then cleaned following the usual procedure described in Section 4.2.3. N2200 was then deposited as for the most interesting samples. The deposited films were then characterized by means of polarized light microscopy (PLM) both in reflection and transmission regimes. In Fig 5.29 some cross-polarized microscopy images taken in transmission regime are reported.

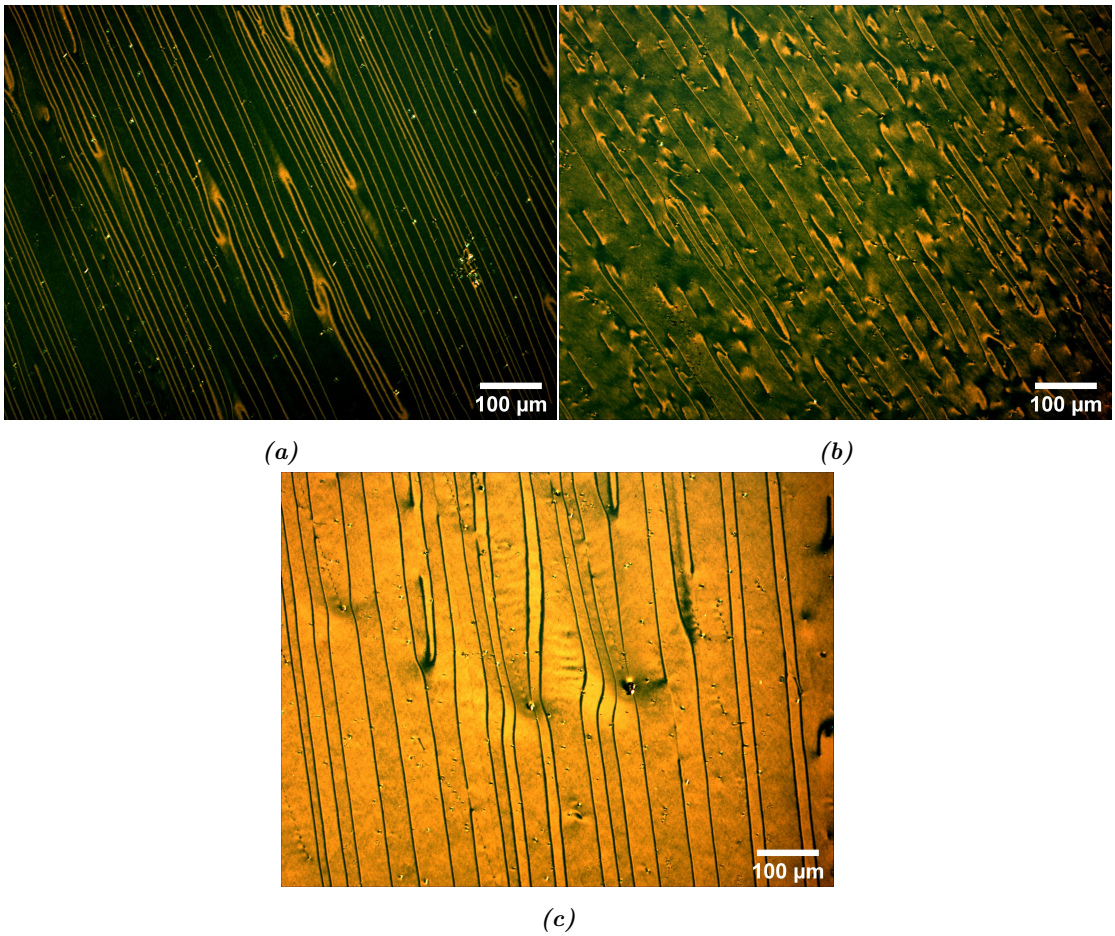

Figure 5.29: *Transmission cross-polarized microscopy images of the morphologies yielding the best device performances: (a) sample 1, (b) sample 23 and (c) sample 29.*

It is possible to notice the different morphologies obtained. For the film deposited with the same parameters of sample 1 (4 g/L in Tol at 1800 rpm and KCC at 30 °C) (Fig 5.29 *(a)*) the resulting domains are very elongated, although their lateral

dimension is relatively small. This may be due to the smaller degree of aggregation in solution of toluene with respect to mesitylene. For the film deposited with the parameters of sample 23 (7 g/L in Mes at 1500 rpm and KCC at 70 °C) (Fig 5.29 *(b)*) the resulting domains are larger but less elongated, probably because of the different KCC. Finally the ideal morphology was obtained for mesitylene solutions of 7 g/L deposited at 1800 rpm and KCC at 30 °C. This set of parameters was used to deposit the sample 29 that also presented the best saturation mobility at high voltage of the entire optimization. From the PLM image of the semiconductor film it is possible to observe the largest domains, characterized by millimetric-size lengths and lateral dimensions of over 50 μm.

The best OFETs were finally measured with the SPA in an extended range of voltages. In particular the best results were obtained for "sample 29", fabricated in the third SVR optimization round. The best device showed a saturation mobility of 5.58 cm^2/Vs, extracted with a drain voltage of 60 V and at gate voltage between 55 V and 58 V. The transfer curve and the mobility extraction are shown in Fig 5.30. The highest mobility extracted in one of the reference paper, using the same voltage range, was 3.99 cm^2/Vs [63]. This demonstrate the power of machine learning-assisted optimization. Indeed, with only three optimization rounds, it was possible to obtain competitive state-of-the-art results.

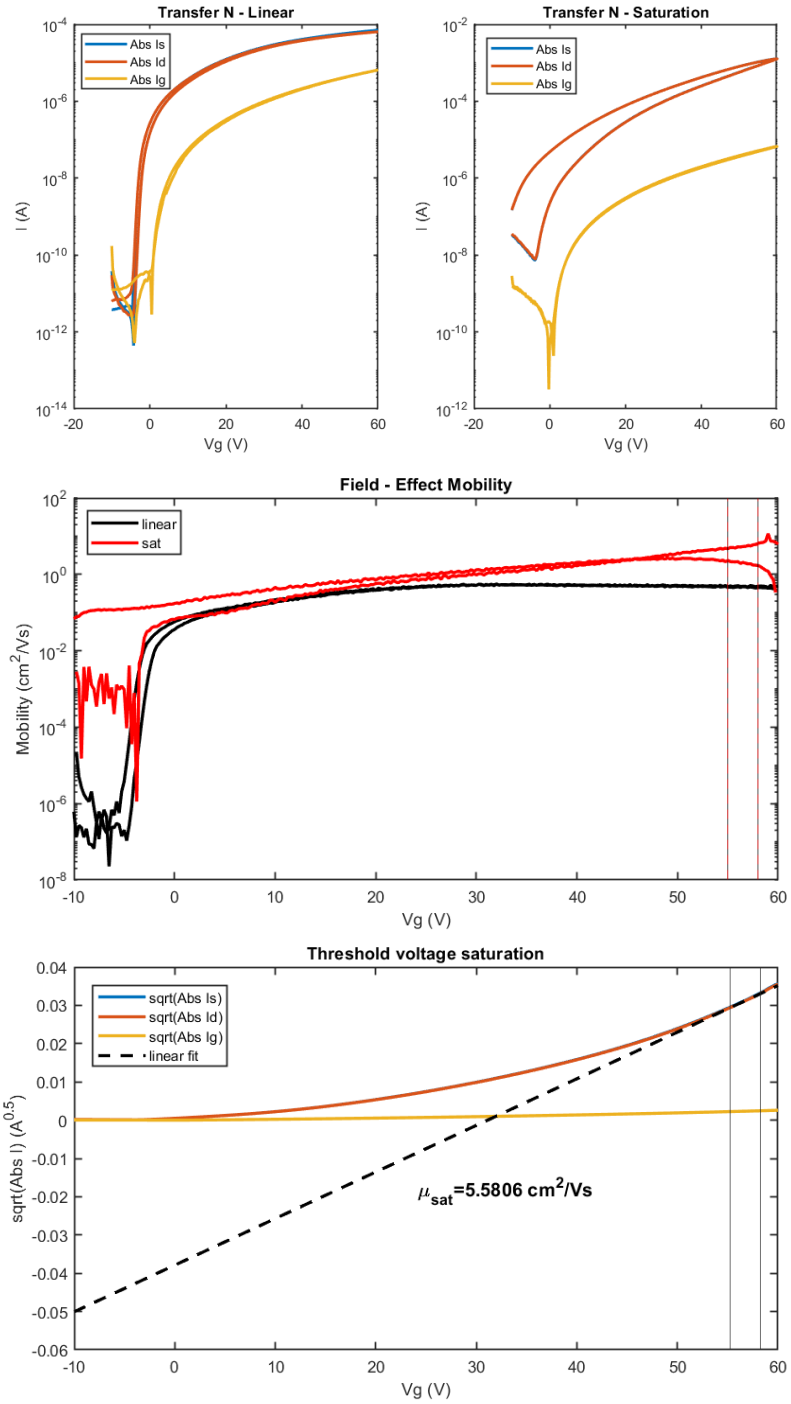

Figure 5.30: *Transfer curve and mobility extraction for sample 29 of N2200 optimization.*

5.2 Predictions for [3]Ph OFET

The first OFET based on carbon atomic wire (CAW) molecules was only recently demonstrated in a work by Printed and Molecular Electronics (PME) group researchers [19]. In the paper, A. D. Scaccabarozzi et al. fabricated a device with [3]Ph as semiconductor, deposited by drop-casting from a solution of dichloromethane. The achieved OFET mobility was in the order of 10^{-3} cm^2/Vs. The authors claimed that this value may be a big underestimation, since the simple drop-casting deposition led to a poor coverage of the device active area. They are trying to improve the performance of [3]Ph-based transistors experimenting other deposition techniques and conditions. Attempts in depositing the film with spin-coating techniques did not result in the formation of extended crystalline domains and, up to now, the best performances reported by the group were obtained with bar-coating [14].
Bar-coating is a technique commonly used in the deposition of organic semiconductors (OSCs). With this technique it is possible to place a dissolved OSC on a threaded bar. The bar rolls on the substrate and uniformly deposit the semiconductor. In order to favour the solvent evaporation usually the substrate is heated during the deposition. The crystallization process of [3]Ph, and small-molecule OSCs in general, is a complex phenomenon and its understanding is the key to the development of uniform films with extended crystalline domains [26, 68, 69]. Several variables impact the final semiconducting film morphology and, hence, the electrical performances of the devices. Some can be tuned during the deposition process, like bar-coating speed and temperature. Others are environmental conditions which are more difficult to keep under control, like humidity and exposition to light during the process. For instance, it was noted that also the random motion of the air due to the aspiration in the fume hood affects the deposition. For this reason the group is now blowing a flux of nitrogen onto the substrate during the bar-coating process, resulting in an increased reproducibility of the films.
For the first studies on the system, the variable selection was performed based on literature data of similar systems and on "spot" experiments. The dataset used in this work was obtained by depositing [3]Ph (pure and blended with polystyrene (PS)) from dichlorobenzene solutions using bar-coating with nitrogen flux. The semiconductor was deposited on silicon-silicon dioxide substrates with interdigitated gold contacts, yielding bottom-gate bottom-contacts (BGBC) OFETs. The substrate consists in 16 transistors with two parallel orientation and 4 different channel lengths (2.5, 5, 10 and 20 μm). The main variables screened so far are

listed in Table 5.15, while the parameters space considered for this optimization process are reported in Table 5.16. A better parameter screening is however required in order to have a better understanding of the system response. The DoE approach would be an excellent way to get a grasp on the relative influence and the importance of each deposition parameters. Indeed, the understanding of the interplay of these effects is one of the main challenges hampering the performance of cumulenes-based transistors.

[3]Ph deposition parameters		
bar-coating	**Blend**	**Substrate**
Speed	Solvent	Application of a SAM
Temperature	Polymer	
Nitrogen flux	Polymer concentration	
	[3]Ph concentration	

Table 5.15: *Main parameters influencing [3]Ph deposition.*

[3]Ph parameters space	
Variable	**Range**
Temperature	50 °C to 110 °C
[3]Ph concentration	2.5 g/L to 20 g/L
PS concentration	0 g/L to 20 g/L
SAM	PFBT or without SAM

Table 5.16: *Table reporting the parameters space of the [3]Ph dataset.*

The bar-coating deposition of the blend leads to three possible crystalline morphologies in the film. It is possible to observe the different domain structures with PLM (Fig 5.31). The morphology obtained is highly influenced by the deposition parameters, although a morphology-charge transport relationship still misses a good understanding for [3]Ph.

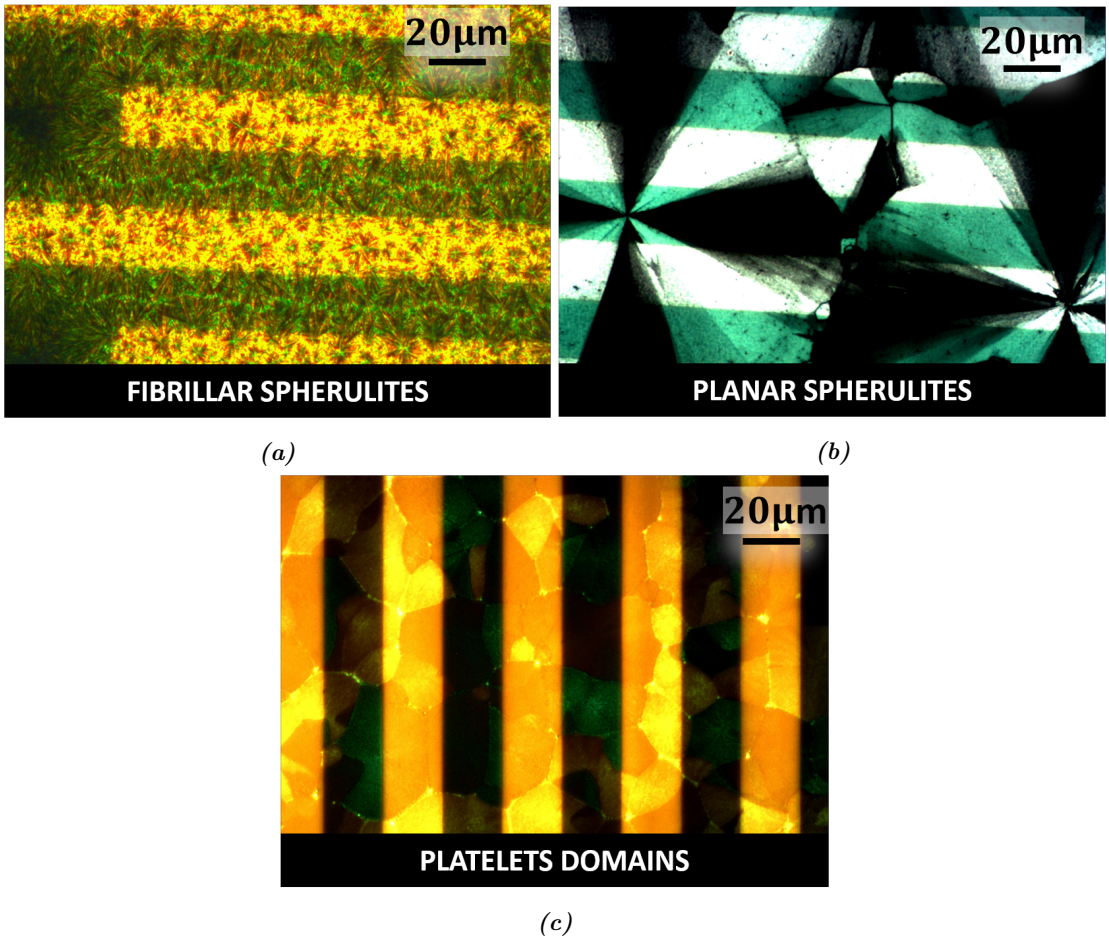

Figure 5.31: *PLM images of the three possible morphologies obtained in the [3]Ph films: (a) fibrillar spherulites, (b) planar spherulites and (c) platelets domains. The films were deposited onto interdigitated contacts (yellowish stripes), which presence severely affect the film morphology.*

5.2.1 Dataset analysis

As for the case of N2200, also for [3]Ph transistors the saturation mobility was chosen as the property to be optimized. The mobility measurements in the dataset presented a great variability and had to be refined in order to obtain a reliable fitting. First of all, the measurements for the short channel transistors (2.5 μm) were discarded in order not to take into account the short channel effects. Then only the top five mobility measurements were kept for each sample. In this way the variance for each sample was reduced, while still keeping a significant statistical power. Moreover, it is worth stressing that, especially in early stages optimization of materials properties, it is more important to target the maxima than the average values. The final dataset consisted of 28 different samples, each composed of three to five mobility measurements. Finally, because the data presented a wide range of mobility values, the logarithm base 10 of the mobility was selected for the fitting and the optimization. The refined dataset is reported in Fig 5.32 and in Table 5.17.

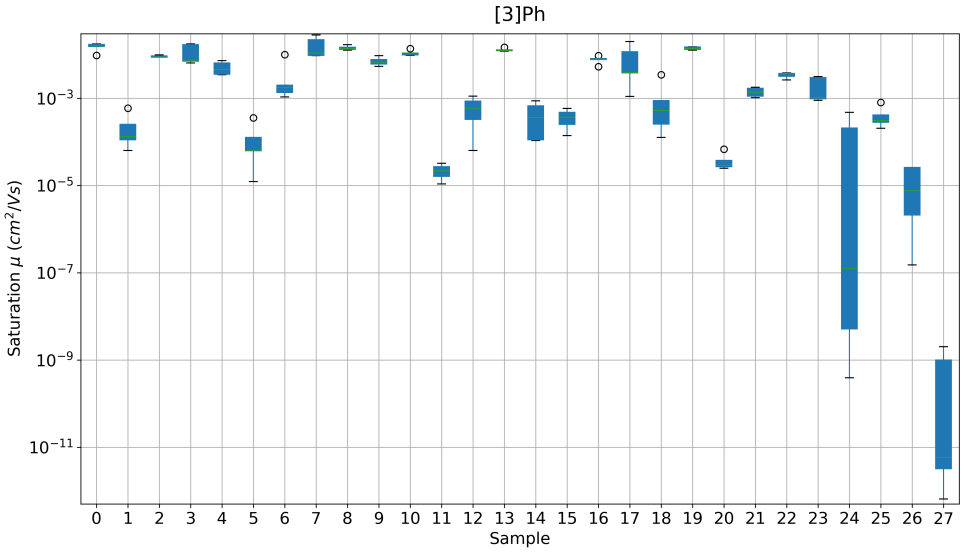

Figure 5.32: *Boxplot reporting the [3]Ph dataset.*

[3]Ph complete dataset					
Sample	**Temp. (°C)**	**[3]Ph conc.** (g/L)	**PS conc.** (g/L)	**SAM**	**Mean** μ (cm^2/Vs)
0	70	10	10	PFBT	$1.5 \cdot 10^{-2}$
1	110	10	10	PFBT	$2.3 \cdot 10^{-4}$
2	70	10	20	PFBT	$9.0 \cdot 10^{-3}$
3	70	10	5	PFBT	$1.1 \cdot 10^{-2}$
4	70	10	2.5	PFBT	$5.0 \cdot 10^{-3}$
5	90	10	10	PFBT	$1.2 \cdot 10^{-4}$
6	90	10	5	PFBT	$3.2 \cdot 10^{-3}$
7	70	10	5	NO SAM	$1.6 \cdot 10^{-2}$
8	60	10	5	PFBT	$1.4 \cdot 10^{-2}$
9	70	10	10	NO SAM	$7.0 \cdot 10^{-3}$
10	60	10	10	PFBT	$1.1 \cdot 10^{-2}$
11	100	10	10	NO SAM	$2.1 \cdot 10^{-5}$
12	110	10	10	NO SAM	$5.9 \cdot 10^{-4}$
13	80	10	5	PFBT	$1.3 \cdot 10^{-2}$
14	80	10	5	NO SAM	$4.2 \cdot 10^{-4}$
15	90	10	5	NO SAM	$3.6 \cdot 10^{-4}$
16	80	5	0	PFBT	$7.6 \cdot 10^{-3}$
17	50	20	0	NO SAM	$8.0 \cdot 10^{-3}$
18	80	10	10	NO SAM	$1.0 \cdot 10^{-3}$
19	80	10	0	NO SAM	$1.4 \cdot 10^{-2}$
20	110	5	0	PFBT	$3.7 \cdot 10^{-5}$
21	50	5	0	PFBT	$1.4 \cdot 10^{-3}$
22	50	10	0	PFBT	$3.4 \cdot 10^{-3}$
23	80	10	0	PFBT	$1.8 \cdot 10^{-3}$
24	110	10	0	PFBT	$1.4 \cdot 10^{-4}$
25	50	2.5	0	PFBT	$4.0 \cdot 10^{-4}$
26	80	2.5	0	PFBT	$1.2 \cdot 10^{-5}$
27	110	2.5	0	PFBT	$6.7 \cdot 10^{-10}$

Table 5.17: *Table reporting the [3]Ph dataset.*

5.2.2 Machine learning prediction

The dataset was fitted with SVR as for N2200 (Section 5.1.4). The selected hyperparameters are reported in Table 5.18. The prediction efficiency was checked with the graph in Fig 5.33, and the contour plots are reported in Fig 5.34 and 5.35.

[3]Ph hyperparameters		
γ	C	ϵ
0.25	25	0.1

Table 5.18: *Hyperparameters selected for the SVR fitting of [3]Ph.*

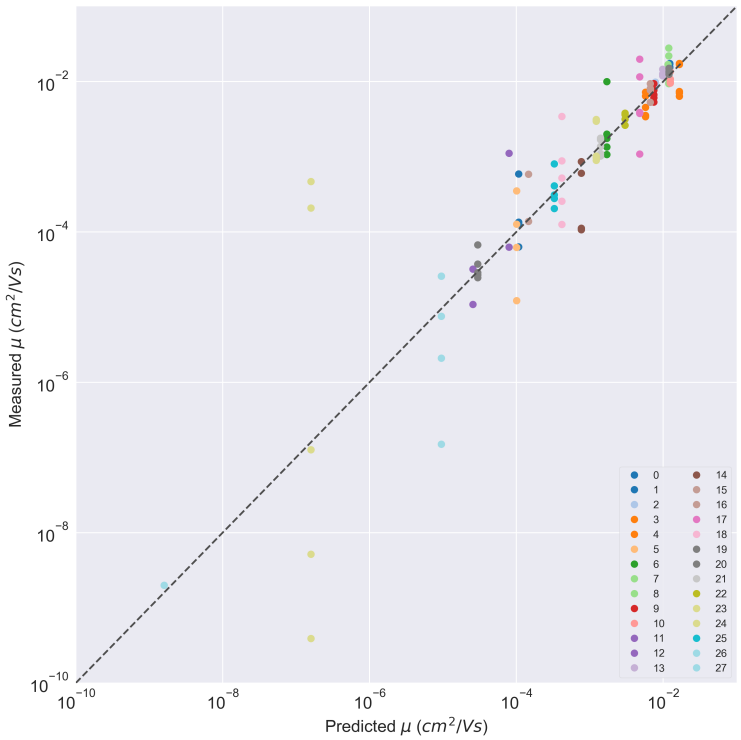

Figure 5.33: *Measured versus predicted mobility from the SVR of [3]Ph.*

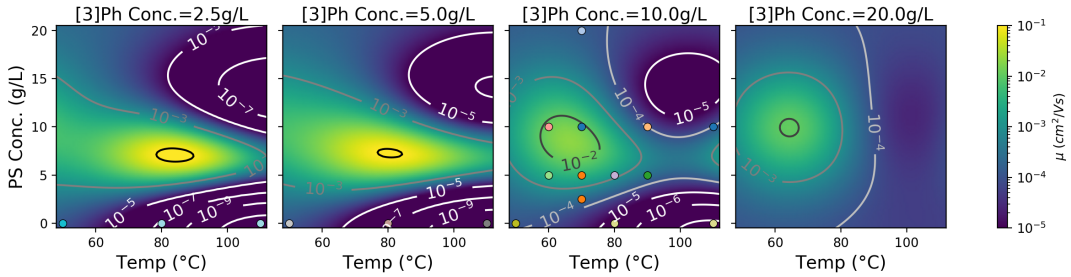

Figure 5.34: *SVR contour plots for [3]Ph with PFBT SAM.*

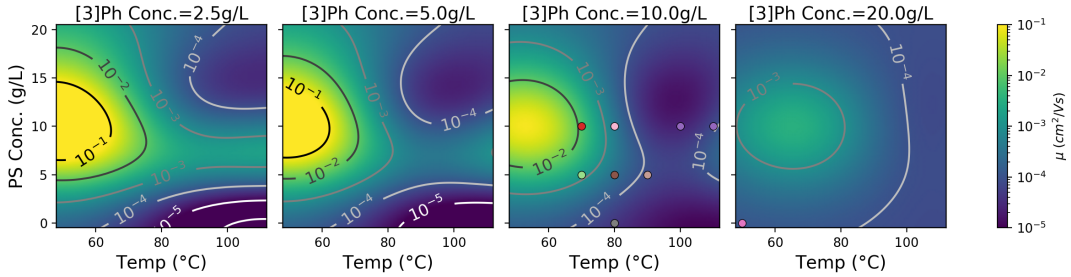

Figure 5.35: *SVR contour plots for [3]Ph without SAM.*

The lack of a DoE does not allow an efficient screening of the parameters space. As it is possible to notice in Fig 5.36, most of the experiments were performed with [3]Ph concentration of 10 g/L. For this reason, the prediction around that concentration are very accurate while at low and high [3]Ph concentrations the fitting is mostly based on extrapolation because few data are present. The predicted best PS concentration is clearly around 7.5 g/L and the deposition temperature below 80 °C. The role of the self-assemble monolayer (SAM) is not clear, although the mobility seems to be slightly higher for the devices without pentafluorotiophenol (PFBT). As discussed in Section 1.3.3, despite an improvement of charge injection, the application of a SAM can modify the crystallization process, and the resulting morphology can be less favourable for the charge transport.

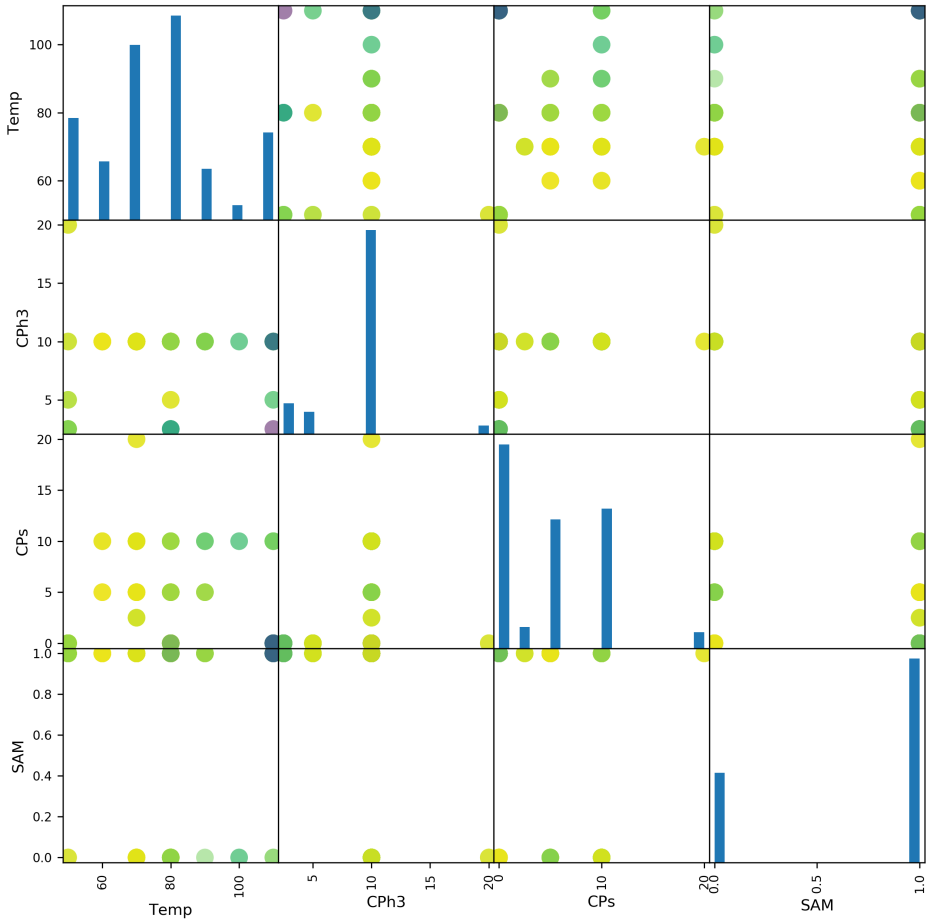

Figure 5.36: *Scatter matrix of the [3]Ph dataset. The SAM levels are reported as 0="No SAM" and 1="PFBT". The saturation mobility is qualitatively reported as color scale (purple="lower mobility" and yellow="higher mobility").*

With the same dataset, also a BO was tested. After the parameters space was defined, the model was trained with the data and 10 suggested experiments were obtained using a batch optimization with local penalization. The suggested experiments (reported in Table 5.19) were plotted over the SVR contour plots in order to assess the prediction consistency (Fig 5.37 and 5.38).

[3]Ph BO suggested experiments				
Sample	**Temp. (°C)**	**[3]Ph conc. (*g/L*)**	**PS conc. (*g/L*)**	**SAM**
0	70	10	7.5	PFBT
1	60	10	7.5	PFBT
2	70	10	7.5	NO
3	70	10	2.5	NO
4	60	10	2.5	PFBT
5	80	7.5	0	PFBT
6	70	12.5	7.5	PFBT
7	70	7.5	7.5	PFBT
8	70	7.5	5	PFBT
9	80	7.5	2.5	PFBT

Table 5.19: *Table reporting the experiments suggested by the BO algorithm for [3]Ph.*

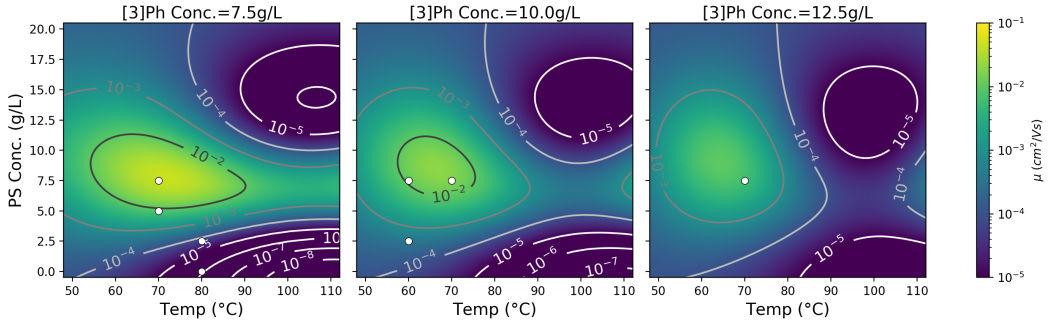

Figure 5.37: *BO suggested experiments (white dots) plotted over SVR contour plots for [3]Ph with PFBT SAM.*

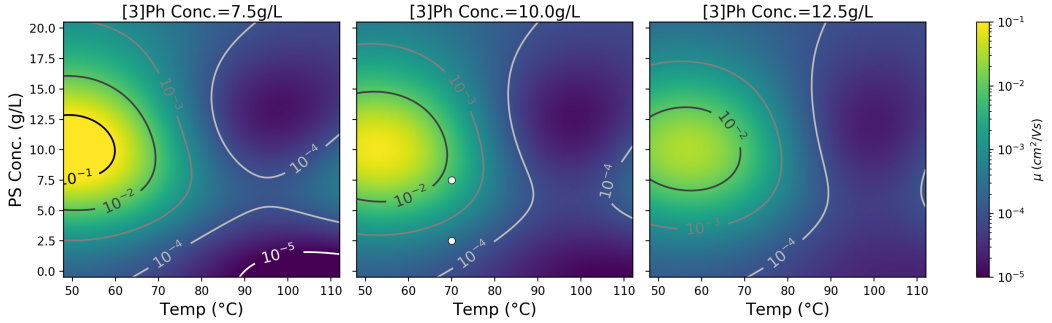

Figure 5.38: *BO suggested experiments (white dots) plotted over SVR contour plots for [3]Ph without SAM.*

Regarding the future experiments for this kind of system, a new DoE, considering as many deposition parameters as possible, can be used as starting point for a more detailed optimization. Given the large number of parameters, probably BO would be a better solution for guiding the initial rounds of the optimization. BO, indeed, does not require the experimentalist to "read" the fitted curves, thus allowing an higher dimensional optimization. In a second phase the data can be fitted with SVR in order to understand the interaction between the parameters and get a physical intuition of the system response. The curves obtained with SVR are an extremely powerful tool for the understanding of variables interactions and, in contrast to BO, enable the experimentalist to see the "big picture".

Chapter 6

Conclusion and perspectives

In this thesis work, the use of machine learning techniques to support the efficient optimization of the mobility of organic field-effect transistors (OFETs) has been studied. In particular two machine learning-guided optimization techniques, based on support vector regression (SVR) and bayesian optimization (BO), were adopted.

In the first part of the thesis, the two optimization techniques were validated and compared to maximize the charge mobility of OFETs employing N2200 as semiconducting material. The optimization started with the selection of the variables to be considered for optimizing the deposition and their range. Once the variables space was defined, the first round of experiments was planned following a design of experiments (DoE) obtained using GPyOpt [12]. Starting from the results of the first round, the two machine learning-based optimization approaches were carried out separately. Both the optimization techniques lead to an improvement of the mobility. SVR optimization allowed a better visualization of the optimization process by returning contour plots of the fitted function. By "reading" these plots, it was possible to focus the experiments of the subsequent rounds in the area of interest, thus guiding the research towards the optimal mobility. With the fabrication of 15 different samples in the fisrt round and another 10 for each optimization method, it was possible to obtain mobility values higher than the ones obtained in the reference paper. In particular, the best device was obtained in the SVR optimization, showing a saturation mobility of 5.58 cm^2/Vs, compared to the best mobility of 3.99 cm^2/Vs extracted by Y. J. Kim et al. [63].

In the second part of the thesis, SVR and BO were used to draw predictions on OFETs fabricated from a new kind of small-molecule organic semiconductor

(OSC), based on carbon atomic wires (CAWs). After a preprocessing of the data, the models were trained and it was possible to obtain a better visualization of the dependence of the mobility on the fabrication parameters in this kind of system. The predictions from SVR and the experiments suggested by BO will be useful leading the future studies on this new system. However, a new DoE, including a larger number of fabrication parameters, is required for a better screening of the parameters space. Starting from this new DoE, probably BO would have a better performance than SVR in guiding the experiments. BO, indeed, does not rely on the visualization of the fitted curve. For this reason, it can be used to guide the experiments in a parameters space with a large number of dimensions. At the same time, SVR allows a better visualization of the optimization process, thus, it can be used to support the bayesian predictions and help the experimentalist to get a physical insight of the problem.

A challenge for future improvements of the model consists in including direct structural information. For instance, in the case of [3]Ph, it might be possible to include a variable describing the kind of polymorph. This would require a classification algorithm to analyze, for example, polarized light microscopy (PLM) or atomic force microscopy (AFM) images. This may help the understanding of the role of morphology on the charge transport properties in [3]Ph OFETs which is nowadays lacking. Moreover, the architecture of the transistor might be changed, passing from a bottom-gate bottom-contacts (BGBC) configuration to top-gate bottom-contacts (TGBC). In this perspective, a new optimization task has to be performed. The information obtained from the study on BGBC OFETs can guide the choice of the relevant variables and ranges for the new optimization, improving its predicting ability and reducing the number of experiments required.

The two optimization approaches used in this thesis have proven an extremely useful tool to guide the optimization of OFETs mobilities. Compared to the usual one variable at a time (OVAT) approach which requires a much larger number of experiments to obtain the same results. Moreover, these methods can be generalized and used in many experimental fields. Hence, it is reasonable to think that machine learning methods will become an essential tool for twenty-first century researchers.

Appendix A

Kernel method

In order to better understand the kernel method introduced in Section 3.2.2, a rigorous mathematical treatment is required.
Starting from the equation of the hyperplane reported in Eq 3.7:

$$\hat{y} = \langle \boldsymbol{w} \cdot \boldsymbol{x} \rangle + b$$

the objective is to minimize the risk functional of Eq 3.8:

$$R = \frac{1}{2}\|\boldsymbol{w}\|^2 + C\sum_{i=1}^{m} |\hat{y}_D^{(i)} - y_D^{(i)}|_\epsilon$$

Through Lagrangian theory [70, 71] it is possible to solve the following minimization problem:

$$\text{minimize } \frac{1}{2}\|\boldsymbol{w}\|^2 + C\sum_{i=1}^{m} |\hat{y}_D^{(i)} - y_D^{(i)}|_\epsilon \tag{6.1}$$

which can be rewritten as a function of two non-negative slack variables $\xi^{(i)}$ and $\xi^{*(i)}$.

$$\text{minimize } \frac{1}{2}\|\boldsymbol{w}\|^2 + C\sum_{i=1}^{m} (\xi^{(i)} + \xi^{*(i)}) \tag{6.2}$$

$$\text{subjected to } \begin{cases} y_D^{(i)} - \langle \boldsymbol{w} \cdot \boldsymbol{x}_D \rangle + b \leq \epsilon + \xi^{(i)} \\ \langle \boldsymbol{w} \cdot \boldsymbol{x}_D \rangle + b - y_D^{(i)} \leq \epsilon + \xi^{*(i)} \\ \xi^{(i)}, \xi^{*(i)} \geq 0 \end{cases}$$

it is now possible to minimize the function using the Lagrangian multiplier method. The resulting Lagrangian function will be:

$$\begin{aligned} L = \frac{1}{2}\|\boldsymbol{w}\|^2 + C\sum_{i=1}^{m}(\xi^{(i)} + \xi^{*(i)}) - \sum_{i=1}^{m}\alpha^{(i)}(\epsilon + \xi^{(i)} - y_D^{(i)} + \langle \boldsymbol{w}\cdot\boldsymbol{x}_D^{(i)}\rangle + b) \\ - \sum_{i=1}^{m}\alpha^{*(i)}(\epsilon + \xi^{*(i)} + y_D^{(i)} - \langle \boldsymbol{w}\cdot\boldsymbol{x}_D^{(i)}\rangle - b) - \sum_{i=1}^{m}(\eta^{(i)}\xi^{(i)} + \eta^{*(i)}\xi^{*(i)}) \end{aligned} \tag{6.3}$$

where α, α^*, η and η^* are the Lagrangian multiplier. Through Lagrangian theory, necessary conditions for the multipliers to be a solution to the original optimization problem are:

$$\frac{\partial L}{\partial b} = \sum_{i=1}^{m}(\alpha^{*(i)} - \alpha^{(i)}) = 0 \tag{6.4}$$

$$\frac{\partial L}{\partial \boldsymbol{w}} = \boldsymbol{w} - \sum_{i=1}^{m}(\alpha^{*(i)} - \alpha^{(i)})\boldsymbol{x}_D^{(i)} = 0 \tag{6.5}$$

$$\frac{\partial L}{\partial \xi^{(i)}} = C - \alpha^{(i)} - \eta^{(i)} = 0 \tag{6.6}$$

$$\frac{\partial L}{\partial \xi^{*(i)}} = C - \alpha^{*(i)} - \eta^{*(i)} = 0 \tag{6.7}$$

Finally from Eq 6.5 it is possible to obtain the following relationship:

$$\boldsymbol{w} = \sum_{i=1}^{m}(\alpha^{*(i)} - \alpha^{(i)})\boldsymbol{x}_D^{(i)} \tag{6.8}$$

thus, Eq 3.7 becomes:

$$\hat{y} = \sum_{i=1}^{m}(\alpha^{*(i)} - \alpha^{(i)})\langle \boldsymbol{x}_D^{(i)}\cdot\boldsymbol{x}\rangle + b \tag{6.9}$$

Thus, the training algorithm and the regression function $\hat{y}$ can be expressed in terms of the dot product $\langle \boldsymbol{x}_D^{(i)}\cdot\boldsymbol{x}\rangle$.
Non-linear function approximations can be achieved by replacing the dot product

of input vectors with a nonlinear transformation on the input vectors. This transformation is referred to as the kernel function and is represented by $k(\boldsymbol{x}_D, \boldsymbol{x})$.
The final expression for the regression function is:

$$\hat{y} = \sum_{i=1}^{m} (\alpha^{*(i)} - \alpha^{(i)}) k(\boldsymbol{x}_D^{(i)}, \boldsymbol{x}) + b \tag{6.10}$$

and by using different kernels (some of which are reported in Table 3.1) it is possible to fit non-linear functions.

List of Figures

List of Tables

Bibliography

[1] C. W. Tang and S. A. VanSlyke, "Organic electroluminescent diodes," *Applied physics letters*, vol. 51, no. 12, pp. 913–915, 1987.

[2] S. R. Forrest and M. E. Thompson, "Introduction: Organic electronics and optoelectronics," *Chemical Reviews*, vol. 107, no. 4, pp. 923–925, 2007.

[3] B. Cao, L. A. Adutwum, A. O. Oliynyk, E. J. Luber, B. C. Olsen, A. Mar, and J. M. Buriak, "How to optimize materials and devices via design of experiments and machine learning: Demonstration using organic photovoltaics," *ACS nano*, vol. 12, no. 8, pp. 7434–7444, 2018.

[4] W. Shi, D. Wang, and Z. Shuai, "High-performance organic thermoelectric materials: Theoretical insights and computational design," *Advanced Electronic Materials*, vol. 5, no. 11, p. 1 800 882, 2019.

[5] A. Perinot, B. Passarella, M. Giorgio, and M. Caironi, "Walking the route to ghz solution-processed organic electronics: A heroic exploration," *Advanced Functional Materials*, vol. 30, no. 20, p. 1 907 641, 2020.

[6] J. Mei, Y. Diao, A. L. Appleton, L. Fang, and Z. Bao, "Integrated materials design of organic semiconductors for field-effect transistors," *Journal of the American Chemical Society*, vol. 135, no. 18, pp. 6724–6746, 2013.

[7] Y. H. Lee, O. Y. Kweon, H. Kim, J. H. Yoo, S. G. Han, and J. H. Oh, "Recent advances in organic sensors for health self-monitoring systems," *Journal of Materials Chemistry C*, vol. 6, no. 32, pp. 8569–8612, 2018.

[8] C. D. Dimitrakopoulos and P. R. Malenfant, "Organic thin film transistors for large area electronics," *Advanced materials*, vol. 14, no. 2, pp. 99–117, 2002.

[9] H. Matsui, Y. Takeda, and S. Tokito, "Flexible and printed organic transistors: From materials to integrated circuits," *Organic Electronics*, vol. 75, p. 105 432, 2019.

[10] A. Facchetti, "π-conjugated polymers for organic electronics and photovoltaic cell applications," *Chemistry of Materials*, vol. 23, no. 3, pp. 733–758, 2011.

[11] C. S. Casari, M. Tommasini, R. R. Tykwinski, and A. Milani, "Carbon-atom wires: 1-d systems with tunable properties," *Nanoscale*, vol. 8, no. 8, pp. 4414–4435, 2016.

[12] T. G. authors, *Gpyopt: A bayesian optimization framework in python*, `http://github.com/SheffieldML/GPyOpt`, 2016.

[13] G. Van Rossum and F. L. Drake, *Python 3 Reference Manual*. Scotts Valley, CA: CreateSpace, 2009, ISBN: 1441412697.

[14] T. Losi, "Field effect transistors based on sp2-sp carbon molecules," 2019.

[15] V. Subramanian, *Organic field-effect transistors, optical science and engineering series*, 2007.

[16] H. Sirringhaus, T. Sakanoue, and J.-F. Chang, "Charge-transport physics of high-mobility molecular semiconductors," *physica status solidi (b)*, vol. 249, no. 9, pp. 1655–1676, 2012.

[17] M. Richter, T. Heumüller, G. J. Matt, W. Heiss, and C. J. Brabec, "Carbon photodetectors: The versatility of carbon allotropes," *Advanced Energy Materials*, vol. 7, no. 10, p. 1 601 574, 2017.

[18] J. Y. Oh, S. Rondeau-Gagné, Y.-C. Chiu, A. Chortos, F. Lissel, G.-J. N. Wang, B. C. Schroeder, T. Kurosawa, J. Lopez, T. Katsumata, *et al.*, "Intrinsically stretchable and healable semiconducting polymer for organic transistors," *Nature*, vol. 539, no. 7629, pp. 411–415, 2016.

[19] A. D. Scaccabarozzi, A. Milani, S. Peggiani, S. Pecorario, B. Sun, R. R. Tykwinski, M. Caironi, and C. S. Casari, "A field-effect transistor based on cumulenic sp-carbon atomic wires," *The journal of physical chemistry letters*, vol. 11, no. 5, pp. 1970–1974, 2020.

[20] V. Coropceanu, J. Cornil, D. A. da Silva Filho, Y. Olivier, R. Silbey, and J.-L. Brédas, "Charge transport in organic semiconductors," *Chemical reviews*, vol. 107, no. 4, pp. 926–952, 2007.

[21] M. Myronov, "Molecular beam epitaxy of high mobility silicon, silicon germanium and germanium quantum well heterostructures," in *Molecular Beam Epitaxy*, Elsevier, 2018, pp. 37–54.

[22] A. Troisi, "Charge transport in high mobility molecular semiconductors: Classical models and new theories," *Chemical Society Reviews*, vol. 40, no. 5, pp. 2347–2358, 2011.

[23] J. Rivnay, L. H. Jimison, J. E. Northrup, M. F. Toney, R. Noriega, S. Lu, T. J. Marks, A. Facchetti, and A. Salleo, "Large modulation of carrier transport by grain-boundary molecular packing and microstructure in organic thin films," *Nature materials*, vol. 8, no. 12, pp. 952–958, 2009.

[24] M. Mas-Torrent, P. Hadley, S. T. Bromley, X. Ribas, J. Tarrés, M. Mas, E. Molins, J. Veciana, and C. Rovira, "Correlation between crystal structure and mobility in organic field-effect transistors based on single crystals of tetrathiafulvalene derivatives," *Journal of the American Chemical Society*, vol. 126, no. 27, pp. 8546–8553, 2004.

[25] G. Pace, A. Grimoldi, D. Natali, M. Sampietro, J. E. Coughlin, G. C. Bazan, and M. Caironi, "All-organic and fully-printed semitransparent photodetectors based on narrow bandgap conjugated molecules," *Advanced Materials*, vol. 26, no. 39, pp. 6773–6777, 2014.

[26] C. He, Y. He, X. Liu, A. Li, J. Chen, and H. Meng, "Enhancing the performance of solution-processed organic thin-film transistors by blending binary compatible small molecule semiconductors," *Organic Electronics*, vol. 64, pp. 104–109, 2019.

[27] H. Opoku, B. Nketia-Yawson, E. S. Shin, and Y.-Y. Noh, "Controlling organization of conjugated polymer films from binary solvent mixtures for high performance organic field-effect transistors," *Organic Electronics*, vol. 41, pp. 198–204, 2017.

[28] D. Khim, H. Han, K.-J. Baeg, J. Kim, S.-W. Kwak, D.-Y. Kim, and Y.-Y. Noh, "Simple bar-coating process for large-area, high-performance organic field-effect transistors and ambipolar complementary integrated circuits," *Advanced Materials*, vol. 25, no. 31, pp. 4302–4308, 2013.

[29] D. Khim, A. Luzio, G. E. Bonacchini, G. Pace, M.-J. Lee, Y.-Y. Noh, and M. Caironi, "Uniaxial alignment of conjugated polymer films for high-performance organic field-effect transistors," *Advanced Materials*, vol. 30, no. 20, p. 1 705 463, 2018.

[30] J. Smith, R. Hamilton, Y. Qi, A. Kahn, D. D. Bradley, M. Heeney, I. McCulloch, and T. D. Anthopoulos, "The influence of film morphology in high-mobility small-molecule: Polymer blend organic transistors," *Advanced Functional Materials*, vol. 20, no. 14, pp. 2330–2337, 2010.

[31] A. Luzio, L. Criante, V. D'innocenzo, and M. Caironi, "Control of charge transport in a semiconducting copolymer by solvent-induced long-range order," *Scientific reports*, vol. 3, p. 3425, 2013.

[32] J. Smith, M. Heeney, I. McCulloch, J. N. Malik, N. Stingelin, D. D. Bradley, and T. D. Anthopoulos, "Percolation behaviour in high mobility p-channel polymer/small-molecule blend organic field-effect transistors," *Organic Electronics*, vol. 12, no. 1, pp. 143–147, 2011.

[33] D. Natali and M. Caironi, "Charge injection in solution-processed organic field-effect transistors: Physics, models and characterization methods," *Advanced Materials*, vol. 24, no. 11, pp. 1357–1387, 2012.

[34] G. Horowitz, "Organic field-effect transistors," *Advanced materials*, vol. 10, no. 5, pp. 365–377, 1998.

[35] V. Koncar, *Smart textiles and their applications*. Woodhead Publishing, 2016.

[36] Y. Xu, C. Liu, D. Khim, and Y.-Y. Noh, "Development of high-performance printed organic field-effect transistors and integrated circuits," *Physical Chemistry Chemical Physics*, vol. 17, no. 40, pp. 26 553–26 574, 2015.

[37] C. Liu, Y. Xu, and Y.-Y. Noh, "Contact engineering in organic field-effect transistors," *Materials Today*, vol. 18, no. 2, pp. 79–96, 2015.

[38] J. Roh, T. Lee, C.-m. Kang, J. Kwak, P. Lang, G. Horowitz, H. Kim, and C. Lee, "Injection-modulated polarity conversion by charge carrier density control via a self-assembled monolayer for all-solution-processed organic field-effect transistors," *Scientific reports*, vol. 7, p. 46 365, 2017.

[39] M. Waldrip, O. D. Jurchescu, D. J. Gundlach, and E. G. Bittle, "Contact resistance in organic field-effect transistors: Conquering the barrier," *Advanced Functional Materials*, p. 1 904 576, 2019.

[40] A. La Torre, A. Botello-Mendez, W. Baaziz, J.-C. Charlier, and F. Banhart, "Strain-induced metal–semiconductor transition observed in atomic carbon chains," *Nature communications*, vol. 6, no. 1, pp. 1–7, 2015.

[41] C. S. Casari and A. Milani, "Carbyne: From the elusive allotrope to stable carbon atom wires," *MRS Communications*, vol. 8, no. 2, pp. 207–219, 2018.

[42] A. Milani, A. L. Bassi, V. Russo, M. Tommasini, and C. Casari, "Linear carbon: From 1d carbyne to 2d hybrid sp-sp2 nanostructures beyond graphene," *Handbook of Graphene, Volume 3: Graphene-like 2D Materials*, p. 297, 2019.

[43] M. Zhang, *Handbook of Graphene, Volume 3: Graphene-like 2D Materials*. John Wiley & Sons, 2019.

[44] M. Fowler. (2007). Electrons in one dimension: The peierls transition, [Online]. Available: `http://galileo.phys.virginia.edu/classes/752.mf1i.spring03/PeierlsTrans.htm` (visited on 06/12/2020).

[45] W. Xu, E. Leary, S. Hou, S. Sangtarash, M. T. González, G. Rubio-Bollinger, Q. Wu, H. Sadeghi, L. Tejerina, K. E. Christensen, *et al.*, "Unusual length dependence of the conductance in cumulene molecular wires," *Angewandte Chemie*, vol. 131, no. 25, pp. 8466–8470, 2019.

[46] A. Moneo, A. González-Orive, S. Bock, M. Fenero, I. L. Herrer, D. C. Milan, M. Lorenzoni, R. J. Nichols, P. Cea, F. Perez-Murano, *et al.*, "Towards molecular electronic devices based on 'all-carbon'wires," *Nanoscale*, vol. 10, no. 29, pp. 14 128–14 138, 2018.

[47] D. Wendinger and R. R. Tykwinski, "Odd [n] cumulenes (n= 3, 5, 7, 9): Synthesis, characterization, and reactivity," *Accounts of chemical research*, vol. 50, no. 6, pp. 1468–1479, 2017.

[48] N. Islam, T. Ooi, T. Iwasawa, M. Nishiuchi, and Y. Kawamura, "Thermal cyclotrimerization of tetraphenyl [5] cumulene (tetraphenylhexapentaene) to a tricyclodecadiene derivative," *Chemical communications*, no. 5, pp. 574–576, 2009.

[49] M. Tommasini, A. Milani, D. Fazzi, A. Lucotti, C. Castiglioni, J. A. Januszewski, D. Wendinger, and R. R. Tykwinski, "π-conjugation and end group effects in long cumulenes: Raman spectroscopy and dft calculations," *The Journal of Physical Chemistry C*, vol. 118, no. 45, pp. 26 415–26 425, 2014.

[50] S. Greenhill, S. Rana, S. Gupta, P. Vellanki, and S. Venkatesh, "Bayesian optimization for adaptive experimental design: A review," *IEEE Access*, vol. 8, pp. 13 937–13 948, 2020.

[51] H. Liu, T. Zhang, N. A. Krishnan, M. M. Smedskjaer, J. V. Ryan, S. Gin, and M. Bauchy, "Predicting the dissolution kinetics of silicate glasses by topology-informed machine learning," *npj Materials Degradation*, vol. 3, no. 1, pp. 1–12, 2019.

[52] H. Sahu, W. Rao, A. Troisi, and H. Ma, "Toward predicting efficiency of organic solar cells via machine learning and improved descriptors," *Advanced Energy Materials*, vol. 8, no. 24, p. 1 801 032, 2018.

[53] P. I. Frazier and J. Wang, "Bayesian optimization for materials design," in *Information Science for Materials Discovery and Design*, Springer, 2016, pp. 45–75.

[54] K. Dunn, "Process improvement using data," *Experimentation for Improvement. Hamilton, Ontario, Canada. Creative Commons Attribution-ShareAlike*, vol. 4, pp. 325–404, 2019.

[55] (2011). Sci-kit learn support vector machines, [Online]. Available: `https://scikit-learn.org/stable/modules/svm.html` (visited on 06/17/2020).

[56] P. Rivas Perea, "Support vector machines for regression: A succinct review of large-scale and linear programming formulations," *International Journal of Intelligence Science*, vol. 03, pp. 5–14, 2013.

[57] P. C. Deka *et al.*, "Support vector machine applications in the field of hydrology: A review," *Applied soft computing*, vol. 19, pp. 372–386, 2014.

[58] A. Barbosa, F. V. Paulovich, A. Paiva, S. Goldenstein, F. Petronetto, and L. G. Nonato, "Visualizing and interacting with kernelized data," *IEEE transactions on visualization and computer graphics*, vol. 22, no. 3, pp. 1314–1325, 2015.

[59] H. Yan, Z. Chen, Y. Zheng, C. Newman, J. R. Quinn, F. Dötz, M. Kastler, and A. Facchetti, "A high-mobility electron-transporting polymer for printed transistors," *Nature*, vol. 457, no. 7230, pp. 679–686, 2009.

[60] Y. M. Gross and S. Ludwigs, "P (ndi2od-t2) revisited–aggregation control as key for high performance n-type applications," *Synthetic Metals*, vol. 253, pp. 73–87, 2019.

[61] N.-K. Kim, E.-S. Shin, Y.-Y. Noh, and D.-Y. Kim, "A selection rule of solvent for highly aligned diketopyrrolopyrrole-based conjugated polymer film for high performance organic field-effect transistors," *Organic Electronics*, vol. 55, pp. 6–14, 2018.

[62] R. Steyrleuthner, M. Schubert, I. Howard, B. Klaumünzer, K. Schilling, Z. Chen, P. Saalfrank, F. Laquai, A. Facchetti, and D. Neher, "Aggregation in a high-mobility n-type low-bandgap copolymer with implications on semicrystalline morphology," *Journal of the American Chemical Society*, vol. 134, no. 44, pp. 18 303–18 317, 2012.

[63] Y.-J. Kim, N.-K. Kim, W.-T. Park, C. Liu, Y.-Y. Noh, and D.-Y. Kim, "Kinetically controlled crystallization in conjugated small-molec organic field-effect transistors," *Advanced Functional Materials*, vol. 29, no. 23, p. 1 807 786, 2019.

[64] K. Wasapinyokul, T. Panjasamanwong, W. Ponkasemsuk, C. Sriprachuabwong, and T. Lomas, "Mathematical model for thickness of off-center spin-coated polymer films," *Journal of Applied Polymer Science*, vol. 137, no. 6, p. 48 356, 2020.

[65] A. F. Paterson, S. Singh, K. J. Fallon, T. Hodsden, Y. Han, B. C. Schroeder, H. Bronstein, M. Heeney, I. McCulloch, and T. D. Anthopoulos, "Recent progress in high-mobility organic transistors: A reality check," *Advanced Materials*, vol. 30, no. 36, p. 1 801 079, 2018.

[66] F. Pedregosa, G. Varoquaux, A. Gramfort, V. Michel, B. Thirion, O. Grisel, M. Blondel, P. Prettenhofer, R. Weiss, V. Dubourg, J. Vanderplas, A. Passos, D. Cournapeau, M. Brucher, M. Perrot, and E. Duchesnay, "Scikit-learn: Machine learning in Python," *Journal of Machine Learning Research*, vol. 12, pp. 2825–2830, 2011.

[67] J. González, Z. Dai, P. Hennig, and N. Lawrence, "Batch bayesian optimization via local penalization," in *Artificial intelligence and statistics*, 2016, pp. 648–657.

[68] S. Riera-Galindo, A. Tamayo, and M. Mas-Torrent, "Role of polymorphism and thin-film morphology in organic semiconductors processed by solution shearing," *ACS omega*, vol. 3, no. 2, pp. 2329–2339, 2018.

[69] A. Scaccabarozzi and N. Stingelin, "Semiconducting: Insulating polymer blends for optoelectronic applications—a review of recent advances," *Journal of Materials Chemistry A*, vol. 2, no. 28, pp. 10 818–10 824, 2014.

[70] S. M. Clarke, J. H. Griebsch, and T. W. Simpson, "Analysis of support vector regression for approximation of complex engineering analyses," *Journal of Mechanical Design*, vol. 127, no. 6, pp. 1077–1087, 2004.

[71] V. Vapnik, S. E. Golowich, and A. J. Smola, "Support vector method for function approximation, regression estimation and signal processing," in *Advances in Neural Information Processing Systems 9*, M. C. Mozer, M. I. Jordan, and T. Petsche, Eds., MIT Press, 1997, pp. 281–287. [Online]. Available: `http://papers.nips.cc/paper/1187-support-vector-method-for-function-approximation-regression-estimation-and-signal-processing.pdf`.